The Dissertation Committee for Andreas Muller
certifies that this is the approved version of the following dissertation:

Resonance Fluorescence and Cavity Quantum Electrodynamics with Quantum Dots

Committee:

Chih-Kang Shih, Supervisor

Daniel J. Heinzen

John W. Keto

John T. Markert

Li Shi

Resonance Fluorescence and Cavity Quantum Electrodynamics with Quantum Dots

by

Andreas Muller, B.S.; M.A.

DISSERTATION

Presented to the Faculty of the Graduate School of
The University of Texas at Austin
in Partial Fulfillment
of the Requirements
for the Degree of

DOCTOR OF PHILOSOPHY

THE UNIVERSITY OF TEXAS AT AUSTIN
May 2007

To my little nephews, Eduardo, Yohan and Stellan.

Acknowledgments

This work would have been impossible without the constant enthusiasm and guidance of my advisor, Prof. C. K. Shih. I am also indebted to Prof. J. W. Keto, Prof. C. Piermarocchi and Prof. E. Li for continuous advice and discussions, and I am particularly thankful to Prof. D. G. Deppe for providing high quality quantum dot samples and intellectual contributions critical to this work. Other members of his group, specifically D. Lu, J. Ahn, D. Gazula, S. Quadery, and S. Freisem, are also gratefully acknowledged. Further thanks go to Regis André and Ivan-Christophe Robin for growing the ZnSe impurity sample, and to W. Ma, J. Zhang, and G. J. Salamo for providing the planar microcavity sample.

I would like to thank all my colleagues, particularly Pablo Bianucci and Edward B. Flagg who have continually assisted me in the experimental and theoretical work presented here. I have also often benefited from the help of Xiaoyong Wang, Han Htoon, Dmitri Kulik, Chris Wieland, and Qu-Quan Wang.

Finally I would like to acknowledge Allan Schroeder, Jack G. Clifford, Lanny Sandefur, as well as all the people of the machine shop, cryogenic shop, and electronics shop who have contributed to the construction, maintenance, and daily operations of the experimental setup.

I acknowledge financial support from the national science foundation and thank my friends and family who have accompanied me during all these years.

Resonance Fluorescence and Cavity Quantum Electrodynamics with Quantum Dots

Publication No. ____________________

Andreas Muller, Ph.D.
The University of Texas at Austin, 2007

Supervisor: Chih-Kang Shih

Next-generation information technology is expected to rely on discrete two-state quantum systems that can deterministically emit single photons. Quantum dots are mesoscopic (∼10,000 atoms large) semiconductor islands grown in a host crystal of larger band-gap that make well-defined two-level quantum systems and are very attractive due to stability, record coherence times, and the possibility of integrating them into larger structures, such as optical microcavities.

This work presents experimental progress towards understanding the coherent optical processes that occur in single quantum dots, particularly such phenomena that might be one day utilized for quantum communication applications. High resolution low temperature optical spectroscopy is used in conjunction with first order (amplitude) and second-order (intensity) correlation measurements of the emitted field. A novel technique is introduced that is capable of harvesting the fluorescence of single dots at the same frequency as the laser, previously impossible due to insurmountable scattering. This technique enables the observation, for the first time, of single quantum dot resonance fluorescence, in both the weak and strong excitation regimes, which forms the basis for deterministic generation of single photons. Guided by the rich theoretical description available from quantum optics with atoms we obtain insight into the complex dynamics of this driven system.

Quantum dots confined to novel optical microcavities were further investigated using micro photoluminescence. An optical microcavity properly coupled to a two-level system can profoundly modify its emission characteristics via quantum electrodynamical effects, which are highly attractive for single photon sources. The all-epitaxial structures we probe are distinguished by a bulk morphology that overcomes the fragility problems of existing approaches, and provides high quality factors as well as small mode volumes. Lasing is obtained with larger structures. Additionally, isolation of individual dots is further realized in smaller cavities and the Purcell effect observed in time-resolved photon counting experiments.

Table of Contents

List of Tables

List of Figures

Chapter 1

Introduction

1.1 Preamble

Firm experimental and theoretical understanding of the quantum optical properties of atomic systems has culminated in recent years with demonstrations of previously unattainable degree of control, at the single-atom level, over light-matter interactions. These include spectacular Purcell enhancement of the spontaneous emission rate [62], the achievement of strong-coupling between a single atom and the single mode of an optical cavity [20, 149], and recently, the operation of a single atom laser in the strong coupling regime [101]. Such capabilities have opened up the possibility of testing the very foundations of quantum mechanics, for example via the Einstein-Podolsky-Rosen (EPR) paradox [43, 117]. They further contributed substantially to the advancement of quantum information science [19, 115].

Concurrently, the last few years have seen rapid advances in semiconductor fabrication and spectroscopy that have opened up the possibility to realize quantum optical effects in a bulk material. Unlike isolated atoms, molecules or ions, a semiconductor approach would provide a monolithic, integrated system, and benefit from existing infrastructure for mass production and commercialization. However, although in solid-state systems the application of quantum mechanics is central in describing the electronic structures of solids, semi-classical approaches are often sufficient to describe dynamic properties such as electron transport, even in highly advanced devices. Indeed, only recently has the advancement of materials synthesis enabled the fabrication of structures, e.g. quantum dots [4, 17, 35, 55, 64, 81], with a length scale lying in the region in which neither microscopic nor macroscopic properties prevail and where the quantum phase information contained in the many-body state can play a profound role.

Semiconductor quantum dots (QDs) possess similar optical properties to that of real atoms and are thus being called "artificial" atoms. In addition to a much larger transition dipole moment compared to their natural counterpart due to their mesoscopic size, QDs be fully tailored, at least in principle, to give rise to the desired electronic properties. These developments bring about new possibilities to explore quantum optical control in such nanostructures and to harness these quantum optical properties for novel optical device applications, particularly in the context of quantum information technology, towards which significant progress has been made within the last few years. Specifically, the demonstration of driven Rabi oscillations using excitonic states in QDs marked an important milestone for quantum optical control in these artificial atoms. Moreover, coherent control of multi-level QD systems further led to conceptual demonstrations of two-qubit operations such as CROT gate and SWAP gate. These demonstrations could be classified as "active" manipulations of quantum states as they employ laser beams to actively drive and shape the wave function of the quantum states. Meanwhile, significant progress has been made by placing artificial atoms inside optical cavities to modify their electro-magnetic properties. So-called "cavity QED" (cavity quantum electrodynamics) with artificial atoms, has led to demonstration of the Purcell effect (weak coupling) as well as vacuum Rabi oscillation (strong-coupling). These demonstrations bring about exciting possibilities for novel optoelectronic devices, such as efficient single photon sources for quantum cryptography applications. One might classify these effects as "passive" control of quantum optical properties of artificial atoms. In this sense, the modification of quantum optical properties is achieved through the modification of the environment without external drive that actively shapes the quantum state.

This work provides a contribution to this field that aims at combining the two, previously divided, topics of coherent control and single photon generation. In the following introduction, a brief summary will be given of quantum dots, together with a general introduction to interactions between light and an electronic state. Chapter 2 then focuses on quantum dots in general, and more specifically self-assembled QDs, how they compare to other types of approaches, and how they can be probed individually. Chapter 3 focuses exclusively on the coherent manipulation of excitonic states, and discusses the individual phenomena of interest, that have been reported experimentally. In Chapter 4, resonance fluorescence experiments are presented and discussed theoretically. Finally, Chapter 5 discusses cavity quantum electro-

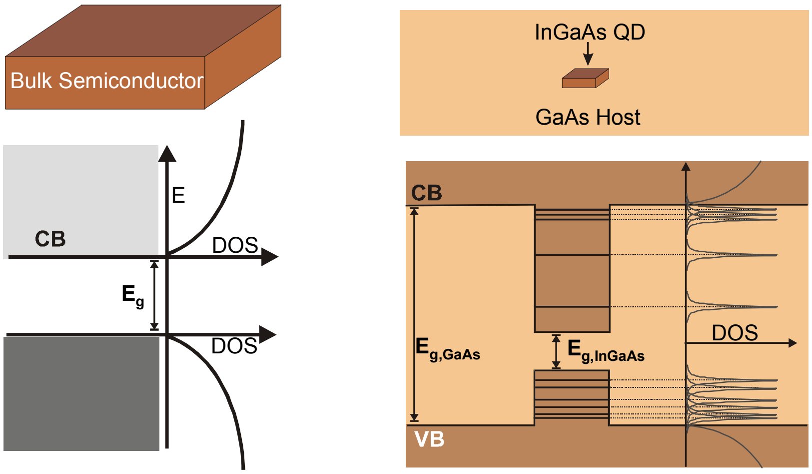

Figure 1.1: Density of states in semiconductor quantum dots (courtesy of H. Htoon).

dynamics with quantum dots in detail, with special focus on our own results with all-epitaxial microcavities, and Chapter 6 presents a brief outlook and conclusions.

1.2 Semiconductor Quantum Dots

Quantum dots come in a variety of forms that have in common the ability to fully localize electrons and holes in a semiconductor crystal. This confinement leads to a delta-function-like density of states, much like in atoms, thus the name "artificial atoms". Between discrete states, optical transitions can take place, ideally resulting in a spectrum with homogeneously broadened, sharp lines, as illustrated in Fig. 1.1. Depending on the material system, their size ranges from a nanometer to tens of nanometers. Roughly speaking, they can be subdivided into two groups, those which are chemically synthesized, so-called "colloidal" QDs [4, 34, 81], and those grown epitaxially [104]. Although colloidal QDs are of much interest for a number of practical applications, and can in fact be nowadays even purchased commercially, they do not, so far, provide enough coherence to be used for quantum information purposes. Specifically they suffer from bleaching, short shelf-life, and blinking associated with surface states. Most epitaxially-grown QDs, on the other hand, are buried in a matrix of high quality crystalline material of larger band-gap, and do not suffer as much, if at all, from the same problems as colloidal QDs do. In fact, samples can be studied for years without a noticeable sign of deterioration, despite having undergone a large number of drastic cooling and heating cycles. In addition, these types of dots can be combined and interfaced more easily with other integrated structures, and benefit from the readily available lithography and etching techniques of modern semiconductor technology. Epitaxial QDs can be grown using a variety of techniques, the most common being molecular beam epitaxy (MBE) and metalorganic chemical vapor deposition (MOCVD). The different types of dots within this category will be discussed explicitly in Chapter 2, as well as their growth modes and their specific confinement properties.

1.3 Introduction to Light-Matter Interactions

For our purpose and for almost all experiments with two-level systems interacting with the electromagnetic field, the basic equations of motion are a modified version of the equations describing the evolution of a spin-1/2 system. The state of the atom, or quantum dot is then represented by a ”pseudo-spin” vector.

1.3.1 Hamiltonian and Schrödinger Equation

For a system that can be in any of two states, $|0\rangle$ or $|1\rangle$, with energy W_- and W_+, respectively, and interacts with the electric field in the dipole approximation, the Hamiltonian reads (see for example Ref. [39] pp. 446):

$$H = W_-|0\rangle\langle 0| + W_+|1\rangle\langle 1| - \vec{d}\cdot\vec{E}(|1\rangle\langle 0| + |0\rangle\langle 1|)$$

where $\vec{d} = \langle 0|e\vec{r}|1\rangle$ is the dipole matrix element. The field is assumed to vary rapidly at a frequency ω, and slowly with an envelope $\mathcal{E}(t)$ so that

$$\Omega \equiv \vec{d}\cdot\vec{E}/\hbar = (d/\hbar)\times\mathcal{E}(t)\times(e^{i\omega t} + e^{-i\omega t})/2$$

denotes the interaction frequency, called ”Rabi frequency”. For a general state of the system, say $|\Psi\rangle = a_-(t)|0\rangle + a_+(t)|1\rangle$, the Schrödinger equation, $i\hbar\frac{\partial|\Psi\rangle}{\partial t} = H|\Psi\rangle$ becomes

$$\begin{cases} i\hbar\frac{\partial}{\partial t}a_+(t) = W_+a_+(t) - a_-(t)\frac{\hbar\Omega}{2}(e^{i\omega t} + e^{-i\omega t}) & (1) \\ i\hbar\frac{\partial}{\partial t}a_-(t) = W_-a_-(t) - a_+(t)\frac{\hbar\Omega}{2}(e^{i\omega t} + e^{-i\omega t}) & (2) \end{cases}$$

1.3.2 The Rotating Frame

If we use the transformation:

$$b_+(t) = e^{i\omega t/2}a_+(t)$$

$$b_-(t) = e^{-i\omega t/2} a_-(t)$$

then the dynamical equations become:

$$\begin{cases} i\hbar\frac{\partial}{\partial t} b_+(t) = -\frac{\hbar\omega}{2} b_+(t) + W_+ b_+(t) - b_-(t)\frac{\hbar\Omega}{2}(e^{2i\omega t}+1) & (1) \\ i\hbar\frac{\partial}{\partial t} b_-(t) = \frac{\hbar\omega}{2} b_-(t) + W_- b_-(t) - b_+(t)\frac{\hbar\Omega}{2}(1+e^{-2i\omega t}) & (2) \end{cases}$$

Neglecting the rapidly varying terms $e^{2i\omega t}$ and $e^{-2i\omega t}$ is called the "rotating-wave" approximation. The corresponding Hamiltonian now obviously reads

$$H_{RWA} = \begin{pmatrix} W_+ - \frac{\hbar\omega}{2} & -\frac{\hbar\Omega}{2} \\ -\frac{\hbar\Omega}{2} & W_- + \frac{\hbar\omega}{2} \end{pmatrix}$$

Finally, if we shift the origin of energies by an amount $W_- + \frac{\hbar\omega}{2}$, and introduce the "detuning" $\Delta\omega = (\omega_0 - \omega) = (W_+ - W_-)/\hbar - \omega$, we obtain (dropping the HWA index)

$$H = \begin{pmatrix} \Delta\omega & -\frac{\hbar\Omega}{2} \\ -\frac{\hbar\Omega}{2} & 0 \end{pmatrix} \tag{1.1}$$

which is now time-independent.

1.3.3 Density Matrix and the Optical Bloch Equations

An important concept for interpreting the outcome of our experiments in relation to the quantum mechanical equations of motion is the "density matrix", which takes into account that we are really just repeating the "experiment" a huge number of times and measuring an average. We do not know the precise state of the system. Rather, we can obtain its "ensemble" average (see for example Ref. [168] pp. 56). For instance, suppose again that the two-level system is in some general state $|\psi\rangle = c_0|0\rangle + c_1|1\rangle$ then its quantum mechanical expectation value is:

$$\langle A\rangle = \langle\psi|A|\psi\rangle = (c_0^*\langle 0| + c_1^*\langle 1|)A(c_0|0\rangle + c_1|1\rangle)$$

$$= c_0^*c_0\langle 0|A|0\rangle + c_0^*c_1\langle 0|A|1\rangle + c_1^*c_0\langle 1|A|0\rangle + c_1^*c_1\langle 1|A|1\rangle$$

but we measure an average (denoted by a bar) of this quantity over many measurements:

$$\overline{\langle A\rangle} = \overline{c_0^*c_0}\langle 0|A|0\rangle + \overline{c_0^*c_1}\langle 0|A|1\rangle + \overline{c_1^*c_0}\langle 1|A|0\rangle + \overline{c_1^*c_1}\langle 1|A|1\rangle$$

The coefficients $\overline{c_n^*c_m} = \rho_{nm}$ form the "density matrix" , and

$$\rho = \rho_{00}|0\rangle\langle 0| + \rho_{11}|1\rangle\langle 1| + \rho_{01}|0\rangle\langle 1| + \rho_{10}|1\rangle\langle 0|$$

is the "density operator". Because the coefficients c_{nm} satisfy the Schrödinger equation (see above), the time evolution of the density matrix can be easily found. It is given by:

$$\frac{\partial\rho}{\partial t} = \frac{i}{\hbar}[\rho, H]$$

For the Hamiltonian in Eq. 1.1, i.e. $H = \hbar\Delta\omega|1\rangle\langle 1| - \frac{\hbar\Omega}{2}(|0\rangle\langle 1| + |1\rangle\langle 0|)$, the commutator evaluates to:

$$[H,\rho]/\hbar = -\frac{\Omega}{2}|0\rangle\langle 0|(\rho_{10} - \rho_{01}) + |1\rangle\langle 0|(\Delta\omega\rho_{10} - \Omega(\rho_{00} - \rho_{11})/2) +$$

$$+|0\rangle\langle 1|(-\Delta\omega\rho_{10} - \Omega(-\rho_{00} + \rho_{11})/2) - \frac{\Omega}{2}|1\rangle\langle 1|(-\rho_{10} + \rho_{01})$$

and the resulting equations of motion read:

$$\dot{\rho_{11}} = \frac{i\Omega}{2}(\rho_{01} - \rho_{10})$$

$$
\begin{aligned}
\dot{\rho_{00}} &= -\frac{i\Omega}{2}(\rho_{01} - \rho_{10}) \\
\dot{\rho_{10}} &= -i\Delta\omega\rho_{10} + \frac{i\Omega}{2}(\rho_{00} - \rho_{11}) \\
\dot{\rho_{01}} &= i\Delta\omega\rho_{01} - \frac{i\Omega}{2}(\rho_{00} - \rho_{11})
\end{aligned}
$$

since $\rho_{00}+\rho_{11} = 1$ and $\rho_{10} = \rho_{01}^*$, we need only two of those equations. Together with phenomenological damping constants $1/T_1$ and $1/T_2$ for the diagonal and off-diagonal elements, we get the optical Bloch equations:

$$
\boxed{
\begin{gathered}
\dot{\rho_{11}} = \tfrac{i\Omega}{2}(\rho_{01} - \rho_{10}) - \rho_{11}/T_1 \\
\dot{\rho_{01}} = i\Delta\omega\rho_{01} - \tfrac{i\Omega}{2}(\rho_{00} - \rho_{11}) - \rho_{01}/T_2
\end{gathered}
}
\tag{1.2}
$$

These equations and variations thereof (such as including an additional level, or a quantized field) form the basis for the theoretical understanding of almost all our experiments. Here the constants T_1 and T_2 are borrowed from NMR where they denote the longitudinal and transverse spin decay, respectively. Appendix A further shows how damping can be included rigorously.

Chapter 2

Quantum Dots and Their Spectroscopy

2.1 Types and Fabrication of QDs

2.1.1 Naturally Formed Dots

Also called ”interface fluctuation quantum dots”, naturally formed quantum dots arise due to monolayer fluctuations in the width of a quantum well, typically GaAs/AlGaAs, when subject to growth interrupts during fabrication (Fig. 2.1). Reported early in pioneering near field studies [65] and using photoluminescence spectroscopy [53–55, 163], they provide moderate confinement energies in the ∼20 meV range. Although there is no obvious strategy to tailor the shape, density, size, etc. of these dots, they remain attractive when large transition dipole moments are required, for instance for achieving the strong coupling regime between a single emitter and the single mode of an optical microcavity [123], or for experiments in which non-linear signals are measured [121].

2.1.2 Self-Assembled QDs

Self-assembly occurs spontaneously when a critical thickness is reached during the deposition of a slightly lattice-mismatched material onto its host substrate (Fig. 2.2). Various growth modes exist, the most common being the

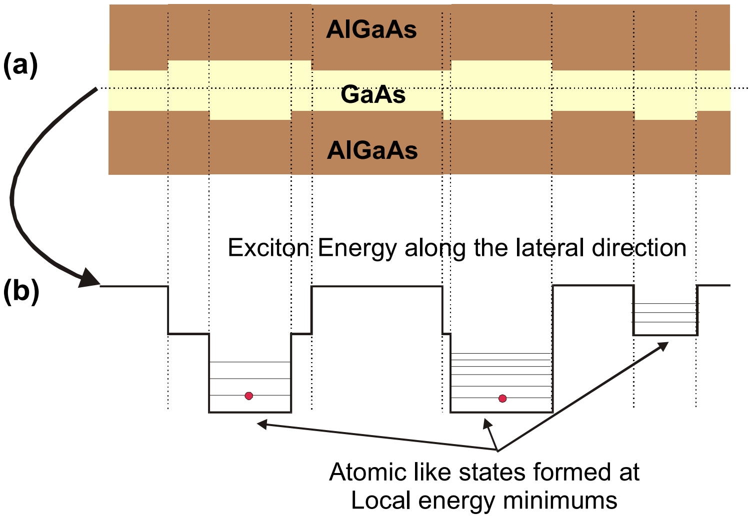

Figure 2.1: Naturally formed quantum dots (courtesy of H. Htoon).

so-called "Stranski-Krastanow" mode [143] usually used for III/V systems. Self-assembled dots constitute the most thoroughly studied system, and arguably the most promising for applications and experiments in which optical coherence is required.

InAs QDs in GaAs, for instance, are of extremely high optical quality, emit in a region close to the telecom band, can be tailored to a large extent for size, density, composition, etc, and can be embedded in other structures such as microcavities for devices. The dots, that "live" on top of a thin residual 2D InGaAs layer known as the "wetting layer", can have surface densities exceeding 100 μm^{-2} (Fig. 2.4) down to as low as a few per μm^{-1}. Their size ranges from a few nanometers to tens of nanometers. Figure 2.5 provides an example of growth conditions such that the size of the dots is particularly

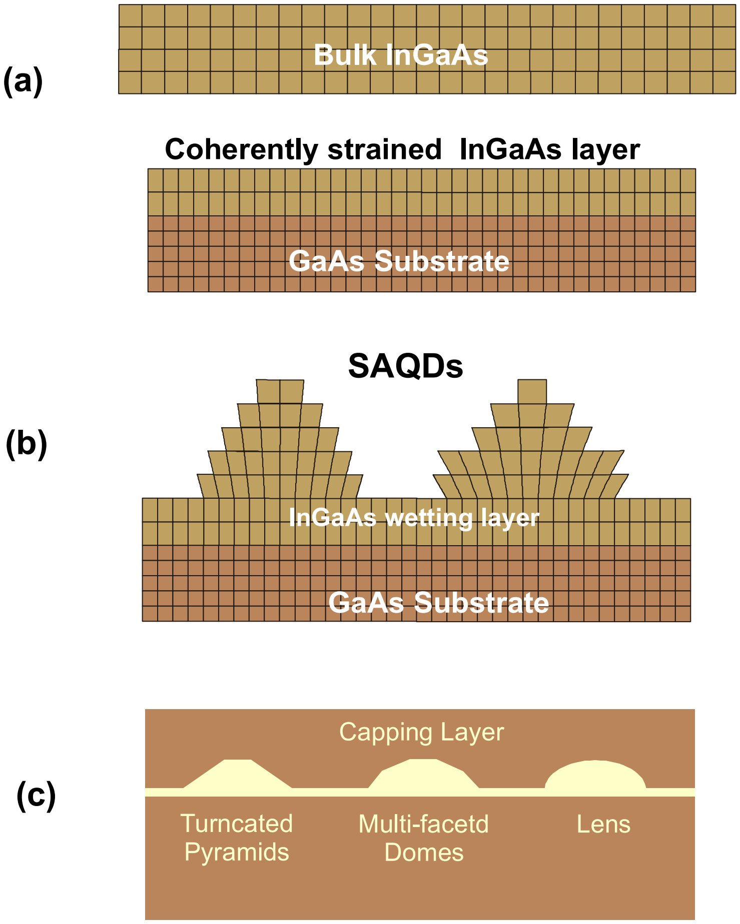

Figure 2.2: Self-assembly of high quality epitaxial quantum dots (courtesy of H. Htoon).

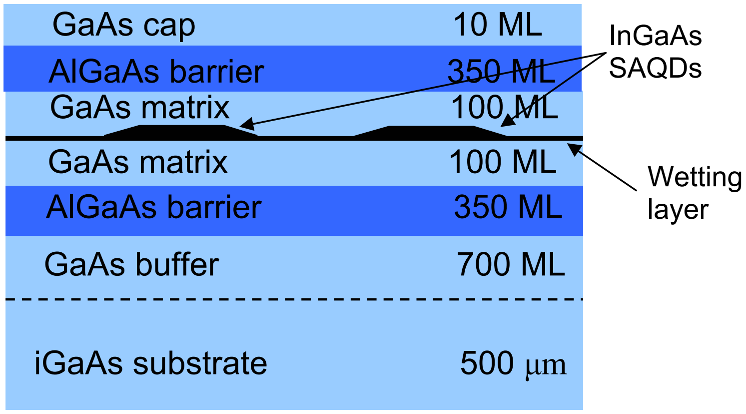

Figure 2.3: Structure of plain quantum dot sample.

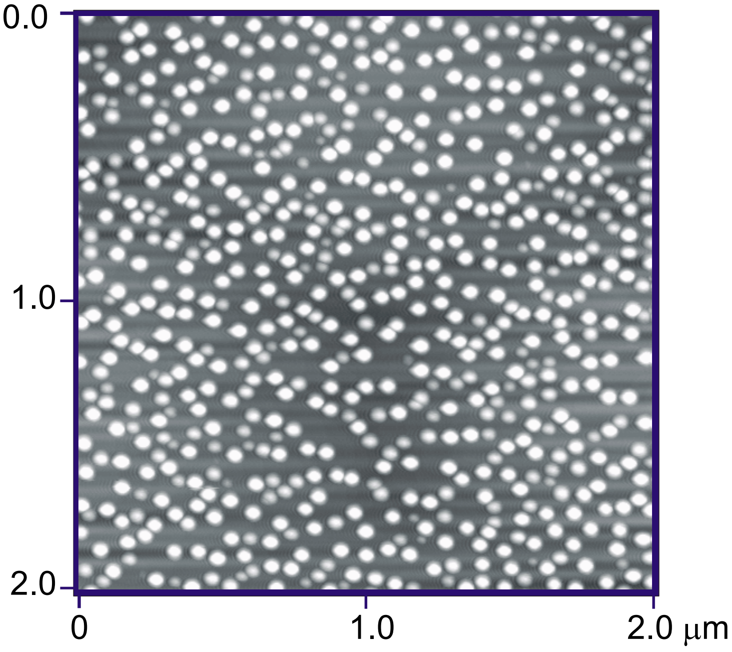

Figure 2.4: Atomic force microscopy image of uncapped quantum dots.

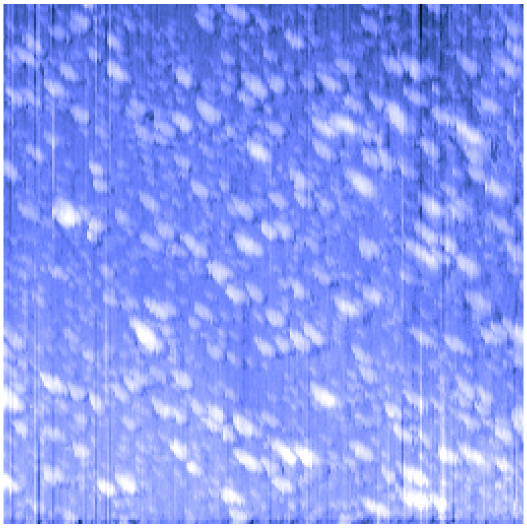

Figure 2.5: Atomic force image of particularly inhomogeneously sized quantum dots (courtesy of S. Wu).

inhomogeneous. Self-assmbled QDs have been grown in a variety of materials such as $\mathrm{Al}_y\mathrm{In}_x\mathrm{Ga}_{1-x-y}\mathrm{As/GaAs}$ [11], In/InGaP [36, 83], GaSb/GaAs [63], InSb/GaSb [6], Si/Ge [1, 42], and even II/VI based systems [165]. The growth of self-assembled quantum dots typically involves multi-layer structures such as shown in Fig. 2.3. Figure 2.6 shows a photoluminscence ensemble spectrum of such a sample at low temperature. This particular sample was purposefully grown to provide dots emitting in the <1000 nm spectral region to enable usage of common high-sensitivity detectors.

2.1.3 Impurity States as Another Type of QD

During the course of this work, various other sample systems have been explored, one of which consists of Tellurium impurity centers in bulk ZnSe

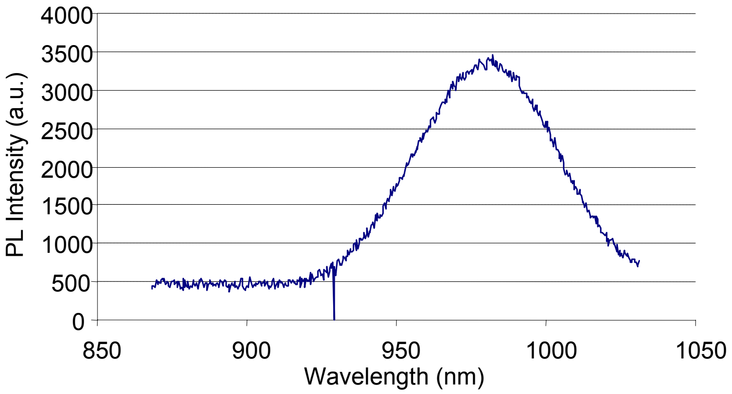

Figure 2.6: Low temperature (10 K) PL spectrum of an ensemble of self-assembled quantum dots.

[109]. The results obtained with this sample are described here. This approach is part of a general trend of substituting large QDs that suffer mostly from inhomogeneities (no two dots are alike), with simpler structures of well-known composition, shape, orientation, etc. This has led for example to studies of Nitrogen vacancy centers in Diamond [33, 84], Nitrogen impurities in ZnSe [145] or Nitrogen isolelectronic complexes in GaAs [51], which have shown very sharp linewidths and non-classical quantum optical effects such as anti-bunching. As shown below, impurity centers in bulk, high-quality semiconductors do in fact resemble much quantum dots, at least as far as the optical properties are concerned.

The sample investigated here was grown by molecular beam epitaxy (MBE) on a GaAs substrate and consists of 1 monolayer (ML) Te-doped ZnSe sandwiched between 40 nm thick layers of ZnSe, with a nominal Te concentration of 2500 μm^{-2}. Tellurium is known to isoelectronically substitute Se, providing unusually strong confinement [85, 88, 166, 167]. The sample, typically maintained at 10 K, was excited non-resonantly (415 nm) with a frequency-doubled Ti:Sapphire laser that delivers ∼1 ps pulses at a repetition rate of 80 Mhz. The PL was dispersed by a 0.5 m spectrometer and imaged onto a two-dimensional charge-coupled device (CCD) detector. Photon correlation measurements were performed using a conventional Hanbury Brown and Twiss (HBT) setup, with a 50/50 beam splitter and two single-photon-counting avalanche photodiodes (APDs)[105, 106, 130]. Such a setup measures the number of photon pairs n(τ) with arrival time separation τ, which is proportional to the second order correlation function $g^{(2)}(\tau)$. For time-resolved single photon measurements, the same setup was used with only one APD (time resolution ∼500 ps). When higher collection efficiency was necessary, we used a high-index hemispherical solid immersion lens[98] in direct contact with the sample surface. In Fig. 2.7, a typical (unpolarized) PL spectral image from our sample is shown. The strong band-edge emission around 2.8 eV is characteristic for high-purity ZnSe. Additionally, many sharp lines appear in the range from 2.6-2.8 eV and are not seen in undoped ZnSe[134]. Such features are the hallmark of excitons confined in all three dimensions and reflect the delta function-like density of states of such a system. Their real linewidth may be much narrower and is limited here by the spectrometer resolution (∼400 μeV). Most peaks actually consist of doublets with an average splitting close to 0.6 meV. The PL spectrum of two such doublets is shown in the spec-

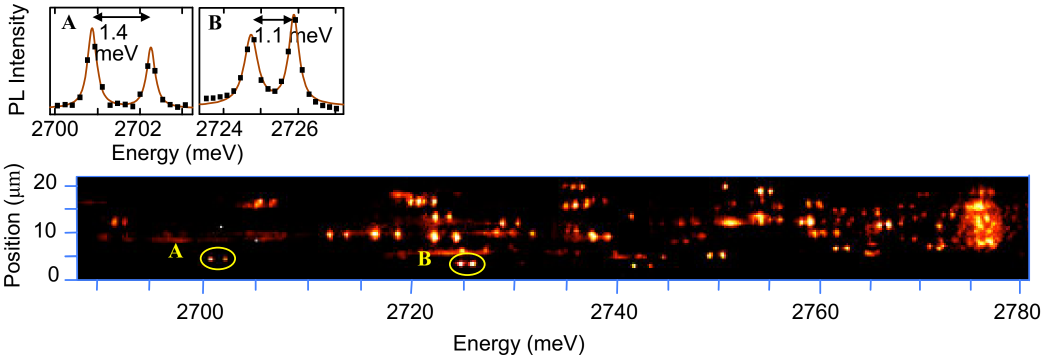

Figure 2.7: PL image of ZnSe:Te.

tra of Fig. 2.7. As has been pointed out in the past[145], observation of sharp PL peaks does not ensure single emitter properties. To verify that the peaks indeed originate from individual quantum emitters, we measured their photon statistics with the HBT setup described above. A typical trace from such a measurement, performed on the peak in Fig. 2.8(a), is shown in Fig. 2.8(b). For a light source with Poissonian statistics such as a laser, peaks separated by the laser repetition period would be observed[105, 106, 130]. Here the central peak is suppressed compared to all other peaks [Fig. 2.8(c)]. The probability of emitting two photons simultaneously is low, which is an intrinsic property of two-level quantum systems.

We next show that the PL doublets of Fig. 2.7 arise from excitons bound to nearest-neighbor Te pairs. Kuskovsky et al. [85] had already argued that single Te atoms could not account for the ~100 meV confinement potential observed in the PL spectra. If excitons bound to single Te atoms

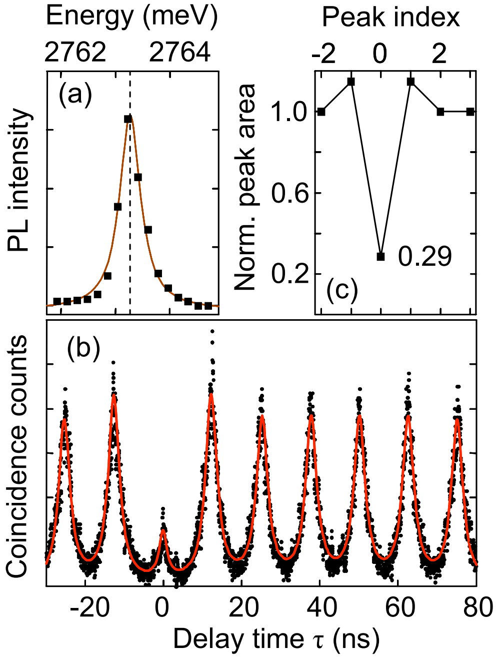

Figure 2.8: Photon anti-bunching from a single center in ZnSe:Te.

would in fact give rise to the PL doublets, we would expect a $\sim$500 times greater number of them (we observe 1-5 per μm^2) and it would be impossible to isolate them without patterning the sample with submicron apertures or mesas. On the other hand, stochastic estimation of nearest-neighbor Te pairs yields an average concentration of 4 μm^{-2} at our nominal doping, consistent with the experimental observation. Furthermore, the peaks within a doublet are strongly polarized. As shown in Fig. 2.9(a) for a particular doublet, the emission from the high (low) energy peak is linearly polarized at 90° (0°) in the sample plane, corresponding to the and crystallographic axes. In fact, almost all doublets follow identical behavior [Fig. 2.9(b)]. This is consistent with emission from nearest-neighbor pairs of the anion sublattice where Te substitutes Se; the orientation of neighboring Te atoms must be either along [110] or along [$\bar{1}$10], and to each Te$_2$ corresponds one spectral doublet. Due to the extremely low density of impurities, we cannot completely rule out alternative interpretations of our experimental data that could be associated with other defects/impurities in ZnSe[127, 161]. However, we believe the present interpretation to be the most consistent.

Ab-initio density functional calculations provide strong support to the picture given above. Using the one-electron band structure, we derived the relative binding for the electronic states involved in the exciton formation for a single Te and a Te$_2$. Our pseudopotential calculations (local density approximation) were performed in a 64 atoms supercell using 2x2x2 **k**-space sampling and an energy cut-off of 25 Ry. The results give a binding energy

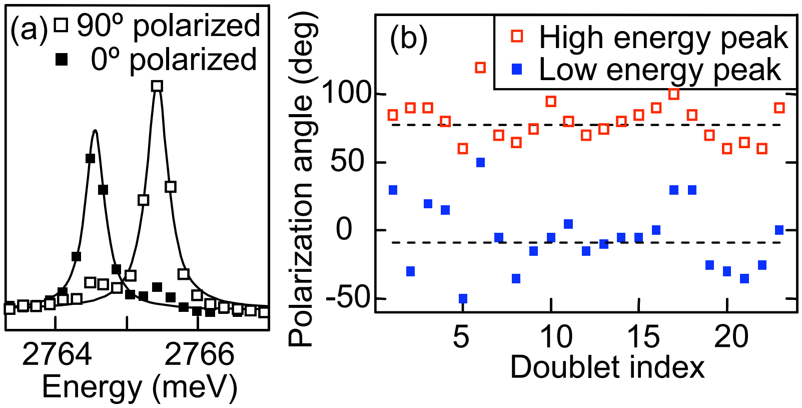

Figure 2.9: Polarized spectrum of a single PL doublet and polarization angle distribution.

(E_b) of about 3 meV for the single Te impurity whereas a substantial $E_b =$ 40 meV for the Te_2. Even if our calculations are limited by the supercell size they indicate that Te pairs produce a confinement which is one order of magnitude larger than for a single Te. The discrepancy with the observed binding energy for the excitons is likely due to Coulomb and spin-orbit effects. The non-equivalence between [110] and [$\bar{1}$10] is common in MBE-grown (001)-oriented III-V or II-VI compounds where the anion dimerizes along [110] and [$\bar{1}$10] on the surface during growth[119]. This explains why the high energy peak is preferentially polarized at 90° [Fig. 2.9(b)]. We also find no correlation between the emission energy and the magnitude of the splitting (performed on 23 doublets) which is expected if non-nearest neighbor pairs would bind an exciton. Therefore, the inhomogeneity in emission energy and splitting most likely arises from the random strain field created by the Te atoms in the vicinity of each nearest-neighbor Te pair. This is supported by the ab-initio calculation which indicates that the energy gap for ZnSe:Te_2 is very sensitive to small changes of the nearest Te-Te bonding length in the supercell. Moreover, the simulation shows that a single Te atom produces a strain field that affects the bonding lengths up to 6 percent. This interpretation is also consistent with the fact that observed inhomogeneous broadening is larger compared, for example, to the case of GaP:N [90], where the lighter N provides weaker strain.

The D_{2d} quantum-well-like symmetry introduced by the delta-doping allows us to neglect the light holes and consider only the lowest heavy-hole and conduction bands both having Γ_6 symmetry. The symmetry for the ground state heavy hole exciton states is therefore obtained as $\Gamma_6 \otimes \Gamma_6 = \Gamma_1 \oplus \Gamma_2 \oplus \Gamma_5$. Γ_1 and Γ_2 are both 1-dimensional and optically inactive while Γ_5 is two-dimensional and transforms like the in-plane x, y components of the dipole operator. The short-range e-h exchange interaction splits the dark states $\Gamma_1 \oplus \Gamma_2$ from the optically active Γ_5. When the symmetry is further reduced to C_{2v} by the presence of Te_2, the 2-dimensional representation Γ_5 becomes $\Gamma_2 \oplus \Gamma_4$ which are split by the long-range part of the e-h exchange. These are the doublets observed in Fig. 2.7, polarized along the Te_2 axis (Γ_2) and orthogonally to it (Γ_4).

The optically dark states, though not visible in the PL spectrum, can nevertheless affect the population of the bright states indirectly via a spin-flip process, resulting in a thermal mixture of states. Consequently, the PL decay becomes biexponential [86]. Figure 2.10(a) shows the time-resolved PL of the high energy peak in the doublet of Fig. 2.9(a), for different temperatures. While the fast component τ_S is close to the resolution limit of our setup, the slow component τ_L is easily resolved and varies significantly with temperature. Such a situation was discussed explicitly for single CdSe colloidal QDs [86, 116] and self-assembled QDs [47, 135]. A detailed model was developed in Ref.[86] using rate equations within a three-level system, consisting of the bright state $|A\rangle$, the dark state $|F\rangle$ and the ground state $|0\rangle$ (no exciton). Assuming the $|A\rangle \rightarrow |F\rangle$ spin flip rate γ_0 is larger than the radiative rates γ_A and γ_F, the slow component τ_L in the biexponential $|A\rangle \rightarrow |0\rangle$ decay reads:

$$\tau_L^{-1} = \frac{\gamma_A + \gamma_F}{2} - \frac{\gamma_A - \gamma_F}{2} \tanh(\frac{\Delta E}{2k_B T})$$

where T is the temperature [inset of Fig. 4(b)]. Note that the result does not depend on the $|A\rangle \rightarrow |F\rangle$ spin flip rate γ_0 or on the initial conditions. The activation energy ΔE equals the energy difference between $|A\rangle$ and $|F\rangle$. In Fig. 2.10(b), the slow decay rate, τ_L^{-1} extracted from the traces in Fig. 2.10(a) is plotted versus temperature (filled circles). A fit to this data with the equation above yields ΔE= 2.4 meV, as well as the intrinsic lifetimes γ_F^{-1}= 3.5 ns for the dark state and γ_A^{-1}= 0.5 ns for the bright state. The same procedure was applied to the time-resolved data of the low energy peak (same doublet). For this particular Te$_2$ we thus obtain the energy diagram shown in Fig. 2.10(c).

In Fig. 2.10, we plot: (a) time-resolved traces, for various temperatures, of the PL from the high energy peak in Fig. 2.9(a). (b) Slow decay rate τ_L^{-1} versus temperature for the data in (a) (filled circles) and for data from a completely different doublet (x's). The inset depicts the Te_2 energy level diagram. State $|0\rangle$ represents the crystal ground-state (no exciton), T is the zero temperature $|A\rangle \rightarrow |F\rangle$ relaxation rate, and $\gamma_{th} = \gamma_0 N_B$. $N_B = \frac{1}{e^{\Delta E/k_B T}-1}$ is the Bose-Einstein phonon number at temperature T. (c) Summary of the fine-structure of one particular Te_2 probed.

We also probed other Te_2 and found comparable lifetimes, typically γ_F^{-1} ~2-4 ns and $\gamma_A^{-1} < 0.5$ ns. The data represented by x's in Fig. 2.10(b), for example, was recorded on the high energy peak of a different doublet. Note that the data closely follows the hyperbolic tangent function. Unlike colloidal QDs [86], Single Te pairs exhibit a systematic bi-exponential PL decay. This material system is thus unique in that both the bright states, and the effect of the dark states can be observed without an external magnetic field. This picture could nevertheless easily be complemented and confirmed by magneto-optical measurements.

In summary, using PL spectroscopy we have investigated the zero-dimensional semiconductor system consisting of Te impurities in bulk ZnSe, in the limit of very low Te concentration. We find that in such a sample, PL doublets originate from the recombination of excitons bound to nearest-neighbor Te pairs whose fine-structure is manifested in the spectral and temporal PL. Such a system turns out to be very promising for studies of zero-dimensional excitons, since it possesses possible advantages over SQD systems, such as a well-defined structure and symmetry, and should be easier to model theoretically. It could also be suited for quantum optical experiments where large

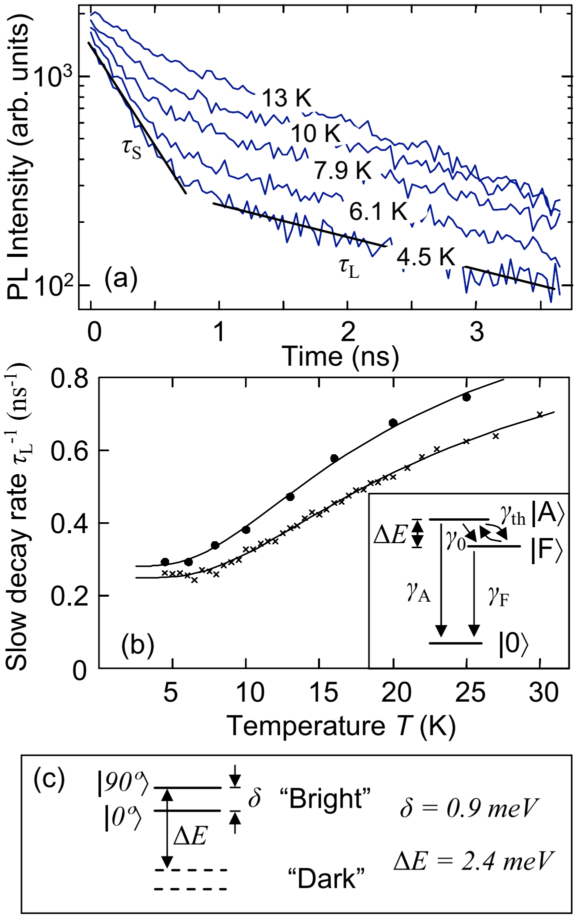

Figure 2.10: Time-resolved temperature dependent measurements on single impurity centers in ZnSe:Te.

transition dipole moments are essential [145], if proven to provide sufficiently long coherence times.

2.2 Spectroscopic techniques

Due to strong interest in probing individual QDs, and specifically their ground state, a number of techniques have been developed over the years by different groups worldwide. The most important among those techniques are described here. This (brief) summary is meant as a comprehensive review of the many methods now available. Except for photoluminescence spectroscopy and "photodiode spectroscopy" (see below), all other methods rely directly or indirectly on homodyne or heterodyne detection, via lock-in amplification. This means that input signals are modulated in such a way that a final output signal, that is dependent on the system dynamics, is modulated at a well-defined frequency not contained in the background signal.

2.2.1 Basic Photoluminescence

By far the most simple, inexpensive, and used of all techniques, photoluminescence (PL) spectroscopy requires basically an excitation source and a sensitive detector. Because relaxation in QDs is much faster than radiative recombinaton, the ground state PL linewidths of QDs can be very sharp, and many useful properties can be obtained by simple PL measurements [57, 99, 174]. For instance non resonant excitation can be used to characterize exciton and biexciton [72] lines by intensity dependent and/or time-resolved measurements [9]. Most basic temperature dependent characterization [13] or magnetic-field dependent measurements [15, 97] have been performed primarily by simple PL. The photoluminescence measurements described in this work have been carried out with a micro-PL apparatus set up by Dr. H. Htoon. Exhaustive details of the setup are available in Ref. [68] and we therefore omit them here.

2.2.1.1 Photoluminescence Excitation (PLE)

Photoluminescence excitation is a useful tool for resonantly probing QDs in their excited states. The photoluminescence from the ground state is simply recorded while the laser is scanned in frequency from the band-edge down to the first excited-state of the dot. In some sense, it resembles an absorption measurement, but differs in that the final emission intensity that is measured depends on all relaxation mechanisms that might occur before. In the early measurements it was widely applied to single QDs to study their spectra and relaxation mechanisms [54, 55, 69, 150].

2.2.1.2 Electroluminescence

In electroluminescence measurements, carriers are generated electrically through lithographically defined leads. The carriers generated can recombine and the emission spectrum carries information related to the level structure of the system. This method is often applied to QDs [73], particularly for structures in which lasing from electrical injection is to be achieved [170].

However this technique does not provide high resolution or coherent control capabilities since current injection is "slow" and incoherent.

2.2.2 Pump-probe Techniques

2.2.2.1 Differential Transmission

In differential transmission measurements, the dot is excited by more than a single beam, usually two. One beam serves as a "pump" beam which acts on the QD strongly, and the second beam serves as a weak "probe", whose absorption is measured [60, 140, 141]. What is actually detected is a nonlinear signal that depends on both fields, so that if each is modulated independently at certain frequencies, then the relevant signal contains both those frequencies, and can be amplified by lock-in for instance at the difference frequency. Since the strength of the nonlinear signal is very sensitive to the dipole moment of the transition that is probed, most experiments with QDs have focused on naturally formed dots [38], which can be much larger than self-assembled dots [89]. This technique usually requires an optically thin sample.

2.2.2.2 Near-Field Differential Reflectivity

An interesting near-field differential reflectivity method was reported in Ref. [67]. There an etched coated fiber tip is brought into close proximity with the sample surface and the excitation laser is sent through the fiber. The differential reflectivity signal is collected from the same fiber and depends sensitively on the presence of a QD in the near field of the fiber tip. Interestingly, the setup can be build such that the sample is cooled to He temperatures while the tip is held at room temperature, thus facilitating its positioning (room temperature walkers and stages can be used). This technique has enabled for example the observation of the optical stark effect with ultrafast pulses [152]. Generally, the coherent response of single QDs has been studied [58], and studies of coupled QDs have also been reported [153]. Traditional near-field methods such as NSOM have also been used to probe QDs [59], and, in some cases, can achieve very high spatial resolution [100].

2.2.2.3 Four-Wave Mixing

Transient four-wave mixing is a powerful tool to probe the quantum dot ground state on ultrafast time scales [24, 26, 27, 49]. Only recently has a modified technique been applied to single QDs [87]. Rabi oscillations could be observed on single dots [121].

2.2.2.4 Photodiode Spectroscopy

An alternative to purely optical spectroscopy is to combine it with electrical control. A structure ideally suited for injecting and collecting charges in and out of a QD is the Schottky diode structure. A doped layer is grown close to the QD layer, so as to make tunnelling in and out of the dot into the continuum possible. The bias voltage on another electrode provides the control knob for this tunneling direction and rate. When the dot is excited optically (in its ground state) the resonantly generated carriers can dissociate, leave the dot, and give rise to a photo current. This photocurrent is then proportional to the population that was induced optically. This type of spectroscopy was first reported in Ref. [49, 146, 173].

2.2.2.5 Stark Shift Modulation Spectroscopy

An interesting approach to probing the ground state is achieved by using the Stark effect. This technique was first demonstrated by Alen *et al.* [3] and subsequently applied to probing the fine-structure of a ground state exciton [66]. The idea is that under narrowband cw excitation, if the ground state transition itself is narrow enough, the resonance condition is very sensitive to a small applied voltage which slightly shifts the resonance frequency of the exciton. Therefore, if the external voltage is periodically varied at a certain frequency (which is slow compared to all other frequencies, say ∼100 Hz), then the QD response will contain that frequency and can be extracted by lock-in amplification, despite the presence of strong background (which does not contain this frequency). Although this technique has the additional capability of simultaneously charging the dot, it does require a special structure, however, which in turn requires elaborated fabrication and lithography. Furthermore, the Stark shift is a perturbative effect, and can only tune slightly. This means that wide transitions can not be probed, and much worse, that fast pulsed optical excitation is not possible (bandwidth is too large to be covered by the tuning range of the Stark shift).

2.2.2.6 Up-conversion

Ground state spectroscopy for an ensemble of dots can be done effectively using (non-linear) upconversion. This technique was pioneered by Shah [133]. It uses a non-linear crystal to convert the luminescence to a higher frequency (e.g double) by mixing it with a reference laser of high intensity. Because the pulse width of the laser can be made much shorter than the luminescence lifetime, which for a QD is on the order of $\sim$1 ns, monitoring the upconverted signal while changing the time-delay of the laser effectively samples the ground state luminescence background-free. This technique is sometimes applied to QDs [171], but only to ensembles so far, because of insufficient non-linear conversion efficiency due to the weak emission of a single dot. This non-linear upconversion is not to be confused with other types of PL upconversion, also discussed in QDs [75, 120], or with linear up-conversion discussed below.

2.2.3 Side-Excitation Spectroscopy

Here we describe another technique, that was developed during the course of this work. We use this method to obtain resonance fluorescence, to which Chapter 4 is devoted. Here we briefly introduce it, and show how it can be used to probe the ground state. It has the main advantage of allowing for (resonant) coherent control, while simultaneously making it possible to collect the emission. It does not require any complex modulation techniques and is relatively general and simple to implement.

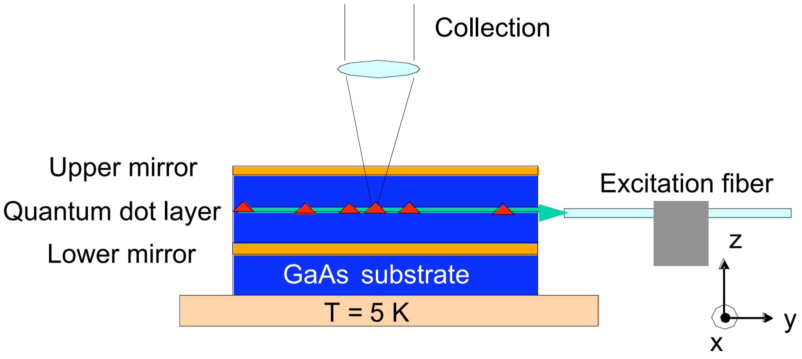

Figure 2.11: Sketch of the side excitation technique.

2.2.3.1 Apparatus

We employ a planar microcavity, grown by the group of G. Salamo, and use a side excitation geometry (Fig. 2.11). We have characterized this cavity before, in different contexts [160]. A single mode fiber mounted on a three-axis high resolution walker and maintained at room temperature is brought within a few microns of the cleaved sample edge. If the cleave is of good quality, the laser couples efficiently to the waveguide modes of the planar cavity, so that the beam can propagate at high power densities deep within the sample where it then excites the quantum dots. However, while the dots couple efficiently to the excitation beam, the unwanted scattered laser light, as observed on the detector after collection of the vertically emitted light, is poorly coupled out of the cavity and can thus be efficiently suppressed. It is important to realize that the cavity serves two purposes: (i) it increases tremendously the light extracted from the QD ground state emission due to good coupling to vertical

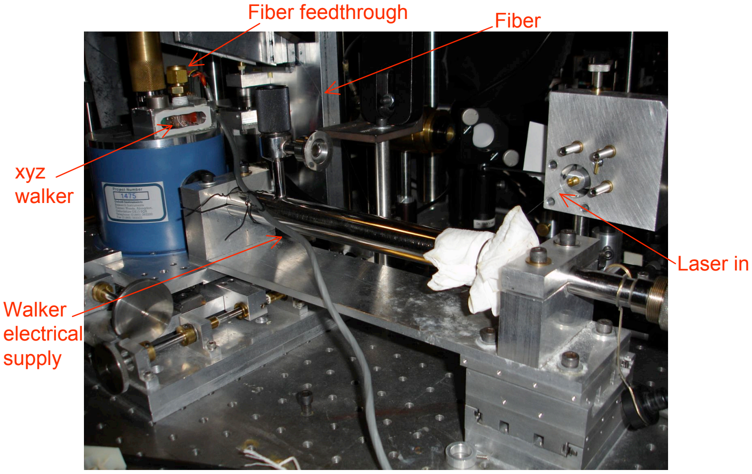

Figure 2.12: Photograph of modified Cryostat and experimental setup for introducing the fiber.

cavity modes, thereby increasing signal to noise ratios substantially, and (ii) it results in only a tiny fraction of scattered light being collected in those same vertical cavity modes, because the unwanted scattering which originates from defects, crystal imperfections, contaminants, etc. does not have a preferred direction. A photograph of the actual setup is shown in Fig. 2.12.

Figure 2.13 shows how the emission from a single QD is observed on top of the (now very small) scattering background. As the laser is scanned in frequency, this emission is observed to go over a resonance, with a linewidth of less than 10 μeV, in agreement with prior measurements of similar, low-confinement, quantum dots that are characterized by only moderate excitonic level spacings (1-10 meV). For that same QD, we also show the full photoluminescence excitation (PLE) spectrum in which at least 7 excited states are

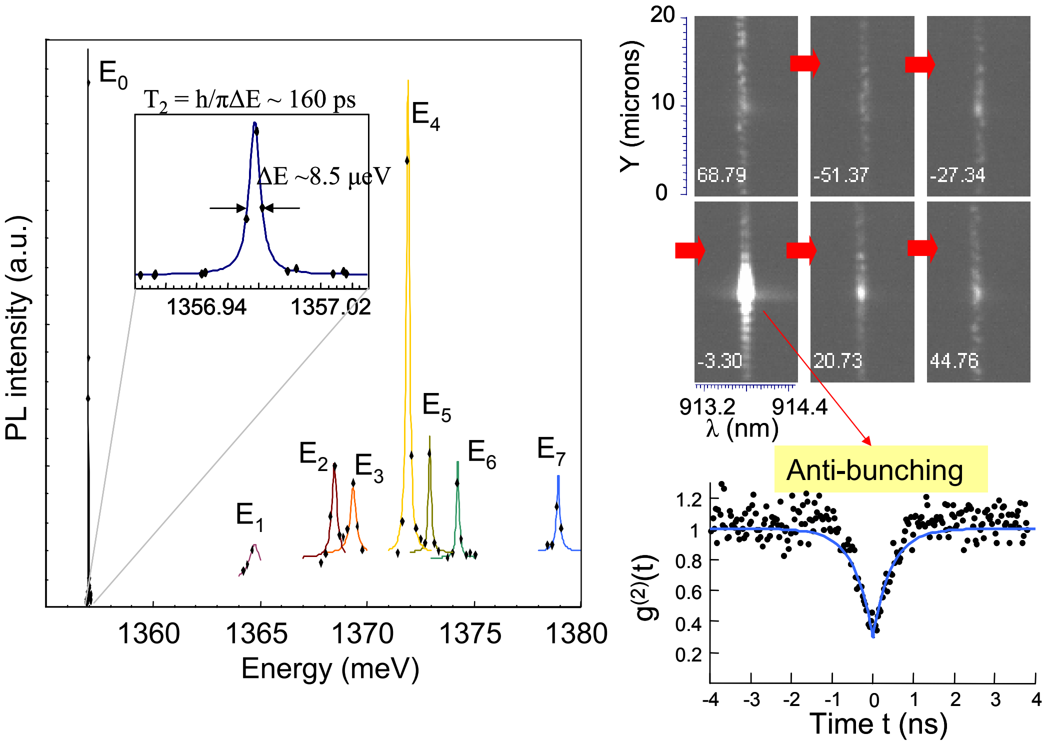

Figure 2.13: Probing the ground state and the excited states of single dot via side excitation.

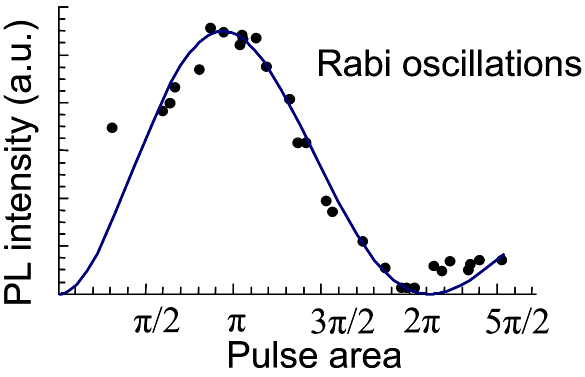

Figure 2.14: Rabi oscillations of a ground state probed using side-excitation.

observed.

In order to prove that the emission in Fig. 2.13 is really due to emission from the ground state (resonant scattering from a single two-level system), we have recorded the second order correlation function of the emitted light, using a Hanbury-Brown and Twiss interferometer. Indeed, as expected, a substantial dip is observed at t=0, which demonstrates single photon emission, which is only observable for light from a single quantum emitter.

Because the coherence provided by such a quantum dot ground state transition is already very long (8 μeV broadening corresponds to $T_2 >$150 ps), we expect that we will be able to coherently drive such a quantum dot ground state resonantly in the non-linear excitation regime. In fact, under pulsed excitation, we are able to observe the familiar ground state Rabi oscillations (Fig. 2.14). The corresponding process under cw excitation, which leads to the Mollow triplet is dealt with in Chapter 4. We note that one drawback of this

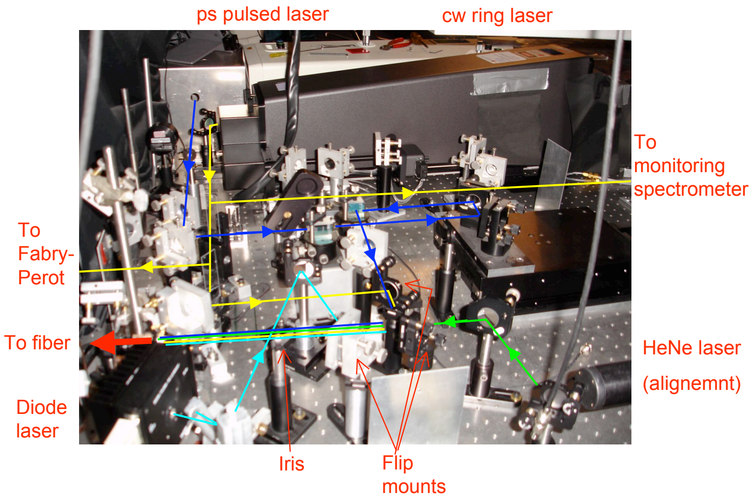

Figure 2.15: Photograph of the excitation section of the experimental setup.

technique is that only one polarization can be used. Fig. 2.15 and Fig. 2.16 show photographs of the setup were it can be seen how different lasers can be introduced depending on the desired excitation, i.e. pulsed, cw, etc... Since all lasers are eventually coupled to a fiber, it suffices to align each laser once, and switch between them via flip mounts. For narrow band cw excitation (ring laser), we use a scanning Fabry-Perot to monitor the linewidth (<40 Mhz) and the relative excitation energy. As is also shown in Fig. 2.15, the intensity, which is monitored with a lock-in detection for extended dynamic range, can be changed for any laser via neutral density filter wheels.

2.2.3.2 Example: probing temperature dependent effects

Here we illustrate the powerful features of the side-excitation approach by measuring upconversion in single dots. This was also the first interest-

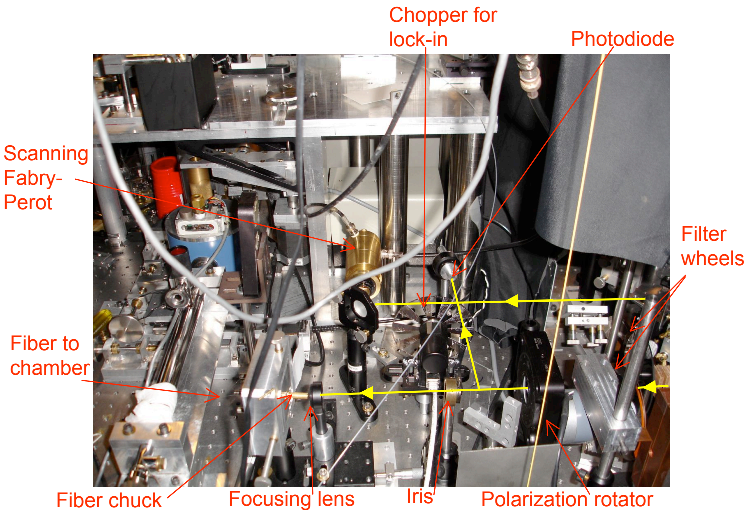

Figure 2.16: Photograph of fiber coupling section of the experimental setup.

ing observation that this technique enabled during its early implementation. Photoluminescence upconversion refers here simply to the thermal population of excited states when a single dot is excited resonantly in its ground state. Because we work at low temperature where $k_B T$ is usually less than 1 meV, thermal excitation of carriers occurs only if the energy separation between the ground and excited state is no more than a few meV. Probing such states obviously requires spectrally probing very close to, if not at the laser frequency.

We examine in detail two situations: (i) the standard PLE configuration where we excite resonantly in the excited state and look at the ground state emission and (ii) the laser excites the ground state, and emission from the excited state is observed and measured. This is depicted explicitly in Fig. 2.17. The corresponding experimental processes are illustrated in Fig. 2.18.

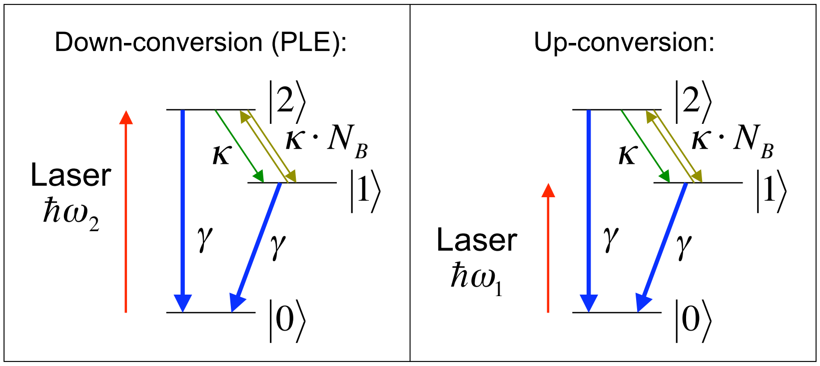

Figure 2.17: Excitation schematic of photoluminescence down and up conversion processes.

As the laser scans (in frequency) over the excited and the ground state, the emission form the ground and excited state, respectively, can be observed (the states are labeled by arrows in Fig. 2.18). Provided that the process is thermal, and that the radiative relaxation rates from state $|2\rangle$ and state $|1\rangle$ are about the same, the ratio of the PL must be given by a Bolzmann factor. This could be verified by explicitly changing the temperature and measuring the dependence on temperature of this ratio. It is easier, however, to measure the ratio from different dots and plotting it versus the energy splitting (which in general is different for any two dots). Three specific dots that have been probed are shown in detail in Fig. 2.19. It shows the resonance of the ground state, the excited state, and the corresponding PL spectra. From an ensemble of dots we can now extract the temperature (which is fixed at the same value for all dots measured), since we know the energy splittings in each dot (Fig. 2.20). The extracted value is close to the reading given by the temperature

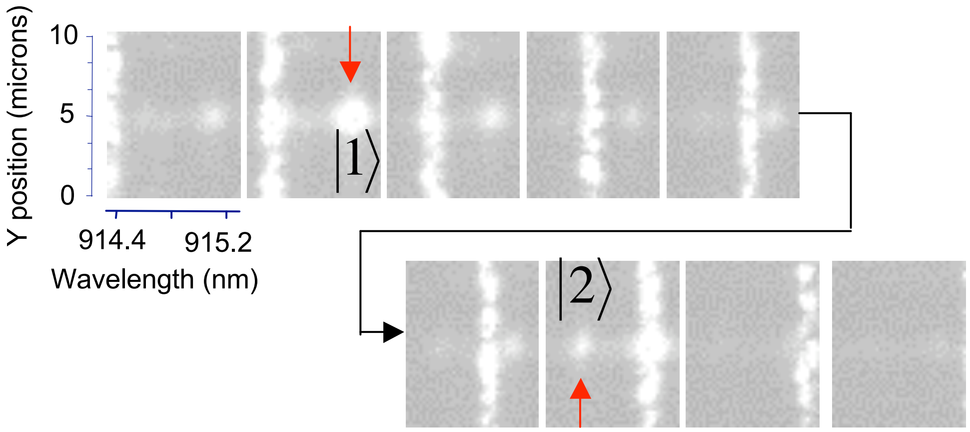

Figure 2.18: Observation of down and upconversion as the (cw) laser is scanned over the excited and ground state of a single dot (arrows).

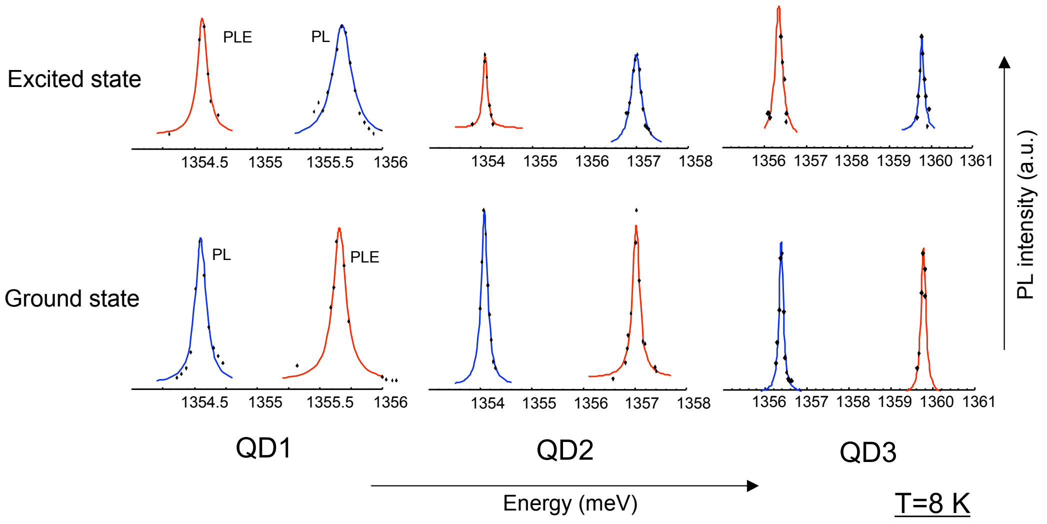

Figure 2.19: Full up and down conversion together with PL spectra for three different dots (pulsed excitation).

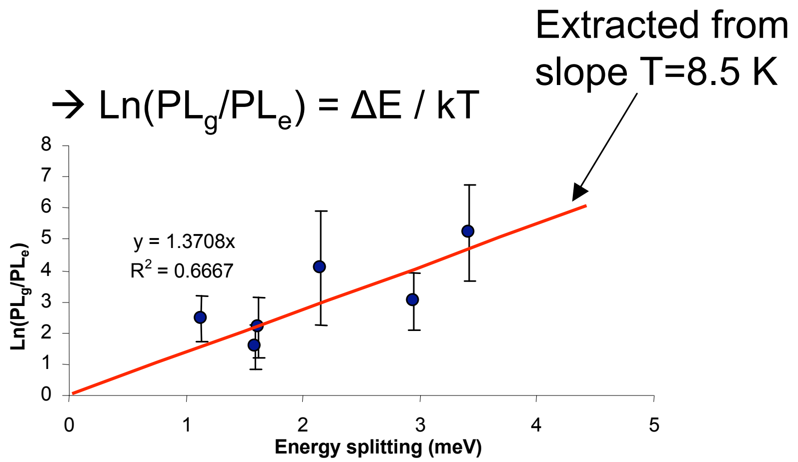

Figure 2.20: Ratio of up and down-converted PL as function of temperature for various dots.

sensor at the cold finger of the cryostat.

Chapter 3

Optical Coherent Control

3.1 Quantum Interference

Quantum interference refers to the basic (not necessarily non-linear) process by which the internal phase of the two-level system plays a role in its time-evolution. The simplest situation is that of a two-pulse measurement, first reported by Bonadeo *et al.* [25] with quantum dots. In such an experiment, the first pulse induces a coherence in the system, say it creates the state $|\Phi^{(1)}(t)\rangle$. A second pulse, identical to the first, follows, and must also induce a coherence, but at a later time delay, say it leads to the state $|\Phi^{(2)}(t-\tau)\rangle$, where τ is the time delay between the pulses. Now since the (total) state of the system must be a superposition of the two, i.e. $|\Psi(t,\tau)\rangle = |\Phi^{(1)}(t)\rangle + |\Phi^{(1)}(t-\tau)\rangle$ then the probability to find it excited is proportional to:

$$\int_{-\infty}^{\infty} \langle\Psi(t,\tau)|\Psi(t,\tau)\rangle dt = \int_{-\infty}^{\infty} \Big[\langle\Phi^{(1)}|\Phi^{(1)}\rangle + \langle\Phi^{(2)}|\Phi^{(2)}\rangle$$

$$+2\mathrm{Re}[\langle\Phi^{(1)}(t)|\Phi^{(2)}(t-\tau)\rangle]\Big] dt$$

The second term gives rise to quantum interference, as the time delay is varied. Another way to look at it is the following: the first pulse brings the system into a state which is not an eigenstate of the system, an thus it undergoes free evolution at its natural frequency (which is also the optical frequency since we are considering resonant excitation). At the time at which the second pulse comes in, it finds the system in a different state, depending on the time, i.e. phase evolution elapsed, and therefore acts either constructively or destructively on the net population. Such effects have been exploited for instance in the demonstration of the single qubit Deutsch-Jozsa algorithm [23] when the pulses are strong enough to populate the system half-way. The pioneering work of Htoon *et al.* [70] comprehensively explores such quantum interference phenomena in the non-linear regime. In practice, quantum interference is also a very useful tool to measure the intrinsic dephasing time of the two-state system. As the time delay between the pulses is increased, the interference contrast decays exponentially with a decay constant T_2. Figure 3.1 shows an example in which T_2 was measured for an excited state.

3.2 Rabi Oscillations

The most basic non-linear phenomenon that occurs in a two-level system is called "Rabi oscillation" or "Rabi flopping". It refers to the population oscillations that the system undergoes when the field strength is large enough so that the Rabi frequency exceeds the dephasing rate [5]. In that sense, it is a coherent process.

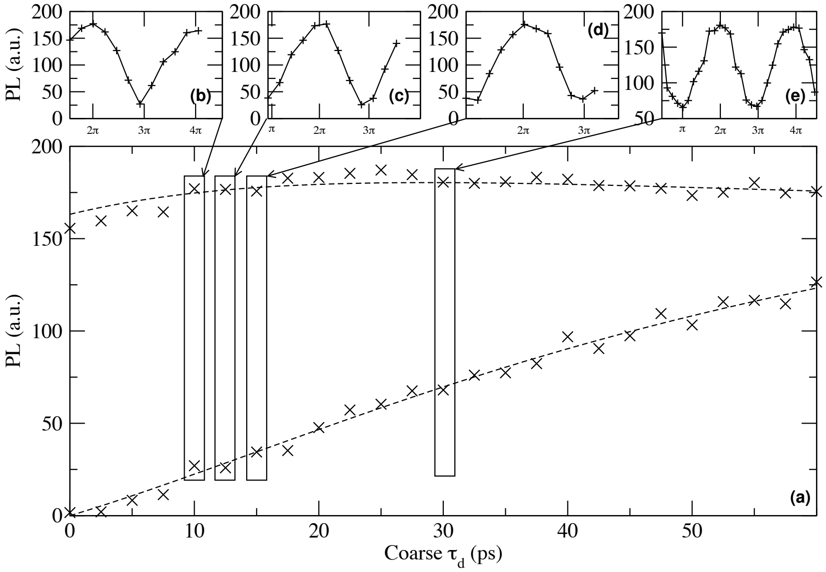

Figure 3.1: Quantum interference with the excited state of a single quantum dot (from Bianucci *et al.*, 2004).

3.2.1 Theory

Consider the optical Bloch equations in the absence of dephasing (Eq. 1.2). They can be solved easily, with the initial condition that all components of the density matrix are zero except for $\rho_{00} = 1$, i.e. the system is in the ground state at $t = 0$. In this case the equations read (also assume exact resonance, i.e. $\Delta\omega = 0$):

$$\begin{cases} \dot{\rho_{11}} = \frac{i\Omega}{2}(\rho_{01} - \rho_{01}^*) \\ \dot{\rho_{01}} = \frac{i\Omega}{2}(2\rho_{11} - 1) \end{cases}$$

which have the solution:

$$2\rho_{11}(t) - 1 = w(t) = \cos(\Omega t)$$

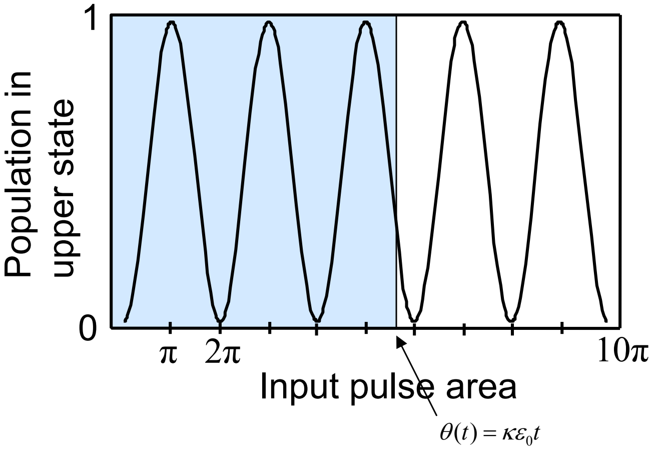

Figure 3.2: Rabi oscillations as a function of input pulse area.

or

$$\boxed{\rho_{11}(t) = \sin^2(\tfrac{\Omega t}{2}) = \sin^2 \tfrac{\theta(t)}{2}}$$

These oscillations are plotted in Fig. 3.2 explicitely. The quantity θ is called "input pulse area". Since it depends both on time and on the Rabi frequency, the oscillations can be either observed in the time domain, or in the "amplitude" domain, i.e. by changing the field amplitude. A "π" pulse means that all the population is transfered to the upper state while a "2π" pulse brings the system up and then back to the ground state. In the language of quantum computation, a Rabi oscillation represents a quantum bit (qubit) rotation. This is only ideal, of course, and in the presence of decoherence, the oscillations are quickly damped.

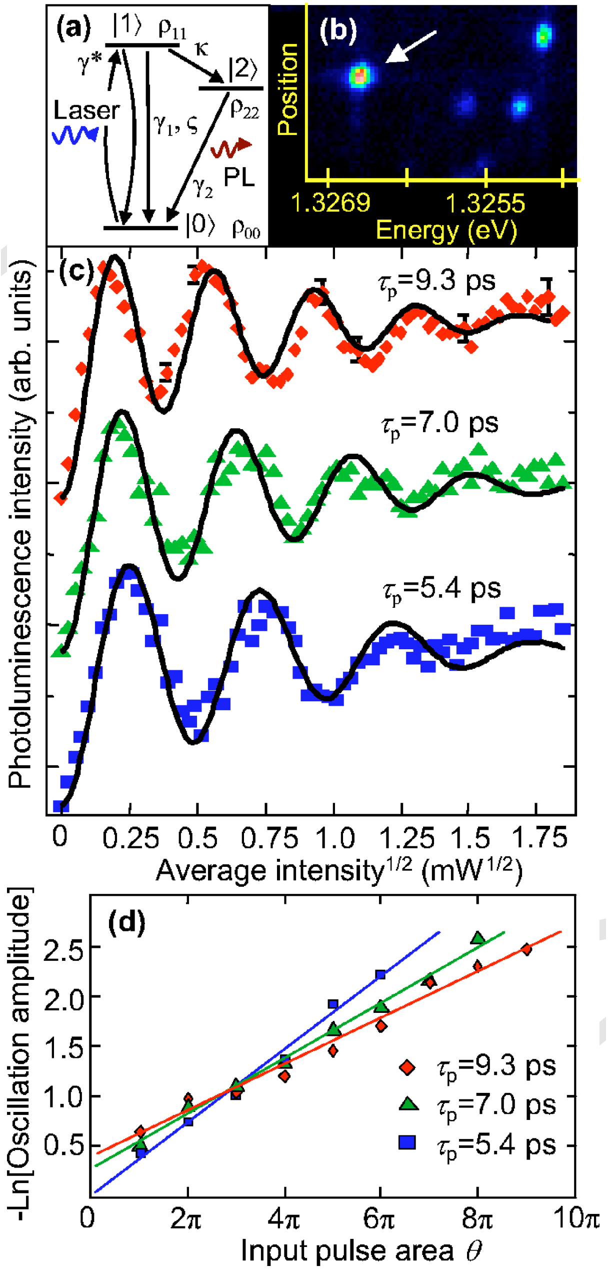

Figure 3.3: Rabi oscillations of the excited state of a single self-assembled quantum dot.

3.2.2 Experimental Observation

Rabi oscillations of excitonic states in quantum dots have been the subject of intense research in the past decade, and much progress has been made since the basic observation of the phenomenon. First reported by Stievater *et al.* [140] in naturally formed quantum dots and shortly after by Htoon *et al.* [70] and Kamada *et al.* [74] in self-assembled QDs, many different approaches have been taken since to measure the maximum number of observable oscillations. Zrenner *et al.* [173] for instance used a photodiode structure (see also Chapter 2) that allows to record the oscillations effectively in the ground state via the measurement of a photocurrent [146]. Rabi oscillations have also been reported on ensembles [29]. Further studies have focused on two-photon Rabi oscillations [148], that can give rise, for instance to a full two-qubit quantum logic gate [91]. Recently, Patton *et. al* [121] used four-wave mixing on single dots to obtain ground state Rabi oscillations. The polarization-dependence has been studied [22, 113], and Rabi oscillations of a charged excitonic state were also reported [21]. Figure 3.3 shows our own results for the excited state of a single self-assembled quantum dot [158]. This particular dot showed up to 10π oscillations, allowing more detailed insight. For example, the dependence on the pulse-width was explicitly obtained for the first time.

We have also focused on Rabi oscillations of dots delimited by a submicron size aperture, in order to tackle specific decoherence issues in this system. Indeed, the oscillations in Fig. 3.3 are not expected to be damped if the damping constants do not change with intensity. Fig. 3.4 provides evidence

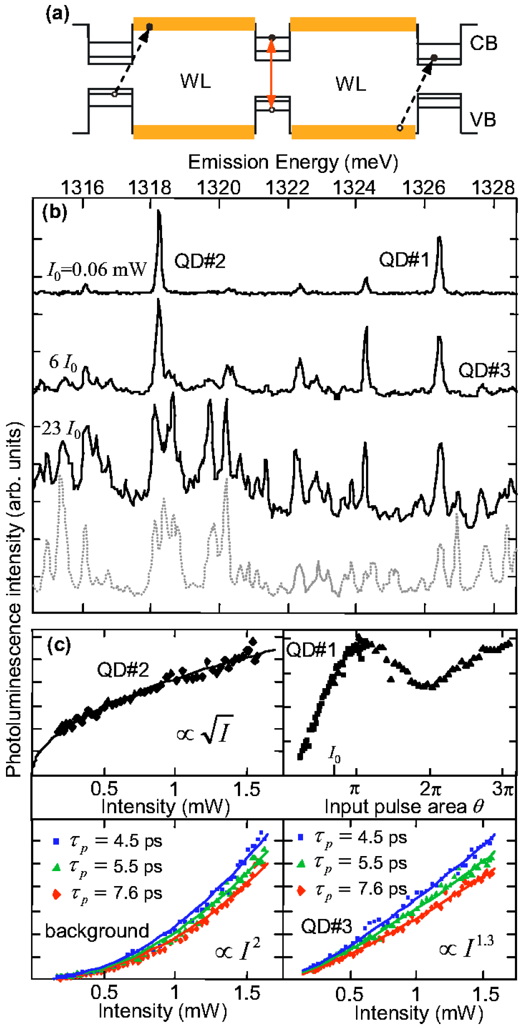

Figure 3.4: Rabi oscillations of a quantum dot beneath a sub-micron aperture and possible decoherence mechanism.

that the wetting layer might play an important role in the processes responsible for intensity dependent-decoherence of the excited state. We point to previous reports, in which other than simple bound-to-bound transitions can occur [69, 150, 155]. A similar situation might arise here, whereby the wetting layer states get populated even though there is not strictly an available transition for the process to occur. Recent reports of few quantum dot lasing [144], in which self-tuning of the cavity resonance with quantum dot states is attributed to wetting layer effects, point to similar transitions. We note that the damping of Rabi oscillations is by itself the subject of much controversy owing to the many different mechanisms proposed such as wetting layer mediated processes [157], and phonon-assisted damping [50].

3.3 Multilevel Manipulation: The V-Type System

Here we are concerned with non-linear coherent optical control of the fine-structure-split states, $|x\rangle$ and $|y\rangle$, of an excited exciton in a single SQD [159]. These states originate in SQD shape anisotropy [14, 113] and play an important role in spin relaxation [139], biexciton creation [91, 140], quantum beats and Raman beats [89]. Together with the vacuum state, $|v\rangle$ (no exciton), they naturally define a V-type three-level system, composed of two orthogonal transition dipole moments. In atomic V-type systems, important quantum effects have been pointed out [32, 48]. Yet there appear to be few investigations in the solid-state counterpart.

We focus on photoluminescence (PL) studies of a single self-assembled

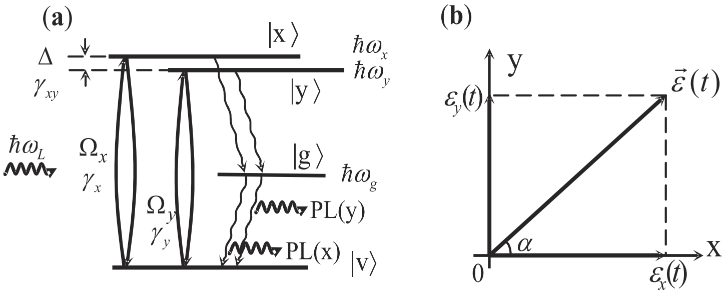

Figure 3.5: V-type energy-level structure and polarization configuration.

InGaAs/GaAs SQDs with V-type exciton energy structure. The Π_x and Π_y transitions to $|x\rangle$ and $|y\rangle$ are excited simultaneously by strong polarization-tailored pulses, resulting in unique dynamics involving the coupled transitions, Rabi oscillations, and quantum interference. In particular, we show that population oscillations between the two orthogonal states are realized, although a direct transition among them is forbidden. These interpretations are confirmed by density matrix calculations of the time-evolution of the system. The sample investigated contains $\text{In}_{0.5}\text{Ga}_{0.5}\text{As}$ SQDs grown by molecular beam epitaxy [12]. A mode-locked Ti:Sapphire laser delivering 6 ps long pulses at a repetition rate of 80 MHz is used to excite the sample (maintained at 5 K). The laser is resonant with the transitions from the vacuum state $|v\rangle$ to the first excited states $|x\rangle$ and $|y\rangle$ [Fig. 3.5(a)]. Measurement of the polarized PL intensity from recombination of ground-state excitons monitors the populations, ρ_{xx} and ρ_{yy}, of the excited states $|x\rangle$ and $|y\rangle$ in individual SQDs, i.e. the x-polarized (y-polarized) PL, denoted by PL(x) [PL(y)] is proportional to $\int_0^\infty \rho_{xx}dt$ ($\int_0^\infty \rho_{yy}dt$), when spin-relaxation is negligible. The PL signals were recorded using a spectrometer combined with a 2D liquid nitrogen cooled CCD array detector. The energy splitting, due to the anisotropic electron-hole exchange interaction, was measured from the polarized photoluminescence excitation (PLE) spectrum to be about Δ=85 μeV for the particular SQD studied, but may vary from dot to dot between $\sim$50 and $\sim$150 μeV.

The laser bandwidth, although larger than the $|x\rangle - |y\rangle$ energy splitting, is too small to excite a bi-excitonic state. The laser (energy $\hbar\omega$) is also far from resonance with the exciton ground state, $|g\rangle$, whose only role is to monitor the population of the excited states. The matrix elements (dipole approximation) of the interaction Hamiltonian are thus $V_{xg} = \frac{1}{2}\mu_x \epsilon_x(t) e^{-i\nu t} + c.c.$, $V_{yg} = \frac{1}{2}\mu_y \epsilon_y(t) e^{-i\nu t} + c.c.$, $V_{xx} = V_{yy} = V_{gg} = 0$, and $V_{xy} = V_{yx} = 0$ where μ_x and μ_y are dipole moments of the $|v\rangle \rightarrow |x\rangle$ and $|v\rangle \rightarrow |y\rangle$ transitions respectively; $\epsilon_x(t) = \epsilon_0(t)\cos\alpha$ and $\epsilon_y(t) = \epsilon_0(t)\sin\alpha$ are the electric field envelopes along the x and y directions, respectively; and α is the polarization angle [Fig.3.5(b)]. The dynamics of the system are described using the density matrix formalism. For convenience we define the vector $\vec{S} = (U_1, U_2, U_{xy}, V_1, V_2, V_{xy}, W_1, W_2)$ which contains the Bloch vectors $U_1 = \rho_{xv} e^{i\nu t} + c.c., V_1 = i\rho_{xv} e^{i\nu t} + c.c., W_1 = \rho_{xx} - \rho_{vv}$ and $U_2 = \rho_{xyv} e^{i\nu t} + c.c., V_2 = i\rho_{yv} e^{i\nu t} + c.c., W_2 = \rho_{yy} - \rho_{vv}$ of the $|v\rangle \rightarrow |x\rangle$ and $|v\rangle \rightarrow |y\rangle$ transitions [5], respectively, and $U_{xy} = \rho xy + c.c.$ and $V_{xy} = -i\rho xy + c.c.$. Within the rotating wave approximation, $\vec{S}$ obeys the equation of motion [8, 48]

$$\dot{\vec{S}} = M(t)\vec{S}(t) - \Gamma\vec{S}(t) - \vec{\Lambda} \tag{3.1}$$

in which

$$\Gamma = \begin{pmatrix} \frac{1}{2}\gamma_x & \frac{1}{2}\gamma_{xy} & 0 & \delta_x & 0 & 0 & 0 & 0 \\ \frac{1}{2}\gamma_{xy} & \frac{1}{2}\gamma_y & 0 & 0 & \delta_y & 0 & 0 & 0 \\ 0 & 0 & \frac{1}{2}(\gamma_x + \gamma_y) & 0 & 0 & -\Delta & \frac{1}{3}\gamma_{xy} & \frac{1}{3}\gamma_{xy} \\ -\delta_x & 0 & 0 & \frac{1}{2}\gamma_x & \frac{1}{2}\gamma_{xy} & 0 & 0 & 0 \\ 0 & -\delta_y & 0 & \frac{1}{2}\gamma_{xy} & \frac{1}{2}\gamma_y & 0 & 0 & 0 \\ 0 & 0 & \Delta & 0 & 0 & \frac{1}{2}(\gamma_x + \gamma_y) & 0 & 0 \\ 0 & 0 & \frac{1}{2}\gamma_{xy} & 0 & 0 & 0 & 0 & 0 \\ 0 & 0 & \frac{1}{2}\gamma_{xy} & 0 & 0 & 0 & 0 & 0 \end{pmatrix} \tag{3.2}$$

and $\vec{\Lambda} = (0, 0, \frac{2}{3}\gamma_{xy}, 0, 0, 0, \frac{1}{3}\gamma_x, \frac{1}{3}\gamma_y)$ account for the various decay rates and the detuning [Fig. 3.5(a)]. Since we are concerned with the time-evolution of $\vec{S}$ caused by tailored laser pulses, we consider the general situation when the SQD is excited by a pair of pulses with mutual phase delay $\phi = 2\pi\nu t_d$. M(t) then reads:

$$M = \frac{1}{2} \begin{pmatrix} 0 & 0 & -\Omega_{y2}\sin\phi & 0 & 0 & -\Omega_{y1} + \Omega_{y2}\cos\phi & -2\Omega_{x2}\sin\phi & 0 \\ 0 & 0 & -\Omega_{x2}\sin\phi & 0 & 0 & \Omega_{x1} + \Omega_{x2}\cos\phi & 0 & -2\Omega_{y2}\sin\phi \\ \Omega_{y2}\sin\phi & \Omega_{x2}\sin\phi & 0 & \Omega_{y1} + \Omega_{y2}\cos\phi & \Omega_{x1} + \Omega_{x2}\cos\phi & 0 & 0 & 0 \\ 0 & 0 & -\Omega_{y1} + \Omega_{y2}\cos\phi & 0 & 0 & \Omega_{y2}\sin\phi & -\Omega_{x1} - 2\Omega_{x2}\cos\phi & 0 \\ 0 & 0 & -\Omega_{x1} - \Omega_{x2}\cos\phi & 0 & 0 & -\Omega_{x2}\sin\phi & 0 & -2(\Omega_{y1} + \Omega_{y2}\cos\phi) \\ \Omega_{y1} + \Omega_{y2}\cos\phi & \Omega_{x1} - \Omega_{x2}\cos\phi & 0 & -\Omega_{y2}\sin\phi & \Omega_{x2}\sin\phi & 0 & 0 & 0 \\ 2\Omega_{x2}\sin\phi & \Omega_{y2}\sin\phi & 0 & 2\Omega_{x1} + 2\Omega_{x2}\cos\phi & \Omega_{y1} + \Omega_{y2}\cos\phi & 0 & 0 & 0 \\ \Omega_{x2}\sin\phi & 2\Omega_{y2}\sin\phi & 0 & \Omega_{x1} + \Omega_{x2}\cos\phi & 2(\Omega_{y1} + \Omega_{y2}\cos\phi) & 0 & 0 & 0 \end{pmatrix} \tag{3.3}$$

For laser pulses with hyperbolic secant time profile, the instantaneous Rabi frequencies $\Omega_{x1} = (\mu_x/\hbar)\cos\alpha_1\epsilon_{01}\mathrm{sech}((t-t_0)/\tau_p)$ and $\Omega_{y1} = (\mu_y/\hbar)\sin\alpha_1\epsilon_{01}\mathrm{sech}((t-$

$t_0)/\tau_p)$ describe the interaction of the first pulse with the $|v\rangle \rightarrow |x\rangle$ and $|v\rangle \rightarrow |y\rangle$ transitions, respectively, while $\Omega_{x2} = (\mu_x/\hbar)\cos\alpha_2\epsilon_{01}\text{sech}((t - t_0 - t_d)/\tau_p)$ and $\Omega_{y2} = (\mu_y/\hbar)\sin\alpha_2\epsilon_{01}\text{sech}((t - t_0 - t_d)/\tau_p)$ account for the interaction of the second pulse with the same transitions. The temporal width τ_p of the pulses is maintained constant but the polarization angles α_1 and α_2 of the two pulses are variable.

Under single-pulse excitation, i.e. when $\Omega_{x2} = \Omega_{y2} = 0$, a simple analytical solution exists, assuming no decoherence and no detuning ($\Gamma = 0, \vec{\Lambda} = 0$). It is convenient to define the effective polarization angle $\alpha_{eff} = \arctan(\frac{\mu_y \sin\alpha}{\mu_x \cos\alpha})$, effective input pulse area $\theta_{eff}(t)$ and effective transition dipole moment μ_{eff},

$$\theta_{eff}(t) = (\mu_{eff}/\hbar)\int_{-\infty}^{t} \epsilon(t')dt' \tag{3.4}$$

$$\mu_{eff} = \sqrt{\mu_x^2 \cos^2\alpha + \mu_y^2 \sin^2\alpha} \tag{3.5}$$

The solutions of Eq.3.1, in terms of the populations of $|x\rangle$ and $|y\rangle$ then read:

$$\begin{cases} \rho_{yy} = \sin^2\alpha_{eff}\sin^2(\frac{1}{2}\theta_{eff}), & \rho_{xx}(0) = \rho_{yy}(0) = 0; \\ \rho_{xx} = \cos^2\alpha_{eff}\sin^2(\frac{1}{2}\theta_{eff}), & \rho_{xx}(0) = \rho_{yy}(0) = 0; \end{cases} \tag{3.6}$$

$$\begin{cases} \rho_{yy} = \sin^2(2\alpha_{eff})\sin^4(\frac{1}{4}\theta_{eff}), & \rho_{xx}(0) = 1; \\ \rho_{xx} = [1 - 2\cos^2\alpha_{eff}\sin^2(\frac{1}{4}\theta_{eff})]^2, & \rho_{xx}(0) = 1; \end{cases} \tag{3.7}$$

Furthermore, if $\alpha_{eff} = \pi/4$, the population difference between the two substates has the general form,

$$\rho_{yy} - \rho_{xx} = (\rho_{yy}(t_0) - \rho_{xx}(t_0))\cos(\frac{1}{2}\theta_{eff}) \tag{3.8}$$

Equations 3.6, 3.7, and 3.8 reveal three interesting characteristics of the population oscillation as a function of θ_{eff}, in this system: (i) the populations of

$|x\rangle$ and $|y\rangle$ oscillate with the same period (i.e. Rabi frequency) even though $\mu_x \neq \mu_y$. (ii) The effective transition dipole moment μ_{eff} of $|v\rangle \rightarrow |xy\rangle$ is tunable in the range $[\mu_x, \mu_y]$, with $|xy\rangle = a|x\rangle + b|y\rangle$. (iii) The period of the population oscillations is 2π when $\rho_{xx}(0) = 0$ and is 4π when $\rho_{xx}(0) = 1$. The population oscillations of $|x\rangle$, $|y\rangle$, and $|v\rangle$ are depicted in Fig. 3.6 as a function of θ_{eff} for various initial conditions and polarization angles. When $(\rho_{yy}(0) = \rho_{xx}(0) = 0, \alpha_{eff} = 0)$ [Fig. 3.6(a)], the excitation field only couples to the $|v\rangle \rightarrow |x\rangle$ transition and the system undergoes the familiar two-level Rabi oscillations. On the other hand, when $(\rho_{yy}(0) = \rho_{xx}(0) = 0, \alpha_{eff} = \pi/4)$ [Fig. 3.6(b)], the two transitions are coupled, yet the populations of $|x\rangle$ and $|y\rangle$ simultaneously undergo oscillations. Finally, under asymmetrical initial conditions $(\rho_{yy}(0) = 1, \alpha_{eff} = \pi/4)$ [Fig. 3.6(c)], coherent population flopping between $|x\rangle$ and $|y\rangle$ occurs, even though $\langle x|y\rangle = 0$. In practice, these results are quantitatively affected by decoherence, inevitably present in the system. For experimental comparison we thus have to resort to numerical integration of Eq. 3.1 using the two-pulse matrix $M(t)$ in which the first pulse acts as an initialization pulse for the case $\rho_{xx}(0), \rho_{yy}(0) \neq 0$. Dephasing prevents initialization into a stationary state, and instead brings the system into a superposition state which is allowed to freely evolve in the non-rotating frame. Therefore, the relative phase between the two pulses plays an important role and is reflected in the data by fine-time PL oscillations.

The polarized PL signals are shown in Fig. 3.7 as a function of input pulse area without any pre-pulse [Fig. 3.7(a)(b)(c)], and with a y-polarized

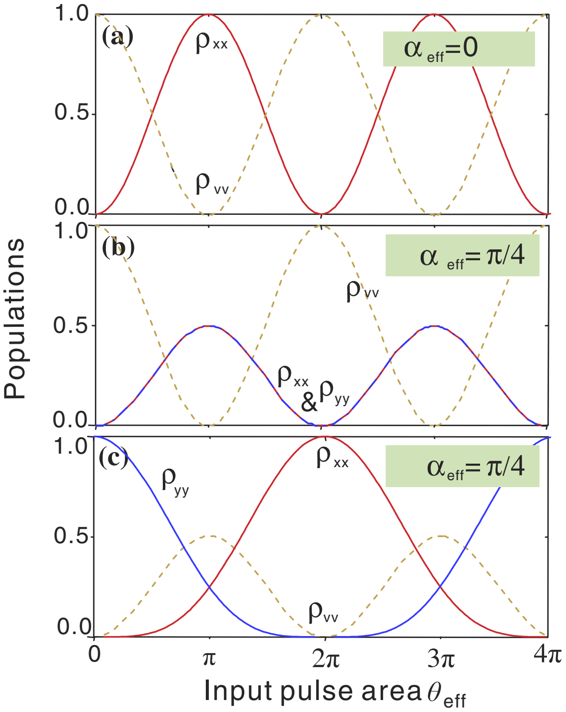

Figure 3.6: Theoretically computed evolution of $|x\rangle$, $|y\rangle$, and $|v\rangle$ in the V-type system.

π-pre-pulse [Fig. 3.7(d)(e)(f)]. In both cases, the polarization of the manipulation pulse was fixed at $\alpha = \pi/4$ while its pulse area was varied by changing the laser intensity.

In the absence of a pre-pulse, both PL(x) and PL(y) oscillate with the same period as expected for ρ_{xx} and ρ_{yy} [Eq. 3.6], and their difference, PL(x)-PL(y) almost vanishes [Fig. 3.7(c)]. The latter behavior validates the assumption that spin-relaxation is negligible during the carrier relaxation from the exciton excited state to the exciton ground state. The population oscillations are also strongly damped due to dephasing processes which have been included in the simulated oscillations [solid curves in Fig. 3.7(a)(b)], obtained from numerical integration of Eq.3.1. This damping reflects the breakdown of the ideal two-level quantum dot model [157, 158]. Using a y-polarized π-pre-pulse, the initial condition $\rho_{yy} = 1$ can be simulated. The second pulse ($\alpha = \pi/4$) then induces population dynamics in the system governed by $M(t)$ [Eq. 3.3], leading to the phase-sensitive evolution of the polarized PL [Fig. 3.6(d)(e)]. The coarse delay between the pulses was fixed at 12 ps to prevent mutual temporal overlap while their phase delay was varied with a piezo-controlled fine-time delay and the maxima (diamonds) and minima (squares) of PL(y) and PL(x) recorded [Fig. 3.7(d) and Fig. 3.7(e), respectively]. The phase-averaged values $\langle \text{PL}(x) \rangle$ and $\langle \text{PL}(y) \rangle$ are also plotted [dashed curves in Fig. 3.7(d)(e)]. These represent the general trend for the population transfer, namely the population of state $|y\rangle$ decreases at the expense of $|x\rangle$, corresponding to the population swapping without direct transition described by Eq. 3.8

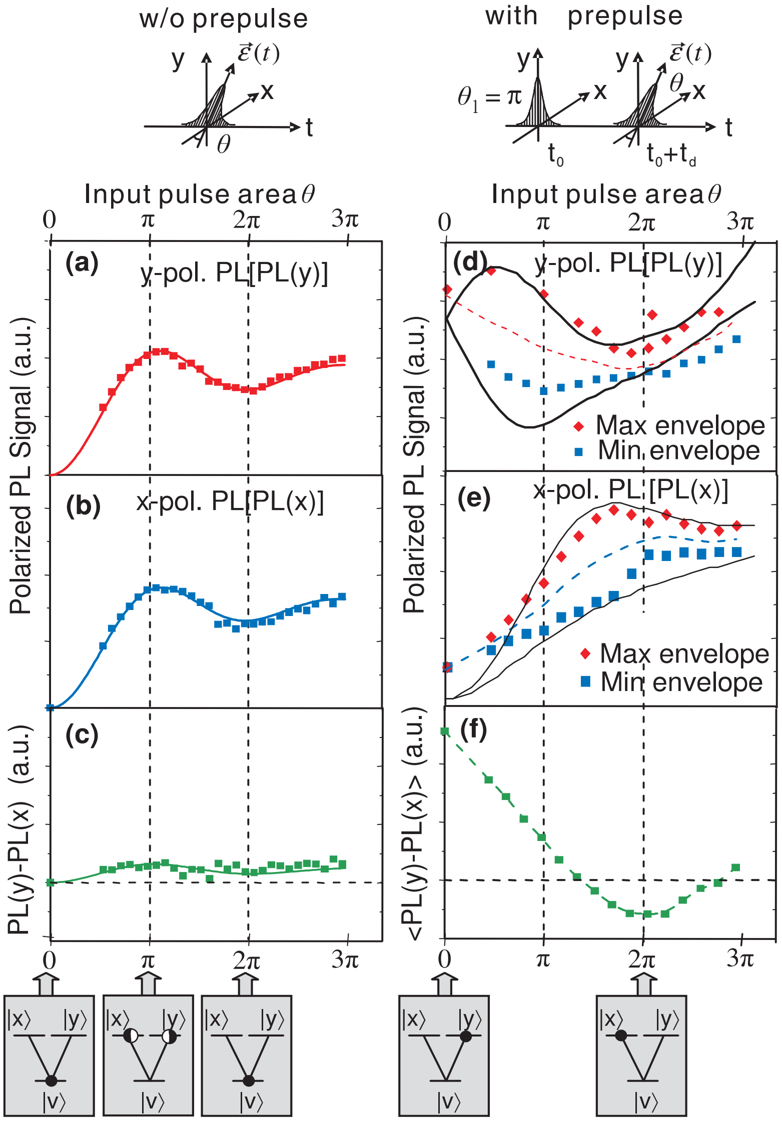

Figure 3.7: Experimentally measured evolution of the populations in the V-system with and without a π-pre-pulse.

and Fig. 3.6(c). Numerical integration of Eq. 3.1, including dephasing, reproduces the envelopes of the oscillations reasonably well [solid curves in Fig. 3.7(e)(f)].

The complex dynamics of this population transfer has its roots in the coupling between the Π_x and Π_y transitions via the common ground state $|v\rangle$. The strength of this coupling can be represented by the normalized quantity $f_c = 1 - \frac{W_{1,max} - W_{2,max}}{W_{1,max} + W_{2,max}}$. There is no coupling ($f_c = 0$) when $\alpha_{eff} = 0$ or $\pi/2$, in which case the V-type three-level system reduces to a two-level system. The coupling reaches a maximum ($f_c = 1$) when $\alpha_{eff} = \pi/4$. The difference of the third component of the two coupled optical Bloch vectors will then oscillate in the form $W_1(t) - W_2(t) = (W_1(t_0) - W_2(t_0)) \cos(\theta_{eff}/2)$ [Eq. 3.8], with the initial value set by the polarized pre-pulse. Indeed, this is what is observed experimentally and reflected in the difference $\langle$PL(y)-PL(x)$\rangle$ between the polarized PL signals [Fig. 3.6(f)].

As is well-known in SQDs, the anisotropic exchange interaction is responsible for the splitting of the originally degenerate heavy-hole exciton spin states $|m_h = 3/2\rangle$ and $|m_h = -3/2\rangle$, into the states $|x\rangle = (|m_h = 3/2\rangle + |m_h = -3/2\rangle)/\sqrt{2}$, and $|y\rangle = (|m_h = 3/2\rangle - |m_h = -3/2\rangle)/\sqrt{2}$ [14]. The coherent manipulation of the populations of $|x\rangle$ and $|y\rangle$ with tailored pulses is thus equivalent to a manipulation of the excitons spin state, with control over both phase and amplitude of the quantum states. In conclusion, we have examined both theoretically and experimentally the exciton dynamics arising under polarization-tailored two-pulse excitation of the V-system defined by the polarization eigenstates $|x\rangle, |y\rangle$ and the crystal ground state $|v\rangle$. This system is special in that the coupling between the otherwise orthogonal states $|x\rangle$ and $|y\rangle$ can be polarization-tuned. Although dephasing affects the detailed time-evolution, the essential characteristics are captured by the analytic solution to the density matrix equations with $\Gamma, \vec{\Lambda} = 0$. The capabilities demonstrated here present an additional step towards all-optical non-linear coherent control of a multilevel excitonic system.

Chapter 4

Resonance Fluorescence

An atom excited resonantly by a monochromatic laser emits "resonance fluorescence". A central topic in the early development of quantum optics, resonance fluorescence was first comprehensively described by Mollow [108] and subsequently observed from atomic beams [162]. Particularly interesting and counter-intuitive is the situation in which the driving field is strong enough for the light-matter coupling to overcome dephasing, giving rise to a non-linear response. In this case, the two-level systems, although damped as an ensemble as a result of being out of phase with each other, continue to oscillate individually at the Rabi frequency and thus generate sidebands in the emission spectrum. In the resulting Mollow triplet, the side peaks are displaced by the Rabi frequency, as if the system were acting as a modulator to the incoming field [107]. Resonance fluorescence and related phenomena, particularly in the strongly driven regime, play a crucial role in current topics of quantum information science. For example, any scheme for deterministic generation of single photons, strictly requires the capability to coherently manipulate a quantum state of the system, while simultaneously harvesting its fluorescence [102].

Although large efforts are under way to make use of semiconductor based two-level systems, such as quantum dots (QDs) [104], which can readily provide efficient single photon emission [106, 130], indistinguishability between photons [128], electrically-controlled single photons [170], polarization-entangled photon pairs [2, 138], and cavity-enhanced single photon emission [41, 56, 136], the fundamental phenomenon of resonance fluorescence has not yet been realized. The main obstacle is isolating the fluorescence from laser scattering at the same frequency associated with defects, surface contaminants, crystal imperfections, etc., that constitutes an insurmountable background signal. While significant progress has been made in probing the coherent optical properties of the exciton ground state using techniques such as differential transmission [140], differential reflectivity [152], four-wave mixing [28], photodiode spectroscopy [173], stark-shift modulation absorption spectroscopy [3], and other methods [121], none of these techniques is able to harvest the fluorescence.

This report presents an experimental geometry that effectively eliminates the same frequency background by placing the dots in a planar microcavity and using a geometry similar to that in atomic physics, where excitation and collection are performed orthogonally. It combines the advantages of pump-probe techniques, which measure the state but not the emission, and standard photoluminescence (PL), which collects the emission but cannot probe the state resonantly. With this technique we are able to unambiguously characterize the properties of the resonance fluorescence from individual dots

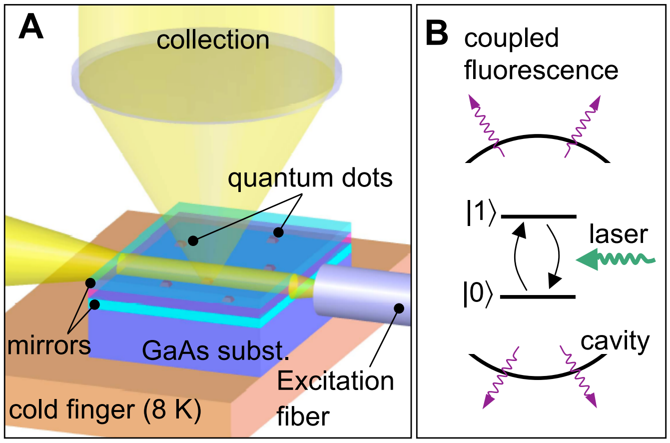

Figure 4.1: Experimental setup and energy level schematic of quantum dot in a cavity.

in both weak and strong excitation regimes.

We employ self-assembled InGaAs QDs grown epitaxially between two distributed Bragg reflectors of moderate reflectivity (Fig. 4.1). While the sample [160] is maintained at low temperature in a He flow cryostat, a single mode optical fiber, mounted on a three-axis inertial walker at room temperature, is brought within a few microns of the cleaved sample edge. An in-plane polarized tunable continuous-wave Ti:Sapphire laser is introduced through the fiber to excite the dots; it couples efficiently into the high index semiconductor and propagates deeply before diverging appreciably. The QD emission is then collected by a conventional micro-PL setup equipped with a two-dimensional charge coupled device (CCD) detector mounted on an imaging spectrograph [71]. We focus here on QDs coupled to a cavity mode centered around 920 nm, with a quality factor of about 250. For first-order correlation measurements, a

Mach-Zehnder interferometer is inserted into the collection beam path. When the laser is frequency-scanned over the excitonic ground-state of a single QD, the resonance fluorescence is observed as a bright peak, localized both spectrally and spatially in the CCD images. This is in contrast to the remaining background laser light, which appears as a faint vertical (i.e. spatially delocalized) line. Shown in Fig. 4.2A are a series of such CCD images, at increasing excitation energy. The laser bandwidth is less than 40 MHz, so that the total integrated intensity as a function of detuning, plotted explicitly in Fig. 4.2B, measures the homogeneous linewidth of the ground state transition. For this particular dot we obtain a full width at half maximum (FWHM) of 2.8 μeV ($T_2 = 480$ ps) at 4.7 K. A strong dependence on temperature is observed (Fig. 4.2C) and all subsequent measurements are performed at 10 K. Finally, we note that second-order correlation measurements, performed on single peaks using a Hanbury-Brown and Twiss setup [106], reveal a pronounced anti-bunching dip (Fig. 4.2D), confirming their single emitter nature.

4.1 Theoretical Description

The interaction of a single QD with an external, near resonant electric field is described using the optical Bloch equations in which the field is treated semi-classically and the dipole approximation is assumed [132]. Assessing the validity of this description, particularly when the field is strong, characterizes much of the progress in the field of coherent QD spectroscopy in the past decade. Milestone experiments include the demonstration of quantum inter-

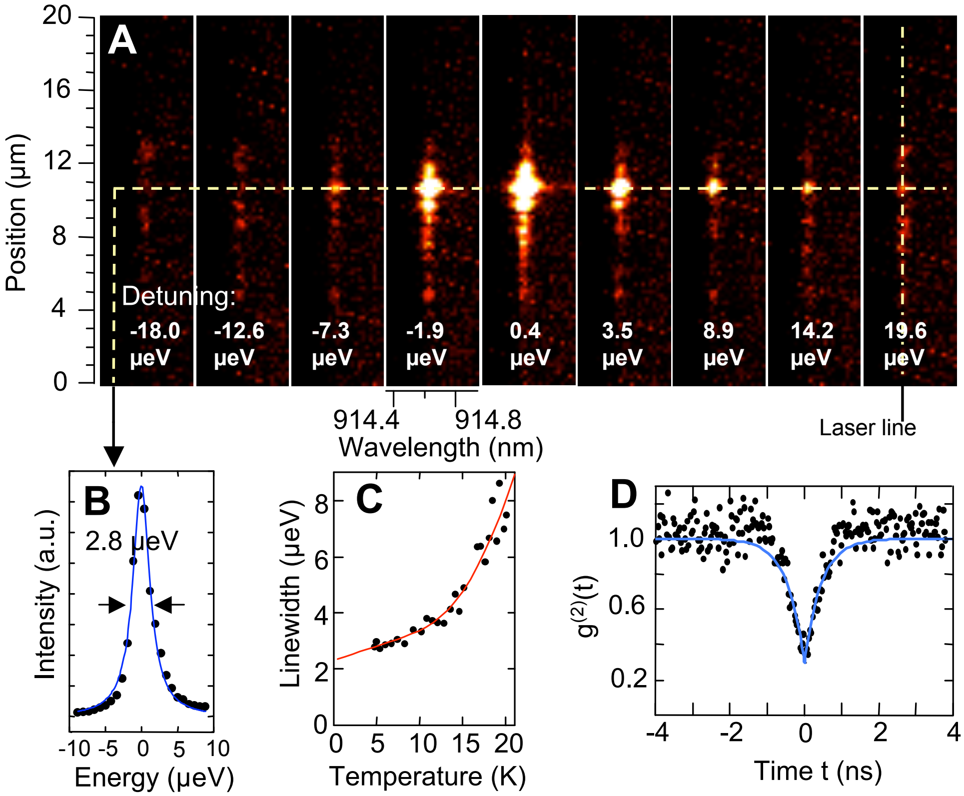

Figure 4.2: Resonance fluorescence from a single quantum dot.

ference [25], Rabi oscillations [29, 70, 74, 121, 140, 173], the optical Stark effect [152], Ramsey Fringes [147], as well as multilevel manipulation schemes such as two-photon Rabi oscillations [91]. At low intensity, a harmonic driving field with constant amplitude, E_0, which may be detuned from the transition frequency of the two-level system by an amount $\Delta\omega = \omega - \omega_0$, first increases the population of the upper state. When the field is strong enough that the Rabi frequency $\Omega = \mu E_0$ exceeds the total decoherence rate $1/T_2$ in the system, however, the probability to find it in the upper state reaches a maximum before decreasing again. Here μ denotes the dipole moment of the transition, whose resonance frequency is ω_0. In fact, both the populations and the coherences of the system then oscillate at the Rabi frequency, which in the language of quantum computation corresponds to quantum bit rotations. Written out explicitly in the rotating wave approximation, the Bloch equations for the upper and lower state populations, $n(t) = \mathrm{Tr}\{\rho(t)|1\rangle\langle 1|\}$ and $m(t) = \mathrm{Tr}\{\rho(t)|0\rangle\langle 0|\}$, and for the coherence, $\alpha(t) = \mathrm{Tr}\{\rho(t)|0\rangle\langle 1|\}$, read:

$$\begin{aligned} \tfrac{d}{dt}n(t) &= -i\tfrac{\Omega}{2}(\alpha(t) - \alpha^*(t)) - \tfrac{n(t)}{T_1} \\ \tfrac{d}{dt}\alpha(t) &= -i\tfrac{\Omega}{2}(n(t) - m(t)) + i\alpha(t)\Delta\omega - \tfrac{\alpha(t)}{T_2} \end{aligned} \tag{4.1}$$

Here $\rho(t)$ is the density operator, and T_1 and T_2 denote, as usual, the diagonal and off-diagonal phenomenological damping constants, respectively. Note that we use the notation of Ref. [108].

4.1.1 Time-Independent Properties of Resonance Fluorescence

The quasi steady-state solutions of Eqs. 4.1 are obtained as:

$$\begin{aligned} n_{\infty}(\Delta\omega) &= \tfrac{1}{2}\tfrac{\Omega^2 T_1/T_2}{\Delta\omega^2 + T_2^{-2} + \Omega^2 T_1/T_2} \\ \alpha_{\infty}(\Delta\omega) &= \tfrac{i\Omega}{2}\tfrac{1/T_2 + i\Delta\omega}{\Delta\omega^2 + T_2^{-2} + \Omega^2 T_1/T_2} \end{aligned} \tag{4.2}$$

and describe well-known saturation phenomena which are directly observed in the experiments with single dots, since the time-averaged fluorescence intensity is proportional to $n_{\infty}(\Delta\omega)$. Specifically, one can see that (i) the total integrated fluorescence at resonance ($\Delta\omega = 0$) saturates once the square Rabi frequency substantially exceeds the quantity $(T_1 T_2)^{-1}$, (ii) that the linewidth of the Lorentzian in Eq. 4.2 increases slowly with the square root of intensity, a phenomenon known as power broadening, and (iii) that the low intensity limit of the linewidth equals $2/T_2$. All the theoretical details are given in Appendix C.

4.1.2 The Resonance Fluorescence Spectrum and the First Order Correlation Function

More interesting is the actual shape of the fluorescence spectrum, which goes far beyond the straightforward steady-state solutions. In fact, while the optical Bloch equations are directly borrowed from nuclear magnetic resonance theory, a comprehensive theoretical description of resonance fluorescence was only given in 1969 [108]; a fully quantized theory followed [78]. Mollow first showed that the resonance fluorescence spectrum is properly computed as the Fourier transform of the two-time (first-order) correlation function

$g(t,\tau) = \langle a^\dagger(t)a(t+\tau)\rangle$ of the field emitted by the system, where $a(0) = |0\rangle\langle 1|$, which can be reduced to the calculation of single time expectation values using the quantum regression theorem [132]. Here we use a Mach-Zehnder interferometer to measure the correlation function directly, whose form can be found analytically, and on resonance reads:

$$g(\tau) = |\alpha_\infty(0)|^2 + \frac{n_\infty(0)}{2}e^{-\tau/T_2} + n_\infty(0)e^{-\tau(1/T_1+1/T_2)/2}\{N\cos(\Omega'\tau) + M\sin(\Omega'\tau)\} \tag{4.3}$$

where N and M denote constants that depend on T_1, T_2, and Ω, and $\Omega' = \sqrt{\Omega^2 - (1/T_1 - 1/T_2)^2/4}$ is a generalized Rabi frequency. When $\Omega \ll 1/T_2$, then $g(\tau)$ reduces to a simple exponential decay, with decay constant T_2, corresponding to a Lorentzian spectral line profile of FWHM $2/T_2$. When $\Omega \gg 1/T_2$, on the other hand, the system is in the strong excitation regime and $g(\tau)$ is oscillatory. Note that T_1 and T_2 are related through $T_2^{-1} = (2T_1)^{-1} + \gamma$, where γ denotes pure dephasing (i.e. loss of coherence without population decay). The corresponding power spectrum, known as the Mollow triplet, is the Fourier transform of the correlation function [108].

4.2 Experimental Observations

For the same dot as in Fig. 4.2A, the absorption linewidth is plotted as a function of intensity in Fig. 4.3A to illustrate power broadening. As mentioned in the discussion of Eq. 4.2, the value of T_2 can be obtained from the low intensity limit of the linewidth; here $T_2 = 380$ ps. If is also known, these measurements provide the proportionality constant between the excita-

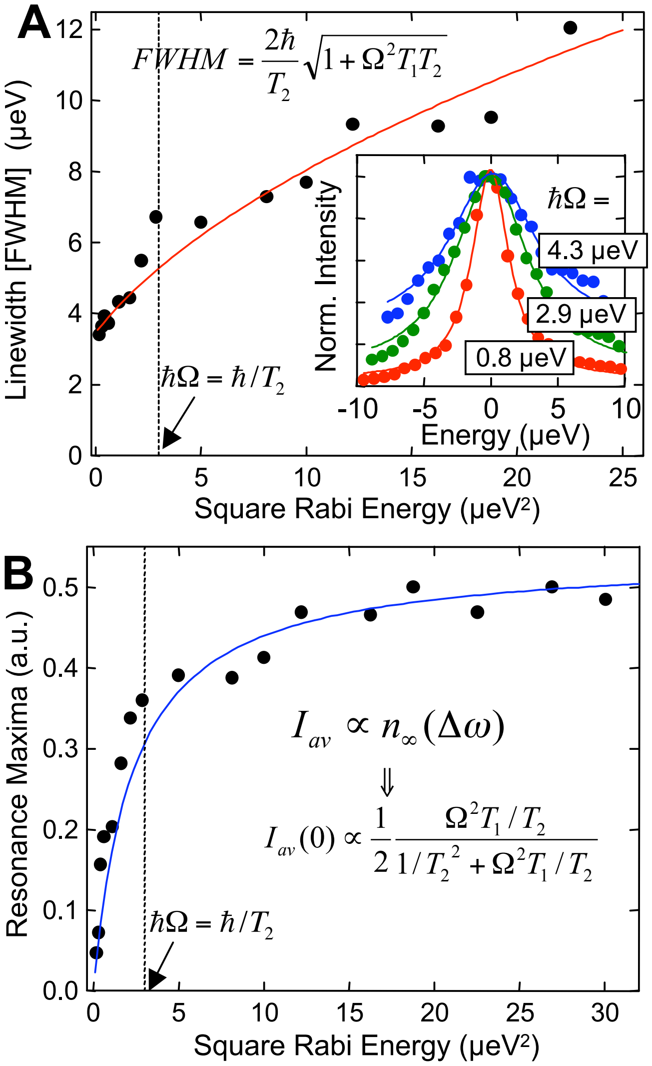

Figure 4.3: Power broadening and saturation for a single dot.

tion intensity and the square Rabi frequency. We assume here that $T_1 = 450$ ps for the particular dot studied, and plot our data as a function of Ω directly. This is consistent with time-resolved measurements of other QDs in the same sample, and with temperature dependent measurements (Fig. 4.2C) on the same dot, which definitely reveal the presence of some amount of pure dephasing that might arise due to phonon-related broadening or other effects such as spectral diffusion. The emission intensity as a function of excitation intensity is plotted in Fig. 4.3B and clearly shows the population saturation behavior predicted by Eq. 4.2 at intensities such that $\Omega \gg (T_1 T_2)^{-1}$. Noted on the graphs of Fig. 4.3 are the thresholds for reaching the strong excitation regime.

To measure $g(\tau)$, the fluorescence is interfered with itself using the interferometer. The length of one of the arms, and thus the time delay between them, is varied coarsely over a number of points with a highly stable translation stage, and finely using a piezo actuator to record the fringe contrast at each point (schematic of Fig. 4.5A). The actual setup is also shown in Fig. 4.4. Such a technique, borrowed from Fourier transform spectroscopy [76, 128, 175], can routinely provide an equivalent spectral resolution of about 1 μeV, much smaller than is available with conventional grating-based spectrometers. For the same dot as in Figs. 4.2 and 4.3, we now examine the resulting fringe contrast as a function of time delay, which is directly proportional to $g(\tau)$. It is plotted in Fig. 4.5, B to G, for various excitation intensities, i.e. Rabi energies.

When the intensity is weak, i.e. in the regime $\Omega \ll 1/T_2$, a single expo-

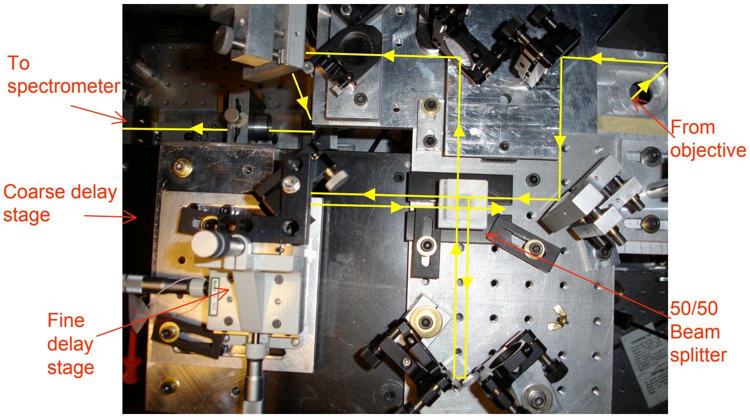

Figure 4.4: Photograph of actual interferometer.

nential decay is obtained. In contrast, as the Rabi frequency is increased, the fringe contrast develops an oscillatory feature whose frequency is the modified Rabi frequency, Ω', defined above, which approximately equals Ω if $\Omega \gg 1/T_2$. The system is sufficiently coherent to observe several oscillations, analogous to the observation of a distinctive Mollow triplet. We illustrate this by plotting the corresponding power spectrum at each excitation intensity in Fig 4.5, using the values $T_1 = 500$ ps, $T_2 = 380$ ps, and the Rabi energy obtained from the oscillation in the correlation data; it is as large as 16 μeV for the highest intensity.

We expect that our results could be substantially improved quantitatively by using, for example, more strongly confined QDs, which may provide even longer coherence times. In addition, we are also limited here by our interferometer which can currently only scan over 12 cm (800 ps delay), thus restricting our measurements, particularly for very weak intensities. Increas-

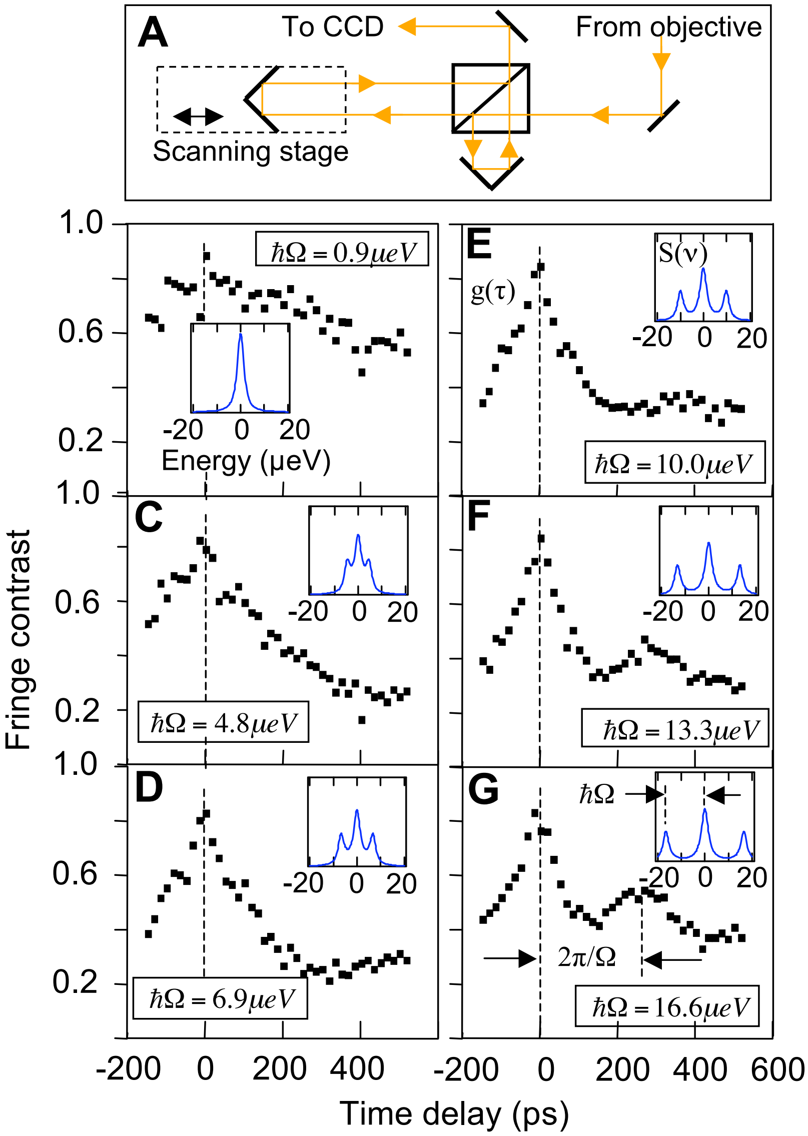

Figure 4.5: Resonance fluorescence in the strong excitation regime: the Mollow triplet.

ing the excitation intensity further is currently not possible due to power-broadened nearby dots, but this could also be overcome simply by using lower density samples. Nevertheless, for a homogeneous linewidth of only 3.5 μeV, and Rabi energies as high as 16 μeV, which are achieved here, the QD is already very attractive for a number of experiments. Second order measurements in the strong excitation regime, for instance, would reveal coherent oscillations in the anti-bunching trace [132]. We speculate that a single QD in strong resonance fluorescence might serve as an ultra high-speed single photon source, whose repetition rate would be tunable simply by changing the excitation intensity. With a modulation frequency of 5 GHz ($\hbar\Omega = 20.7\mu$eV) and higher it would substantially exceed traditional sources operating in the sub GHz regime which are ultimately limited by radiative recombination. Alternatively, one might be interested in quantum optical experiments of greater complexity, such as squeezing, which involves interfering the fluorescence with a reference laser [132]. Using a three dimensional microcavity instead of a simple planar structure would enable advanced experiments relying on cavity quantum electrodynamic effects, many of which have been proposed for quantum information processing applications. This might be achieved straightforwardly with all-epitaxial microcavities [110], whose bulk morphology is ideally suited to introduce a waveguided laser.

4.3 Conclusions

The measurement technique presented here, that of laterally excited quantum dots in a microcavity, realizes the goal of resonant coherent control of a quantum dot ground state while simultaneously collecting the fluorescence. Using this method in concert with Fourier transform spectroscopy we have achieved the first measurement, in a single solid-state two-level system, of resonance fluorescence. In the strong excitation regime, oscillations in the first-order correlation function are clearly visible in the interference data and correspond to a Mollow triplet split by a Rabi energy up to 16 μeV. Low-background resonant measurements open up many possible applications of coherent control that are impossible with pump-probe or simple photoluminescence techniques.

Chapter 5

Cavity-Coupled Quantum Dots

This section presents our results with novel quantum dot containing microcavity samples grown by the group of Prof. Deppe. These structures are distinguished from previous approaches by their buried morphology, and we refer to them often as "all-epitaxial" microcavities [110–112].

5.1 The "All-Epitaxial" Design

To fabricate the microcavities, mesas were initially defined by electron-beam lithography in a layer containing InAs self-assembled QDs, grown epitaxially onto a lower AlAs/GaAs semiconductor mirror [Fig. 5.1(a)]. The lateral size of these mesas was varied down to a diameter D ~0.5 μm. After etching, the mesas were covered under proper epitaxial growth conditions with an upper semiconductor mirror, to form a fully epitaxial microcavity. Here the longitudinal confinement is controlled essentially by the number of quarter-wave pairs in the upper layer. The lateral confinement, on the other hand, is provided by the step in cavity height at the mesa edge. Consider the schematic of Fig. 5.1(b), in which $\vec{k} = (\vec{k}_\perp, \vec{k}_z)$ and $\vec{\kappa} = (\vec{\kappa}_\perp, \vec{\kappa}_z)$ denote the propagation constants inside and outside the mesa region, respectively. Since

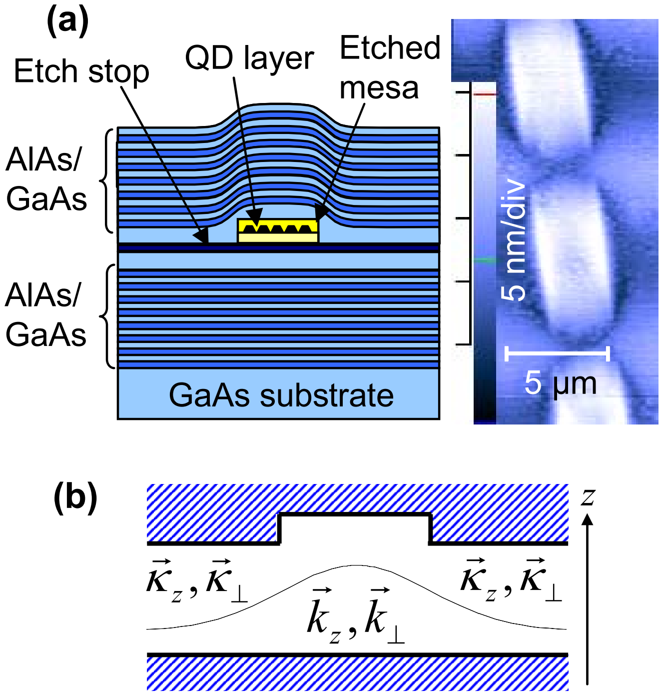

Figure 5.1: Schematic and AFM image of an all-epitaxial microcavity.

$k_z < \kappa_z$, there exist solutions to $\omega/c = \sqrt{k_z^2 + k_\perp^2} = \sqrt{\kappa_z^2 + \kappa_\perp^2}$ (given real $k_\perp$) for which $\kappa_\perp$ is imaginary. These bound solutions are actually identical to those obtained assuming an effective index step at the mesa edge, but without the detrimental effects of surface states or interface defects [96]. In fact, the epitaxial growth conditions can be controlled to fully isolate single QDs and create a truly single QD microcavity light source [111]. In addition, quality factors in excess of 30,000 have been achieved for larger devices [112]. This may seem surprising at first sight, in light of the lens-like shape that the mesa assumes as it is overgrown, as shown in the atomic force microscope (AFM) images [95]. However, as discussed below, the cavity itself nevertheless remains cylindrical to a large extent. Because the intended mesa size can be significantly undercut after etching, we use the minor axis dimension as obtained from the atomic force (AFM) images [Fig. 5.1(a)] to specify the cavity size.

5.2 Modeling

Another way of looking at the confinement provided by the all-epitaxial cavities is through Gaussian beam optics. Appendix E is dedicated to the details of this description, and the present section summarizes the results.

As the AFM images reveal, the overgrown surface morphology approximates a dome, or spherical shape (Fig. 5.2). Indeed we can therefore view the cavities as consisting of one planar and one spherical mirror. The spherical mirror's radius of curvature can also be estimated from the nominal parameters such as the lithographic mesa diameter and the mesa height. If we assume

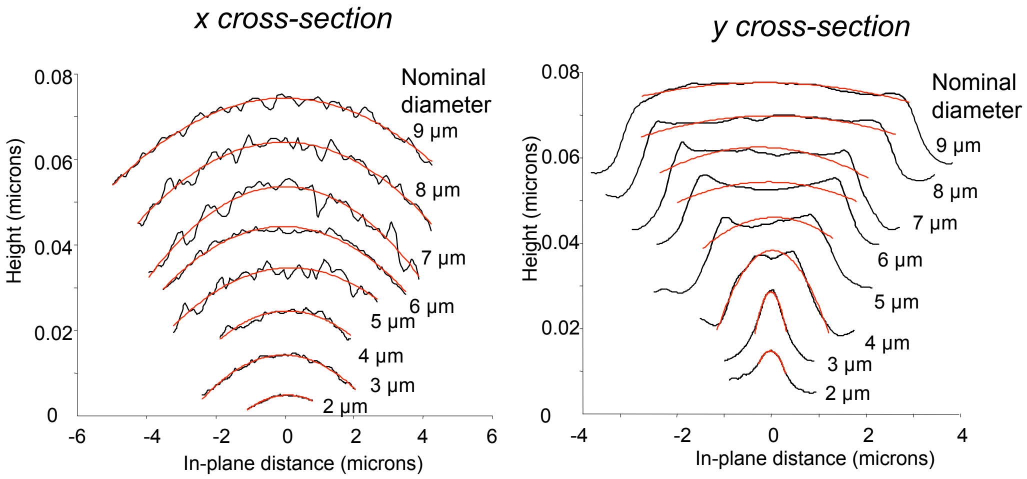

Figure 5.2: Cross-sections of overgrown cavity from AFM measurements.

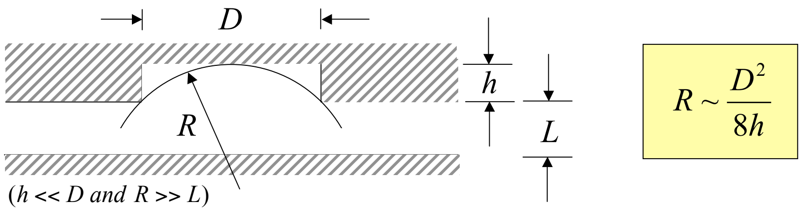

Figure 5.3: Sketch of cavity cross-section before overgrowth.

that these more or less define the final structure sphericity we can use the approximations shown in Fig. 5.3.

The Gaussian beam formalism, based on the paraxial wave equation can then be used to find the resonant frequencies of the cavities. What we actually need here, is a somewhat modified solution which takes into account the different radii of curvature of the overgrown surface, which is obviously best characterized by two radii, along [110] and [$\bar{1}$10]. The details of such an

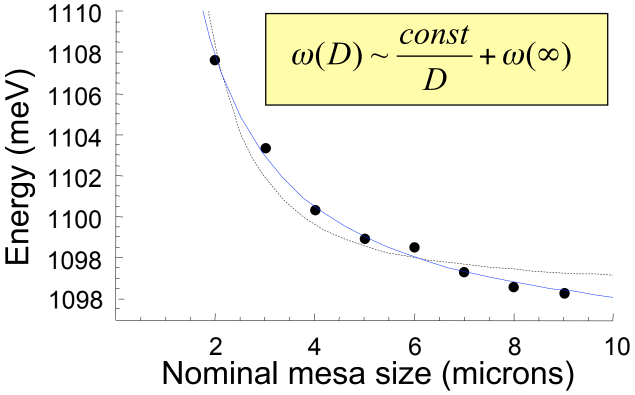

Figure 5.4: Fundamental mode versus frequency.

approach are given in the appendix. The solution for the lowest order modes reads:

$$\omega_{q0l} = \frac{\pi c}{L} q + \frac{c}{L} \times \begin{cases} (l+1)\left(\sqrt{L/R_1} + \sqrt{L/R_2}\right)/2 & l \text{ even} \\ \frac{l+1}{2}\sqrt{L/R_1} + \frac{l}{2}\sqrt{L/R_2} & l \text{ odd} \end{cases}$$

and is plotted for the fundamental mode in Fig. 5.4 Interestingly, we can a dependence which goes as $\omega(D) \sim const/D + \omega(\infty)$, whereas we would have gotten a dependence of the form $\omega(D) \sim \sqrt{const/D^2 + \omega^2(\infty)}$using an effective index model.

Furthermore, we plot the complete set of mode for a particular cavity and compare theory and experiment. This is shown in Fig. 5.5. On the other hand, we can compare the energies of a few modes for different mesa sizes. In this case, the experimental modes are shown in Fig. 5.6 and the theoretical modes are shown in Fig. 5.7.

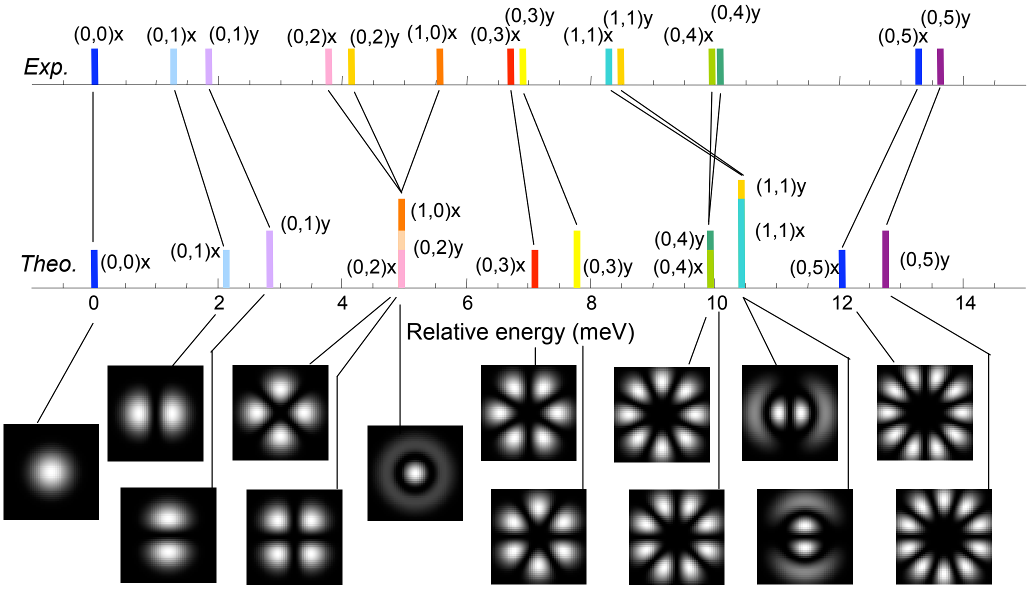

Figure 5.5: Experimental vs. theoretical mode energies for a particular microcavity size.

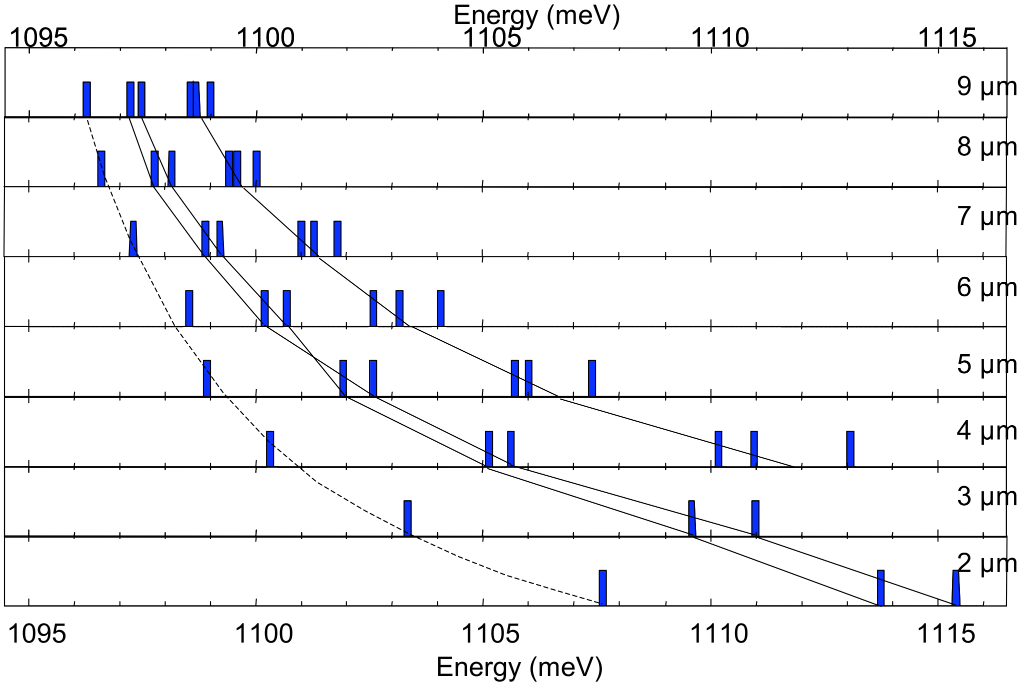

Figure 5.6: Mode energies as a function of size, experimental.

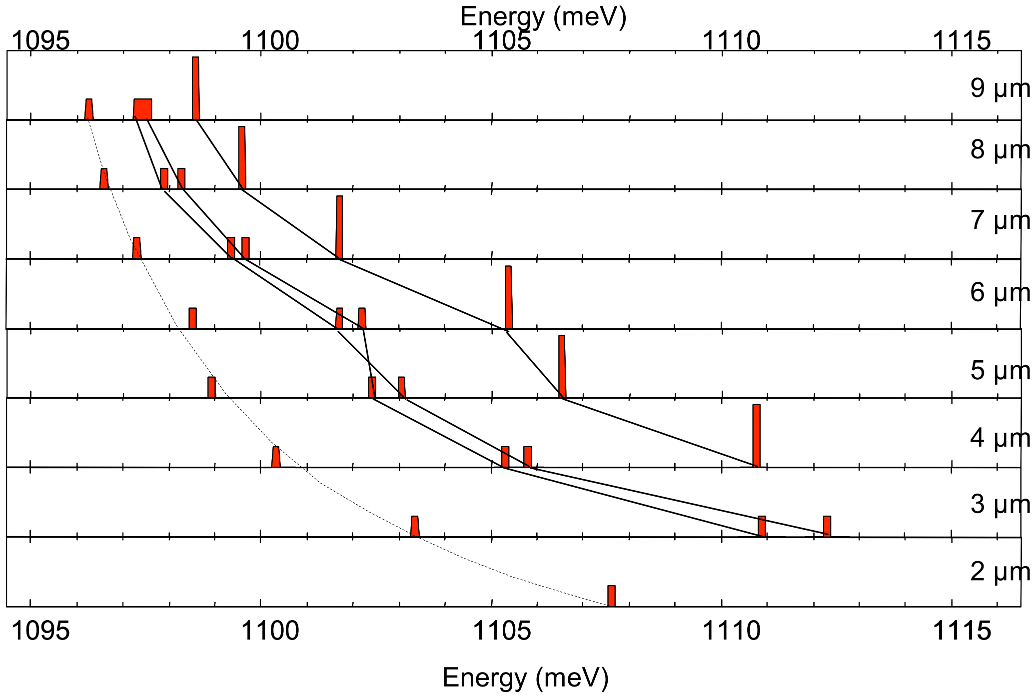

Figure 5.7: Mode energies as a function of size, theoretical.

5.3 Mode Imaging and Characterization

The modal characteristics were studied for various mesa sizes in the high-Q embodiment of the cavity (sample A). Maintained at liquid-He temperatures, the sample was excited with a pulsed Ti-Sapphire laser above the GaAs band-edge. The photoluminescence (PL) signal was dispersed by a 0.5 m spectrograph and imaged onto a two-dimensional array detector so that the spatial dimension along the spectrograph slit was preserved. Figure 5.8 shows the spatially integrated spectra of individual cavities with diameters ranging from D=3.5 μm to D $\sim$0.1 μm. The blue shift and the increased mode spacing are the result of increased optical confinement in the plane of growth. The actual field distribution for each mode was analyzed from the spectrally-resolved mode images. These were reconstructed from a series of spectral images recorded while scanning across the slit and are shown in Fig. 5.8 linked to their spectral peak (D=3.5 μm cavity). They closely resemble the linearly polarized LP$_{nm}$ modes of a quasi-cylindrical waveguide (only one polarization component is shown), and are labeled accordingly, with 2n azymuthal, and m-1 radial zeros. Even though the ellipticity of the overgrown mesa was found to increase with decreasing mesa size, the field distribution remains surprisingly cylindrical. In fact, the lens shape does not cause a dramatic drop in Q compared to the planar structure (inset of Fig. 5.8) [112]. Note that although we strictly measure the far-field instead of the near-field distribution [94, 172], only a minor quantitative difference is expected [40]. From the mode images in Fig. 5.8 for the smaller cavities it is also readily

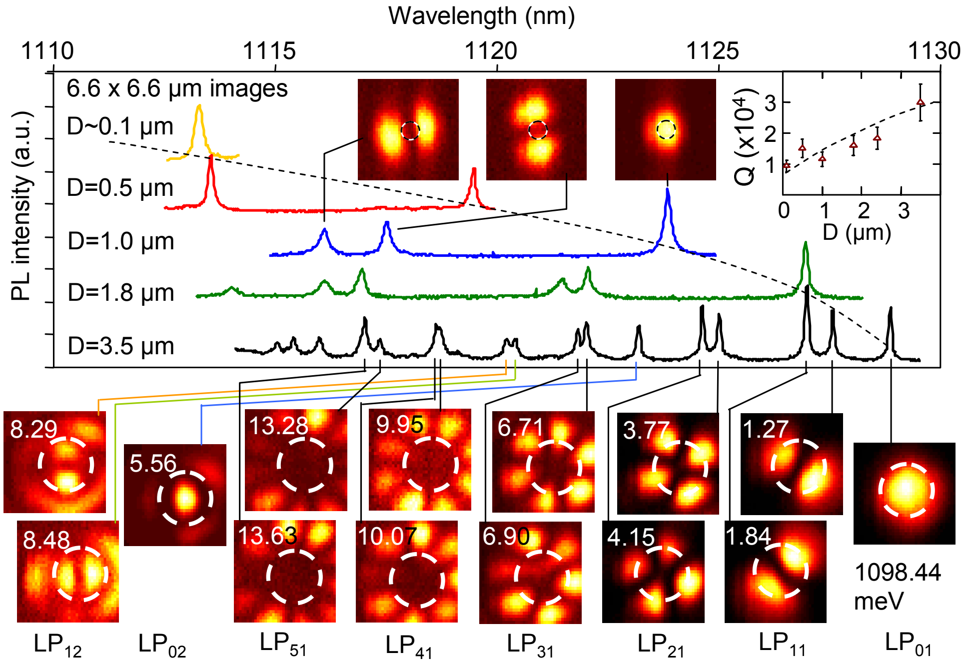

Figure 5.8: Mode spectrum and images for various cavity sizes.

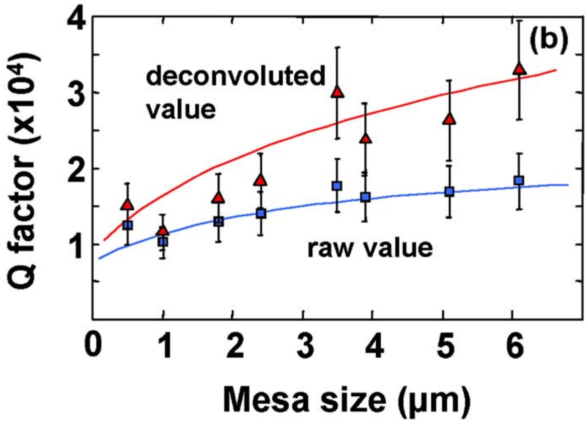

Figure 5.9: Quality factor as a function of mesa size.

observed how the QDs, restricted to the mesa region, are automatically placed at the optimum location (in the lateral direction), i.e. at the anti-node of the electric field of the fundamental cavity mode. This self-alignment eliminates the problem of spatial overlap between emitter and cavity mode, frequently encountered in other systems.

5.4 Lasing in High Q Resonators

The quality factors ($Q = \omega/\Delta\omega$), obtained from the Lorentzian linewidth of the PL peaks, are further studied for mesas of various sizes. Plotted in Fig. 5.9, are the Qs of individual cavities with decreasing size, measured at sufficiently low excitation intensity so as to exclude linewidth narrowing effects due to lasing [131]. The values range from $Q \sim$ 33,000 for the largest cavities with ∼6 μm mesas down to Q ∼10,000 for cavities based on 0.5 μm diameter mesas. Both the raw and deconvoluted values are shown. The highest Q values exceed those of a recent report based on three-halves wavelength cavity spacers.5 The high Q combined with high quality QDs are key to obtaining QD VCSELs with a single active layer. Although the Q decreases with mesa size similar to reports for other microcavity systems [93, 126, 131], the present measurements indicate that for the smallest mesas that contain only a single QD [95, 111] entering the strong coupling regime [118, 123, 125, 169] may be feasible with this all-epitaxial lithographically defined QD microcavity. This is especially important since this microcavity eliminates the reliability problem caused by surface degradation in etched micropillars [125], and increases the thermal conductivity and mechanical robustness over a photonic crystal approach [169]. The Q values compare well with the highest obtained for micropillar [93, 131], microdisk [137], and photonic crystal QD microcavities [169].

The lasing characteristics are studied under experimental conditions similar to the ones described above with the temperature typically maintained at ∼35 K. Previous studies of etched-pillar [93, 131] or oxide-apertured microcavities [142] have not demonstrated lasing, even with multiple QD active layers. The VCSEL operation with a single QD active layer suggests that either the passive Q in the present microcavities is higher, or the QD quality is better, or possibly both. In Fig. 5.10(a) the light out versus pump intensity curves for 6.1 μm and 5.1 μm diameter cavities are shown on linear and log-log plots (inset). The largest average powers incident on the sample were on the

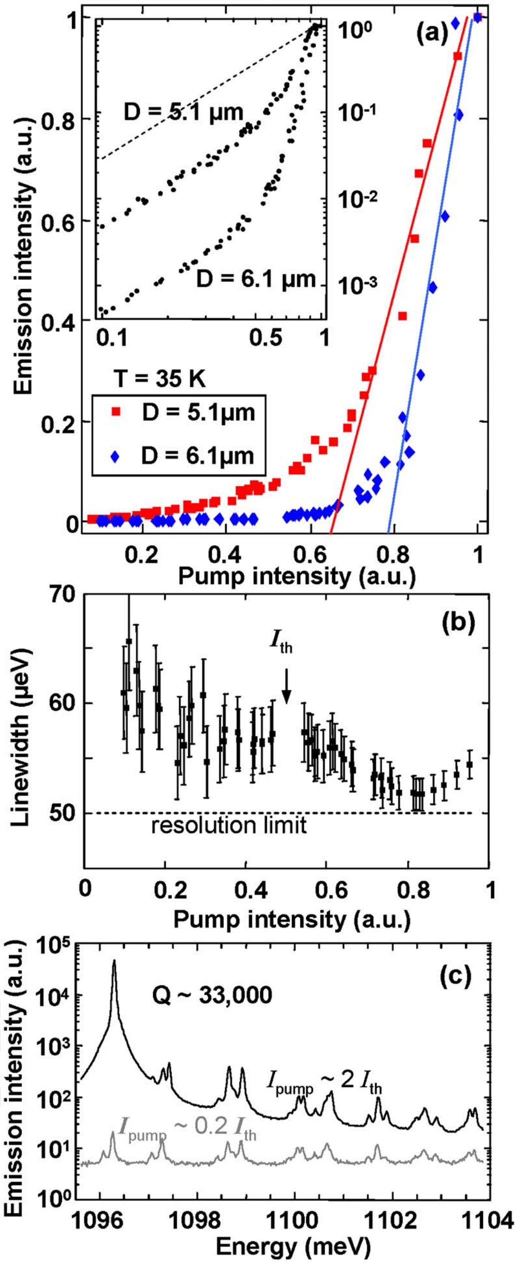

Figure 5.10: Lasing characteristics.

order of ~10 mW (corresponding to $\sim 5(10)^8$ W peak power at 80 Mhz repetition rate and 6 ps pulse widths), while the laser spot (780 nm) was focused to a ~20 μm diameter spot. However, a meaningful value for the actual intensity at the QD location is difficult to estimate due to the pump absorption in the large number of overgrown layers, and the intensity scale is therefore left in arbitrary units. As the threshold is approached, a pronounced linewidth narrowing is also observed as shown for the D=6.1 μm cavity in Fig. 5.10(b). The linewidth decreases to values close to the spectrometer resolution (~50 μeV) and a weak increase is observed at the highest pump powers, most likely due to heating effects. The spectral features below and above threshold are shown in Fig. 5.10(c). The laser emission, which is highly linearly polarized, generally occurs at the fundamental mode only. Some cavities in the array, however, have been found to lase on higher order modes as well, and multimode lasing has been observed at temperatures exceeding 200 K. The threshold and lasing characteristics also change with temperature mostly because of the spectral overlap between the inhomogeneously broadened gain profile of the QDs and the cavity resonances. In agreement with the targeted spectral match around ~100 K, the lasing threshold first decreases in the temperature range from 5-100 K and later increases. With a structure for which the gain is spectrally matched to the fundamental cavity mode, lasing is expected to occur at temperatures that can be obtained with thermoelectric cooling and possibly room temperature.

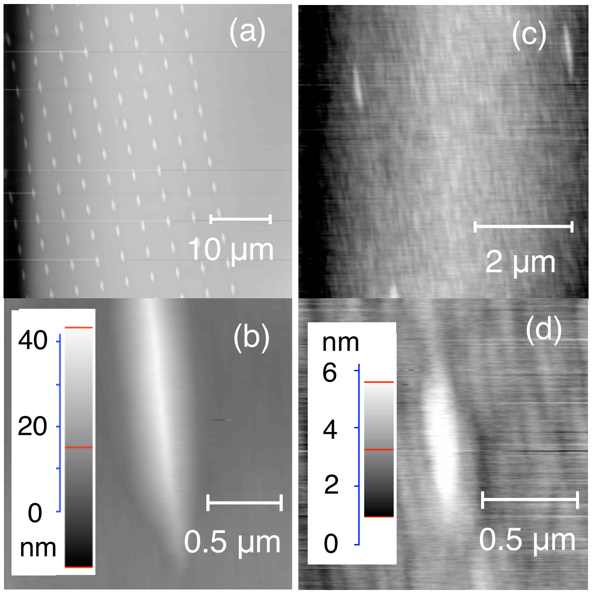

Figure 5.11: AFM images of 0.5 μm and 0.1 μm microcavities.

5.5 Isolation of Single Quantum Dots

When the diameter of the mesas on which the cavities are based is sufficiently decreased, few or even only single dots can be contained [111]. We focus here on two sizes, 0.5 μm and 0.1 μm diameter, whose overgrown structure is revealed by the AFM images of Fig. 5.11.

Emission from the arrays are studied using a He-Ne laser exciting a 1 mm diameter spot, and from the single QD microcavities using a focused Ti:Sapphire laser. Figure 5.12 shows a plot of the measured cavity resonance in wavelength and integrated intensity versus mesa size. The spectral tuning between the cavity frequency and QD transitions depends on temperature, and resonance is achieved between 77 and 100 K for all except the smallest

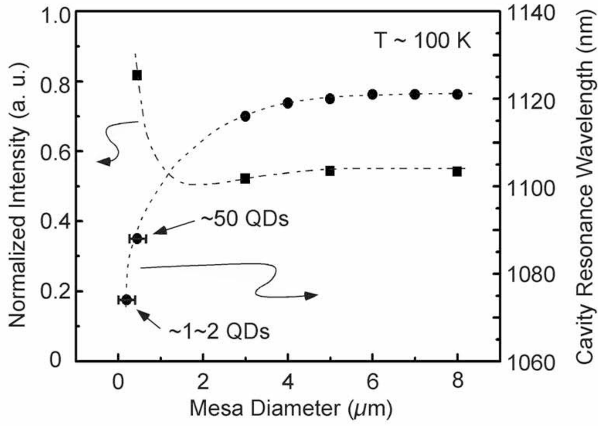

Figure 5.12: Size dependence of emission wavelength and intensity for the smallest microcavities.

microcavities. For the larger microcavities the array emission intensity when normalized by the fill factor of the mesas shows only a slight decrease in efficiency for decreasing mesa size for sizes ≥ 4 μm, indicating that nonradiative recombination due to the QD microcavity fabrication is low. For microcavities smaller than ~ 1 μm diameter the emission intensity and efficiency can be increased due to the Purcell effect. The increase in efficiency observed for the array of 0.5 μm mesa QD microcavities as compared to the larger sizes is ~ 50 percent. The Q's of the cavities are measured to be ~ 50, while the effective cavity length can be estimated from the field penetration into the semiconductor mirrors as $L \approx 1.5\lambda_0/n$. Therefore the emission into the 0.5 μm QD mesa cavity can also be estimated from the blue-shifted frequency as also increasing by $\tau_{sp,cav}^{-1}/\tau_{sp,bulk}^{-1} \approx 0.5$. The blue-shift in cavity resonance is therefore consistent with and provides a measure of the expected increased in emission due to the Purcell effect. Also from Fig. 5.12, the blue-shift of the smallest microcavities based on the 0.1 μm mesa, given a fixed cavity length, corresponds to lateral mode diameters of $\sim$0.4 μm, and can therefore place QDs at the centers of these smallest microcavity confined modes. Note that in commercial applications, such as quantum key distribution, operation at temperatures that can be reached by thermoelectric cooling ($\geq$150 K) is highly desirable. But since the single QD homogeneous linewidth is already a few meV at these temperatures [30], and because the Purcell enhancement saturates once the cavity linewidth becomes smaller than QD linewidth, the quality factor, Q, required of single photon sources for quantum security is only a few hundred for standard fiber optic wavelengths.

While the emission intensity is uniform for the 0.5 μm diameter and larger QD mesa microcavities, it is not for the $\sim$0.1 μm mesa microcavities. Figure 5.13 shows the spatial intensity patterns from either (a) the 0.5 μm or (b) the 0.1 μm QD mesa microcavities. While the 0.5 μm diameter QD mesas contain $\sim$50 QDs as indicated by the spectral emission in Fig. 5.13(c), the smallest 0.1 μm mesa microcavities show nonuniform emission intensity due to the actual number of QDs contained in the mesa, and this number may be only one or two, or even zero QDs.

The spectrum of a mesa with precisely one QD is displayed in Fig. 5.13(d) for various excitation intensities. With increasing excitation intensity, many peaks appear due to multiparticle states of the dot, and eventually turn into S and P-like bands [124]. Only the peak visible at low powers, labeled

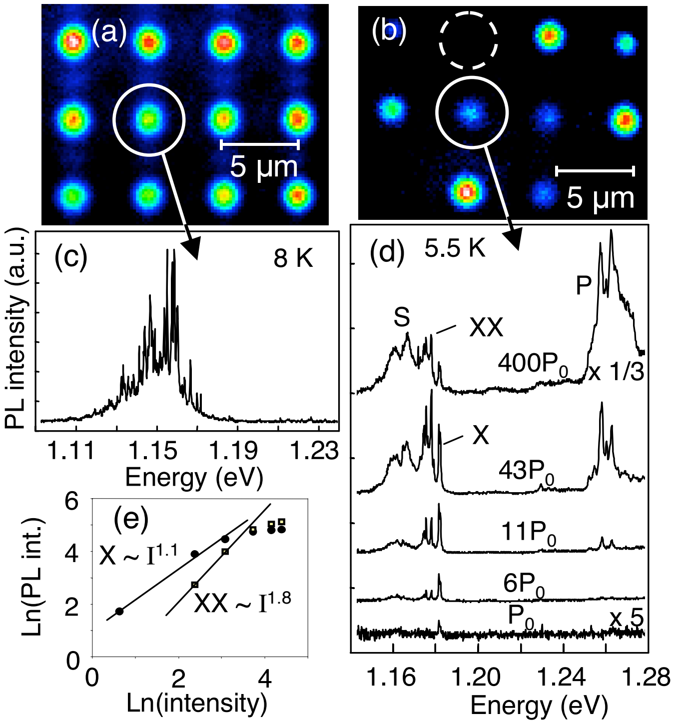

Figure 5.13: Single dot spectra for 0.1 μm and 0.5 μm.

by "X" increases linearly with excitation intensity [Fig. 5.13(e)]. The features appearing at higher intensity have a non-linear (In) intensity dependence. For example, the peak labeled "XX" corresponds to emission from a bi-excitonic state, and increases roughly with the square of the excitation intensity [Fig. 5.13(e)]. Furthermore, temperature-dependent PL studies (data not shown) indicate that the PL features remain sharp and prominent above 100 K. These measurements illustrate the feasibility of single QD all-epitaxial nano-cavities with desirable optical properties for quantum light sources [18, 122, 129, 170].

5.6 Time-Resolved Measurements: The Purcell Effect

To study the cavity-emitter coupling at the single QD level, we turn to a different sample (sample B), which was initially fabricated from a high-reflectivity back mirror and a low-reflectivity top mirror, yielding a low Q value of $\sim$50. The advantage of using a lower Q is that the spectral peaks from single QDs can then be readily identified underneath the cavity resonance. The spectrum of a single cavity, which contains $\sim$50 QDs is shown in Fig. 5.14(a). Due to the small mode volume (mesa diameter $\sim$0.5 μm), a weak Purcell effect can already be observed using time-resolved measurements. These were recorded using a Si avalanche photodiode (APD) and time counting electronics with an overall instrument response function (IRF) of $\sim$0.4 ns such that decay times down to $\sim$0.2 ns can be measured with reasonable accuracy by deconvolution. The spectrally-resolved PL lifetime of the QDs is observed to gently map out the cavity resonance and varies from $\sim$1 ns, the free-space lifetime, τ_{free}, down to $\sim$0.8 ns.

The (single mode) Purcell spontaneous emission enhancement is usually written as [56],

$$\frac{\tau_{free}}{\tau_{cav}} = F_p \frac{\Delta\omega_c^2}{4(\omega_e - \omega_c)^2 + \Delta\omega_c^2} \frac{|\vec{E}(\vec{r}_e)|^2}{|\vec{E}|^2{}_{max}} \tag{5.1}$$

where $\Delta\omega_c = \omega_c/Q$ and $\Delta\omega_e$ are the cavity and QD linewidths, respectively. The figure of merit, F_p, for this enhancement can be expressed near resonance as [56] (also see J. M. Gérard in [104]),

$$F_p = \frac{3(\lambda_c/n)^3}{4\pi^2 V}(Q^{-1} + \Delta\omega_e/\omega_e)^{-1} \tag{5.2}$$

and depends primarily on the cavity mode volume, V, the semiconductor index, n, the wavelength, λ_c, and the cavity quality factor Q. In addition to its dependence on F_p, the Purcell enhancement in Eq. 5.1 is sensitive to the factor $\frac{|\vec{E}(\vec{r}_e)|^2}{|\vec{E}|^2{}_{max}}$ which denotes the normalized field distribution function of the cavity mode at the position, $\vec{r}_e$, of the emitter. This quantity is often set to unity, and perfect placement is assumed. Here, the function $|\vec{E}(\vec{r})|^2$ is directly obtained from experiment as demonstrated in Fig. 5.8 and we therefore retain this factor and study its effect on the Purcell enhancement. For details on Eq. 5.1 and Eq. 5.2, see the appendix on cavity-QED.

An increase in coupling is obtained by a second mirror overgrowth on the same sample (B). This procedure, which could in principle be repeated many times, allows for fine tuning Q and brings additional control into the fabrication process. As can be seen in the spectrum of a single cavity in Fig. 5.14(b), a mode structure similar to what is observed in sample A is then

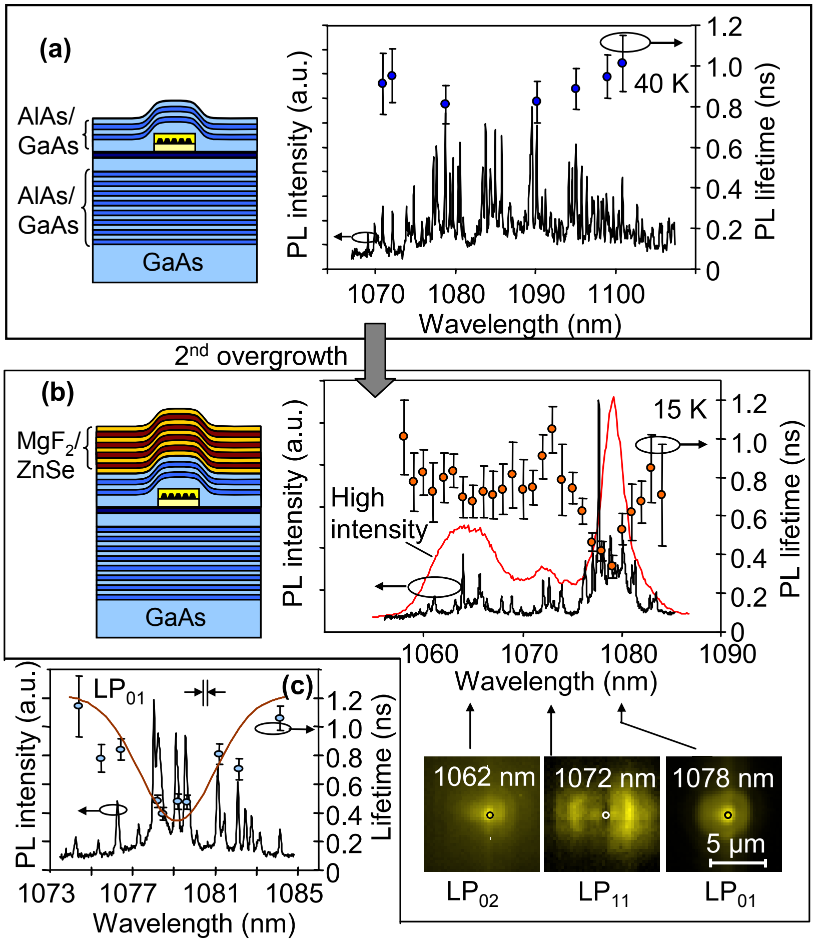

Figure 5.14: Time-resolved measurements and PL images of single cavities of the low-Q embodiement.

revealed. Here, pumping the QDs harder makes it possible to decorate the cavity spectrum [solid line in Fig. 5.14(b)]. Mode imaging identifies three basic mode patterns corresponding to the fundamental LP$_{01}$ mode as well as higher order modes, and a pronounced Purcell spontaneous emission enhancement is measured. This enhancement, however, differs significantly between modes. Assuming perfectly matched dipole and field polarization, as well as optimal resonance, Eq. 5.1 actually predicts three main contributions to this Purcell enhancement, due to Q, V, and $\frac{|\vec{E}(\vec{r}_e)|^2}{|\vec{E}|^2{}_{max}}$. For each mode shown in the figure, these quantities can be estimated. The quality factor is determined from the spectral mode width under high excitation intensity, and the relative mode volume and field at the QD location are extracted from the mode images (Table 5.1). Most interesting is the total absence of Purcell enhancement for QDs coupled to the LP$_{11}$ mode, which is due to the spatial mismatch between the QDs (confined to the mesa region indicated by circles in the images of Fig. 5.14) and the spatially extended cavity mode. Both the quality factor and mode volume are actually different between modes. However, the factor accounting for the field profile dominates by far. It can be noticed for instance that the quality factor of the LP$_{11}$ mode (which shows no Purcell effect) is close to LP$_{01}$ and much higher than LP$_{02}$. On the other hand the lower Q LP$_{02}$ mode already shows a measurable Purcell effect due to the better field alignment than the LP$_{11}$ mode. Because the mode images are limited by diffraction we are only able to give a relative mode volume between the two modes. Nevertheless, the fact that neither the quality factor nor the mode

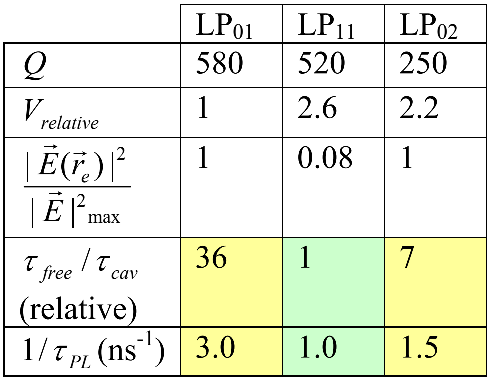

	LP_{01}	LP_{11}	LP_{02}
Q	580	520	250
$V_{relative}$	1	2.6	2.2
$\frac{\lvert\vec{E}(\vec{r}_e)\rvert^2}{\lvert\vec{E}\rvert^2{}_{\max}}$	1	0.08	1
τ_{free}/τ_{cav} (relative)	36	1	7
$1/\tau_{PL}$ (ns^{-1})	3.0	1.0	1.5

Table 5.1: Purcell enhancement parameters.

volume change dramatically between modes (compared to the field envelope) can be observed with much more confidence in larger cavities (see for example Fig. 5.8), where the diffraction limit does not play an important role. Quantitatively, the measured Purcell enhancement is not as high as the theoretical value, which is common in the literature. Nevertheless, the current result captures qualitatively very well the variations in Purcell enhancements due to the factor $\frac{|\vec{E}(\vec{r}_e)|^2}{|\vec{E}|^2{}_{max}}$ in Eq. 5.1. Finally, to illustrate the capability of addressing single QD states, high resolution time-resolved PL decay traces were recorded nearby an LP_{01} resonance [Fig. 5.14(c)]. The spectral features due to individual QD transitions are resolution limited here and can be selectively detected, for example to probe for single photon emission.

The largest Purcell emission enhancement demonstrated in the present proof-of-concept experiment approaches $\frac{\tau_{free}}{\tau_{cav}}$. However, the quality factor, which could be substantially increased as demonstrated in sample A, is not necessarily a limiting factor to the optimal operation of a Purcell-enhanced single photon source. In fact, at temperatures at which real devices would operate, i.e. T >150 K, the QD linewidth, $\Delta\omega$, already amounts to several meV [28], so that increasing Q above a few hundred does not increase F_p due to saturation in Eq. 5.2. For the same reason, the contribution of the detuning factor in Eq. 5.1 gets to play a less important role because of increased spectral overlap with temperature. Therefore, the most determinant parameters in this case are the mode volume and the value of the mode function at the QD position. Because the mode volume can be substantially reduced using smaller mesas, a significant improvement in Purcell enhancement can be expected. In fact, the smallest mesas that can contain a single QD and yet isolate it from the crystal surfaces exposed in the fabrication require ∼0.1 μm, and have already been fabricated [111]. Lifetimes in the <50 ps range can be extrapolated from current data using conservative estimates but actual measurements will require improved instrumental time-resolution and likely shortening of the emission wavelength to the high-sensitivity region of the Si APDs. The quality factor could nevertheless be increased for low-temperature measurements and we anticipate that the capabilities demonstrated here could be extended to achieve and study in a controlled way the strong coupling between a single QD and a single cavity mode that leads to vacuum Rabi oscillations [118, 123, 125, 169]. In addition, a stepwise increase in Q, could be used in many contexts for controlled coupling between a single dot and a single cavity mode. For example it may often be more systematic and convenient to first isolate a

QD with the desirable properties in a low-Q sample, and then step up the Q by successive depositions of quarter-wave pairs. This capability is somewhat unique to the all-epitaxial microcavity due to the planar geometry, and can avoid blind temperature tuning in a high-Q sample.

Chapter 6

Outlook and Conclusions

After a decade of research dedicated to self-assembled quantum dots, it still remains unclear whether they will one day fulfill their promise as building blocks for future quantum computers which require an error rate of no more than 10^{-4} per quantum operation. As of now, it appears that superconducting Josephson-junction qubits would be a more promising alternative. Nonetheless, even in that case, it remains a formidable challenge to achieve the required precision.

As it stands, however, it seems that self-assembled QDs could make remarkably good nanophotonic sources for modern optoelectronics. It is hopeful that operation of single photon sources can be extended into the telecom band and to room temperature environments in the near future, or at least into a regime in which thermoelectric cooling can be used. Particularly feasible would be the utilization of self-assembled QDs in commercial devices that might rely on quantum optical effects. Moreover, even if a scalable computer cannot be realized, few-qubit gates, some of which have already been demonstrated, could be used for example in interfaces that form an intermediate link between ingle photon communication channels and a full-scale quantum computer. From a larger perspective, quantum computation serves as a common goal that, even though not readily achievable, enables otherwise unexplored new physical insight into solid-state quantum optics.

This work explored both the coherent control aspects as well as the quantum optical features of self-assembed QDs. Rabi oscillations and the capability to manipulate the population and coherence of single QDs within the dephasing time were demonstrated. In conjunction with measurements of the ground state emission, such coherent control leads to fascinating quantum optical effects such as Mollow fluorescence, as was shown here. This was possible due to a simple technical improvement of the setup, which relies on side-excitation of the sample and the placement of dots into a planar microcavity for waveguiding and enhanced QD emission. Additionally, a new optical microcavity structure was investigated in great detail, and was shown to enable high Q, isolation of single dots and the Purcell effect. Considering this progress, it is not unexpected that the strong coupling between a single quantum dot and a single cavity mode can be achieved soon in this system. Combined with the side excitation approach with which it is ideally compatible due to its bulk morphology, it could lead to the rapid development of a manufacturable technology.

The following appendix is meant to serve as a reference for future members of the group and perhaps also people in the field. Some of the material can be found in textbooks, but never simultaneously and usually not written out explicitly. The equations pertaining to resonance fluorescence theory in the general case that includes pure dephasing have been derived completely.

Appendices

Appendix A

Damping of a Two-Level System Coupled to a Reservoir

Although the damping constants appearing in the theoretical descriptions presented previously can be understood as phenomenological quantities, they can also be obtained from a more rigorous master equation approach.

This appendix gives a summary of how damping can be included in the optical Bloch and cavity-QED equations, by modeling the two-level system as interacting with a "reservoir". This approach recovers of course the phenomenologically assigned longitudinal and transverse decay times of NMR (T_1 and T_2) but is more insightful to understand the specific origins of the different types of dephasing, such as radiative losses or simply loss of phase coherence.

A.1 Master Equation: the "Quantum Jump" Picture

In the absence of decoherence, the equations governing the time evolution of the density matrix $\hat{\rho} = \hat{\rho}(t)$ are of course simply obtained (Schrödinger picture) as:

$$\frac{d}{dt}\hat{\rho} = -\frac{i}{\hbar}[\hat{H}, \hat{\rho}]$$

It can be shown that interactions with a reservoir can be included in a general way using quantum "jump" operators [103], which leads to:

$$\frac{d}{dt}\hat{\rho} = -\frac{i}{\hbar}[\hat{H}, \hat{\rho}] + \sum_k (\hat{L}_k \hat{\rho} \hat{L}_k^\dagger - \frac{1}{2}\hat{L}_k^\dagger \hat{L}_k \hat{\rho} - \frac{1}{2}\hat{\rho}\hat{L}_k^\dagger \hat{L}_k) \tag{A.1}$$

where the jump operators are denoted by: $\hat{L}_k = \sqrt{\Gamma_{ji}}\sigma_{ij} = \sqrt{\Gamma_{ji}}|i\rangle\langle j|$. Obviously a quantum jump from state $|i\rangle$ to state $|j\rangle$ occurs with "probability" Γ_{ij}. Equation A.1 is often called "Lindblad" equation. Note that the quantum jump operators act in the "system" and that the effect of the reservoir is contained in the sum over decay channels $k = \{ij\}$. For one single decay channel, we get:

$$\frac{d}{dt}\hat{\rho} = -\frac{i}{\hbar}[\hat{H}, \hat{\rho}] + \frac{\Gamma_{ji}}{2}(2\hat{\sigma}_{ij}\hat{\rho}\hat{\sigma}_{ji} - \hat{\sigma}_{jj}\hat{\rho} - \hat{\rho}\hat{\sigma}_{jj}) \tag{A.2}$$

which is also sometimes written in the form:

$$\frac{d}{dt}\hat{\rho} = -\frac{i}{\hbar}[\hat{H}_{eff}, \hat{\rho}] + \Gamma_{ji}\hat{\sigma}_{ji}\hat{\rho}\hat{\sigma}_{ij}$$

using the effective Hamiltonian:

$$\hat{H}_{eff} = \hat{H} - i\hbar\frac{\Gamma_{ji}}{2}\hat{\sigma}_{jj}$$

A.2 Optical Bloch Equations

For a two-state system, there can be only four different "quantum jumps" which either keep the state unchanged or flip the system between the upper and lower state. In general, the density matrix for the two-level system reads, as usual:

$$\hat{\rho} = \rho_{11}|1\rangle\langle 1| + \rho_{00}|0\rangle\langle 0| + \rho_{01}|0\rangle\langle 1| + \rho_{10}|1\rangle\langle 0|$$

and the Hamiltonian (rotating-wave approximation) is:

$$\hat{H} = \hbar\Delta\omega|1\rangle\langle 1| - \frac{\hbar\Omega}{2}(|0\rangle\langle 1| + |1\rangle\langle 0|)$$

so that the commutator evaluates to:

$$[\hat{H}, \hat{\rho}]/\hbar = -\frac{\Omega}{2}|0\rangle\langle 0|(\rho_{10} - \rho_{01}) + |1\rangle\langle 0|(\Delta\omega\rho_{10} - \Omega(\rho_{00} - \rho_{11})/2) +$$

$$+|0\rangle\langle 1|(-\Delta\omega\rho_{10} - \Omega(-\rho_{00} + \rho_{11})/2) - \frac{\Omega}{2}|1\rangle\langle 1|(-\rho_{10} + \rho_{01})$$

A.2.1 Radiative Decay

When a two-state system decays radiatively via spontaneous emission, it gives away one quantum of energy and its state jumps from $|1\rangle$ to $|0\rangle$ (see, for example [7]). So for this particular decoherence channel we must require $\Gamma_{10} = \Gamma$ ($i = 0$ and $j = 1$) to be the only non-zero element. The "Lindbladian" (second term in Eq. A.1) then reads:

$$L(\rho) = \Gamma(\rho_{11}|0\rangle\langle 0| + \rho_{11}|1\rangle\langle 1| - \frac{\rho_{01}}{2}|0\rangle\langle 1|) - \frac{\rho_{10}}{2}|1\rangle\langle 0|)$$

so that the optical Bloch equations are obtained as:

$$\dot{\rho_{11}} = \frac{i\Omega}{2}(\rho_{01} - \rho_{10}) - \Gamma\rho_{11}$$

$$\dot{\rho_{00}} = -\frac{i\Omega}{2}(\rho_{01} - \rho_{10}) + \Gamma\rho_{11}$$

$$\dot{\rho_{10}} = -i\Delta\omega\rho_{10} + \frac{i\Omega}{2}(\rho_{00} - \rho_{11}) - \frac{\Gamma}{2}\rho_{10}$$
$$\dot{\rho_{01}} = i\Delta\omega\rho_{01} - \frac{i\Omega}{2}(\rho_{00} - \rho_{11}) - \frac{\Gamma}{2}\rho_{01}$$

A.2.2 Pure Dephasing

Assuming a jump operator from the individual states to themselves, we obtain pure dephasing, i.e. loss of coherence without population relaxation. Starting from Eq. A.1 with two decay channels from state $|0\rangle$ to itself ($i = 0$, $j = 0$, and $\Gamma_{00} = \gamma$), and from state $|1\rangle$ to itself ($i = 1$, $j = 1$, and $\Gamma_{11} = \gamma$), we get the Lindbladian:

$$L(\rho) = -\frac{\gamma}{2}(\rho_{10}|1\rangle\langle 0| + \rho_{01}|0\rangle\langle 1|) - \frac{\gamma}{2}(\rho_{10}|1\rangle\langle 0| + \rho_{01}|0\rangle\langle 1|)$$

where the first and second term come from the first and second decay channel, respectively. They are actually equal. Combining radiative and pure dephasing, the Lindbladian reads:

$$L(\rho) = \Gamma(\rho_{11}|0\rangle\langle 0| + \rho_{11}|1\rangle\langle 1| - \frac{\rho_{01}}{2}|0\rangle\langle 1|) - \frac{\rho_{10}}{2}|1\rangle\langle 0|)$$

so that the optical Bloch equations are obtained as:

$$\dot{\rho_{11}} = \frac{i\Omega}{2}(\rho_{01} - \rho_{10}) - \Gamma\rho_{11}$$

$$\dot{\rho_{00}} = -\frac{i\Omega}{2}(\rho_{01} - \rho_{10}) + \Gamma\rho_{11}$$

$$\dot{\rho_{10}} = -i\Delta\omega\rho_{10} + \frac{i\Omega}{2}(\rho_{00} - \rho_{11}) - (\frac{\Gamma}{2} + \gamma)\rho_{10}$$
$$\dot{\rho_{01}} = i\Delta\omega\rho_{01} - \frac{i\Omega}{2}(\rho_{00} - \rho_{11}) - (\frac{\Gamma}{2} + \gamma)\rho_{01}$$

The real form used in Allen and Eberly [5] can, as usual, be obtained from the substitutions:

$$w = \rho_{11} - \rho_{00}$$

$$u = \rho_{01} + \rho_{10} = 2Re(\rho_{01})$$

$$v = i(\rho_{10} - \rho_{01}) = 2Im(\rho_{01})$$

which gives:

$$\dot{u} = -\Delta\omega \cdot v - (\Gamma/2 + \gamma)u$$

$$\dot{v} = \Omega w + \Delta\omega \cdot u - (\Gamma/2 + \gamma)v$$

$$\dot{w} = -\Omega v + \Delta\omega \cdot u - \Gamma(1 + w)$$

here $\Delta\omega = \omega_0 - \omega$ and Ω denote of course the detuning and the Rabi frequency, respectively. Obviously $1/T_2 = \gamma + \Gamma/2$ and $1/T_1 = \Gamma$.

Appendix B

Pulsed Excitation: Pulse Time/Frequency Profile, Area and Polarization

This appendix briefly summarizes the quantities need for describing Rabi oscillations and coherent control under pulsed excitation.

B.1 Relationship Between Average Intensity and Input Pulse Area

Our Ti:Sapphire laser provides pulses at a repetition rate f, and has an intensity profile of the form:

$$I(t) = \operatorname{sech}^2(1.76t/\tau_p)$$

where I_0 is the peak intensity and τ_p the pulse width. The factor of 1.76 corrects for the fact that τ_p is the full width at half maximum of the intensity profile, not the electric field profile. The relationship between the instantaneous electric field and intensity is given by:

$$I_0 = \frac{1}{2} n \epsilon_0 c E_0^2$$

Here n is the index of refraction, ϵ_0 the free-space permittivity and c the speed of light in vacuum. The quantity we actually measure with a powermeter is the average laser power P_{av} given by:

$$P_{av} = \frac{2\tau_p}{1.76} I_0 f A$$

where A is the area of the laser focus on the sample. Note that because of the integration properties of the sech function, i.e. $\int_{-\infty}^{\infty} \mathrm{sech}(x/a)dx = \pi a$ and $\int_{-\infty}^{\infty} \mathrm{sech}^2(x/a)dx = 2a$, these expressions take a very simple form. The relationship between the electric field and the average power is then:

$$E_0 = \sqrt{P_{av}}\sqrt{\frac{1.76}{n\epsilon_0 c\tau_p f A}} = \xi\sqrt{\frac{P_{av}}{\tau_p}}$$

where ξ is a constant that only depends on fixed parameters and fundamental constants. For our typical experiments (exciting from at glancing incidence) we have A=$\pi 10^2 \mu$m^2, $n = 3.6$ (GaAs), $f = 80.2$ Mhz. The input pulse area is then:

$$\theta(t) = \int_{-\infty}^{t} dt' \mu E(t') = \frac{d}{\hbar}\int_{-\infty}^{t} dt' E_0 \mathrm{sech}(\frac{1.76t'}{\tau_p})$$

and

$$\theta(\infty) = \frac{\pi}{1.76}\frac{d}{\hbar}\xi\sqrt{\tau_p}\sqrt{P_{av}}$$

Moreover, the instantaneous Rabi frequency (whose expression enters usually in numerical simulations) is:

$$\Omega(t) = \mu E(t) = \frac{d}{\hbar}E_0 \mathrm{sech}(\frac{1.76t}{\tau_p}) = \frac{d}{\hbar}\xi\sqrt{\frac{P_{av}}{\tau_p}}\mathrm{sech}(\frac{1.76t}{\tau_p}) = \Omega_0 \mathrm{sech}(\frac{1.76t}{\tau_p})$$

The relationship between $\theta(\infty)$ and Ω_0 is:

$$\Omega_0 = \frac{1.76}{\pi}\frac{\theta(\infty)}{\tau_p}$$

Note that the dipole moment d is sometimes defined differently, e.g. a factor of 2 is dropped. Dipole moments are often expressed in units of Debye (1 Debye = $3.335(10)^{-30}$ C·m).

Also note that P_{av} is the average power at the QD layer. Since one can position a powermeter only so close to the sample, a few other corrections are necessary. The most important correction arises due to the high reflectivity of GaAs. In fact, only a fraction of the incident light penetrates the sample. At normal incidence, this fraction is given by:

$$T = (\frac{2}{n+1})^2 = 0.19$$

More generally this fraction depends on the angle of incidence and the light polarization. As it turns out, using horizontally polarized light, incident at an angle of ∼ 60°, the correction factor is 0.063. Another minor correction is due to absorption by the cryostat window but we will ignore it here. This leads to an overall result:

$$\Omega_0 = \frac{d}{\hbar}\sqrt{\frac{P_av}{\tau_p}}\sqrt{\frac{1.76}{n\epsilon_0 cfA}} = 8.55(10)^{10} \cdot d(\text{Debye})\sqrt{\frac{P_{av}(mW)}{\tau_p(\text{ps})}}$$

or

$$\Omega_0 = 0.0855 \cdot d(\text{Debye})\sqrt{\frac{P_{av}(\text{mW})}{\tau_p(\text{ps})}}ps^{-1}$$

By measuring the intensity when $\theta(\infty) = \pi$, one can get a value for the transition dipole moment from:

$$d(\text{Debye}) = \frac{1.76}{0.0855}\frac{1}{\sqrt{\tau_p(\text{ps}) \cdot P_{av}^{(\pi)}(\text{mW})}}$$

B.2 Relationship Between the Spectral Width and the Temporal Width

The Autocorrelator (FR-103MN) provides the most reliable way to measure the duration of the laser pulses. The relationship between the time t read from the oscilloscope and the real time delay T is given by: $\frac{T}{t} = 6.25$ ps/ms. The pulse shape measured is an autocorrelation trace and needs to be deconvoluted. For a $sech^2(1.763t/\tau_p)$ pulse, the relationship between the autocorrelation width ΔT and the real FWHM τ_p is: $\frac{\tau_p}{\Delta T}= 0.648$. The temporal width can also be obtained from the spectral width. The latter is Fourier transform limited so that: $\tau_p \Delta\nu = 0.315$. At a wavelength $\lambda = 930$ nm, $\tau_p(ps) \cdot \Delta\lambda(nm) = 0.908$. The results from the autocorrelation measurement and the spectral measurement disagree slightly. Therefore, we chose the average value of both measurements. Table B.1 summarizes the results. Here $\Delta\lambda$ was measured with the spectrometer, and t was measured with the autocorrelator. Here the superscripts (s) and (a) refer to the width measured from the spectrometer and the width measured from the autocorrelator, respectively.

B.3 Polarization-Dependent Intensity Correction Factor

When the laser is incident at an angle on the GaAs surface, the intensity of the light penetrating in the sample is given by the Fresnel equations of reflection and refraction. Using the notation from Jackson, i is the angle of incidence and n' is the index of refraction of GaAs. E_0 is the electric field

$\Delta\lambda$ (nm)	t (ms)	T(ps)	$\tau_p^{(a)} = 0.648T$	$\tau_p^{(s)} 0.908/\Delta\lambda$	$(\tau_p^{(s)} + \tau_p^{(a)})/2$
0.12	2.72	16.992	11.011	7.57	9.29
0.13	2.43	15.17	9.83	6.98	8.41
0.14	2.17	13.58	8.80	6.49	7.64
0.15	1.95	12.19	7.90	6.05	6.98
0.16	1.76	11.02	7.14	5.68	6.41
0.17	1.61	10.06	6.52	5.34	5.93
0.18	1.49	9.32	6.04	5.04	5.54
0.19	1.44	9.00	5.70	4.78	5.24
0.20	1.41	8.796	5.48	4.84	5.01

Table B.1: Spectral and temporal widths of pulsed laser.

amplitude outside the sample and E_0' the electric field amplitude inside the sample. **E** perpendicular to the plane of incidence:

$$\frac{E_0'}{E_0} = \frac{2\cos(i)}{\cos(i) + \sqrt{n'^2 - \sin^2(i)}}$$

E parallel to the plane of incidence:

$$\frac{E_0'}{E_0} = \frac{2n'\cos(i)}{n'^2\cos(i) + \sqrt{n'^2 - \sin^2(i)}}$$

So the correction factor for the intensity becomes:

$$\chi = \left(\frac{\frac{2n'\cos(i)}{n'^2\cos(i)+\sqrt{n'^2-\sin^2(i)}}}{\frac{2\cos(i)}{\cos(i)+\sqrt{n'^2-\sin^2(i)}}} \right)^2 = \left(n' \frac{\cos(i) + \sqrt{n'^2 - \sin^2(i)}}{n'^2\cos(i) + \sqrt{n'^2 - \sin^2(i)}} \right)^2$$

Table B.2 lists a few angles of interest (we used $n' = 3.6$ for the index of GaAs around 1 micron wavelength.)

i (Degrees)	χ
45	1.44
55	1.80
65	2.46
68	2.77
74.5 (Brewsters angle)	3.76

Table B.2: Polarization correction factor.

Appendix C

Theory of Resonance Fluorescence

This appendix gives full account of the theory behind resonance fluorescence, as first derived by Mollow and extended here to include pure dephasing, i.e. loss of coherence without population decay. Starting from Ref. [108], pure dephasing is added to the optical Bloch equations for the two-level system. The power spectrum, average scattered intensity, and first and second order correlation functions are calculated. Here the situation is that of a two-state system with natural frequency ω_0, excited near-resonance by a monochromatic electric field $\mathcal{E} = \mathcal{E}_0 e^{-i\omega t}$ that may be slightly detuned by an amount $\Delta\omega = \omega - \omega_0$. Together with the dipole coupling λ this gives rise to a Rabi frequency $\Omega \equiv 2\lambda\mathcal{E}_0$.

In the rotating wave approximation, the equation of motion for the resonantly excited dipole reads:

$$\frac{d}{dt}\mathbf{R}(t) = \mathbf{M} \cdot \mathbf{R}(t) \tag{C.1}$$

where

$$\mathbf{M} = \begin{pmatrix} -\kappa & -i\Omega/2 & i\Omega/2 & 0 \\ -i\Omega/2 & -\kappa/2 - \gamma + i\Delta\omega & 0 & i\Omega/2 \\ i\Omega/2 & 0 & -\kappa/2 - \gamma - i\Delta\omega & -i\Omega/2 \\ \kappa & i\Omega/2 & -i\Omega/2 & 0 \end{pmatrix} \tag{C.2}$$

and

$$\mathbf{R}(t) = \begin{pmatrix} n(t) \\ \alpha(t) \\ \alpha^*(t) \\ m(t) \end{pmatrix}$$

Here $n(t) = Tr\{\rho(t)a^\dagger a\}$, $\alpha(t) = Tr\{\rho(t)a\}$, $\alpha^*(t) = Tr\{\rho(t)a^\dagger\}$, and $m(t) = Tr\{\rho(t)aa^\dagger\}$ $n(t)$ and $m(t)$ are the population of the two-level system in the ground and excited state, respectively, and $\alpha(t)$ denotes the coherence between the two states. The diagonal and off-diagonal damping terms, respectively $\frac{1}{T_1} = \kappa$ and $\frac{1}{T_2} = \gamma + \kappa/2$ have been included using the usual master equation (note that $\hbar = 1$ has been assumed). Equation C.1 has the steady state solutions:

$$\alpha_\infty = \frac{i\Omega}{4} \frac{\kappa + 2\gamma + 2i\Delta\omega}{\Delta\omega^2 + (\kappa + 2\gamma)(\kappa + 2\gamma + 2\Omega^2/\kappa)/4} \tag{C.3}$$

and

$$n_\infty = \frac{\Omega^2}{4\kappa} \frac{\kappa + 2\gamma}{\Delta\omega^2 + (\kappa + 2\gamma)(\kappa + 2\gamma + 2\Omega^2/\kappa)/4} \tag{C.4}$$

C.1 First order correlation function

C.1.1 Quantum Regression Theorem

The solution to Equation C.1, can be written as:

$$\mathbf{R}(t+\tau) = \mathbf{U} \cdot \mathbf{R}(t) \tag{C.5}$$

where

$$\mathbf{U} = \mathbf{U}(\tau) = e^{\mathbf{M}\tau} \tag{C.6}$$

According to the quantum regression theorem (see for example Ref. [108] p.1973, eq. 4.6),

$$g(\tau,t) \equiv \langle a^\dagger(t)a(t+\tau)\rangle = U_{\alpha\alpha}(\tau)n(t) + U_{\alpha m}(\tau)\alpha^*(t) \tag{C.7}$$

And for long enough times,

$$\boxed{g(\tau) = U_{\alpha\alpha}(\tau)n_\infty + U_{\alpha m}(\tau)\alpha^*_\infty \qquad \text{(C.8)}}$$

C.1.2 Calculation of $\mathbf{g(\tau)}$

We get g(τ) via equation C.8 by computing the necessary matrix exponentials of $\mathbf{M}$ in Eq. C.2. In the case of zero detuning, i.e. $\Delta\omega \equiv \omega - \omega_0 = 0$:

$$U_{\alpha\alpha}(\tau) = e^{\mathbf{M}\tau}|_{2,2}$$

$$= \frac{1}{2}e^{-\tau(\gamma+\kappa/2)} + e^{-\tau(\gamma/2+3\kappa/4)}\Big(\frac{1}{2}\cos(\mu\tau) - \frac{1}{8\mu}(2\gamma-\kappa)\sin(\mu\tau)\Big) \tag{C.9}$$

Here the frequency μ of the oscillations is given by:

$$\mu = \sqrt{\Omega^2 - (\kappa/4 - \gamma/2)^2} \tag{C.10}$$

Correspondingly,

$$U_{\alpha m}(\tau) = e^{\mathbf{M}\tau}|_{2,4}$$

$$= \frac{-i\Omega}{4\mu(2\Omega^2+\kappa^2+2\gamma\kappa)}\Bigg(4\kappa\mu e^{-\tau(\gamma/2+3\kappa/4)}\cos(\mu\tau) +$$

$$-(4\Omega^2+2\gamma\kappa-\kappa^2)e^{-\tau(\gamma/2+3\kappa/4)}\sin(\mu\tau) - 4\kappa\mu\Bigg) \tag{C.11}$$

So that

$$
\begin{aligned}
g(\tau) &= U_{\alpha\alpha}(\tau) n_\infty + U_{\alpha m}(\tau)\alpha^*_\infty \\
&= \frac{\Omega^2}{2\gamma\kappa+\kappa^2+2\Omega^2}\Bigg(\frac{\kappa^2}{2\gamma\kappa+\kappa^2+2\Omega^2}+\frac{1}{2}e^{-\tau(\gamma+\kappa/2)}+e^{-\tau(\gamma/2+3\kappa/4)}\Big(
\end{aligned}
$$

$$
\cos(\mu\tau)\frac{1}{2}\ \frac{2\Omega^2-\kappa^2+2\gamma\kappa}{2\Omega^2+\kappa^2+2\gamma\kappa}-\sin(\mu\tau)\frac{1}{4\mu}\ \frac{\Omega^2(2\gamma-5\kappa)+2\gamma^2\kappa-2\gamma\kappa^2+\kappa^3/2}{2\Omega^2+\kappa^2+2\gamma\kappa}\Big)\Bigg) \tag{C.12}
$$

C.1.3 Average Intensity

The average intensity is proportional to

$$
\begin{aligned}
\langle a^\dagger a\rangle &= g(0) \\
&= \frac{\Omega^2}{2\gamma\kappa+\kappa^2+2\Omega^2}\left(\frac{\kappa^2}{2\gamma\kappa+\kappa^2+2\Omega^2}+\frac{2\Omega^2+2\gamma\kappa}{2\gamma\kappa+\kappa^2+2\Omega^2}\right) \\
&= \frac{\Omega^2}{2\gamma\kappa+\kappa^2+2\Omega^2} = n_\infty(\Delta\omega\to 0)
\end{aligned}
\tag{C.13}
$$

C.1.4 Limiting Cases

If $\gamma = 0$, we get:

$$
\begin{aligned}
g(\tau) = \frac{\Omega^2}{\kappa^2+2\Omega^2}\Bigg(\frac{\kappa^2}{\kappa^2+2\Omega^2}+\frac{1}{2}e^{-\tau\kappa/2}+e^{-3\tau\kappa/4}\Big(\cos(\mu\tau)\frac{1}{2}\ \frac{2\Omega^2-\kappa^2}{2\Omega^2+\kappa^2}+ \\
-\sin(\mu\tau)\frac{1}{4\mu}\ \frac{-5\kappa\Omega^2+\kappa^3/2}{2\Omega^2+\kappa^2}\Big)\Bigg)
\end{aligned}
\tag{C.14}
$$

with now

$$
\mu = \sqrt{\Omega^2-\kappa^2/16} \tag{C.15}
$$

This is exactly the equation given by Scully [132] (pp.304, Eq. 10.5.20). In case the Rabi frequency is much smaller than the radiative damping, i.e. $\Omega \ll \kappa/4$, then $\mu \approx i\kappa/4$, and

$$g(\tau) \approx \frac{\Omega^2}{\kappa^2}\left(1 + \frac{1}{2}e^{-\kappa\tau/2} + e^{-3\kappa\tau/4}\Big(\cos(i\kappa\tau/4)\frac{-1}{2} + \frac{i}{2}\sin(i\kappa\tau/4)\Big)\right)$$

$$= \frac{\Omega^2}{\kappa^2}\left(1 + \frac{1}{2}e^{-\kappa\tau/2} - \frac{1}{2}e^{-\kappa\tau/2}\right) = \frac{\Omega^2}{\kappa^2} \tag{C.16}$$

This means that at low enough excitation intensity, the measured coherence should be that of the laser. This is very different from the case with finite dephasing ($\gamma \neq 0$). In this case, even though the Rabi frequency is small, there is still an inelastic contribution to $g(\tau)$. Explicitly, if $\gamma \neq 0$ and $\Omega \ll \kappa/4, \gamma/2$, then $\mu \approx i(\kappa/4 - \gamma/2)$ and Eq. C.12 becomes

$$g(\tau) \approx \frac{\Omega^2}{\kappa^2 + 2\gamma\kappa}\left(\frac{\kappa^2}{\kappa^2 + 2\gamma\kappa} + \frac{1}{2}e^{-\tau(\gamma+\kappa/2)} + \right.$$

$$+ e^{-\tau(\gamma/2+3\kappa/4)}\Big(\cosh((\kappa/4-\gamma/2)\tau)\frac{1}{2}\,\frac{-\kappa^2 + 2\gamma\kappa}{\kappa^2 + 2\gamma\kappa} +$$

$$\left. - \sinh((\kappa/4-\gamma/2)\tau)\frac{\kappa(\kappa-2\gamma)(\kappa/2-\gamma)}{(\kappa-2\gamma)(\kappa^2+2\gamma\kappa)}\Big)\right) \tag{C.17}$$

This reduces to:

$$g(\tau) = \frac{\Omega^2}{\kappa^2 + 2\gamma\kappa}\left(\frac{\kappa}{2\gamma+\kappa} + e^{-\tau(\gamma+\kappa/2)}\Big(\frac{2\gamma}{2\gamma+\kappa}\Big)\right) \tag{C.18}$$

Therefore, any dephasing that is comparable to the radiative decay completely washes out the effect described in textbooks, i.e. that at low intensity we should expect to measure the coherence of the laser. In fact, in our case we know that $\gamma \gg \kappa$ so that Eq. C.18 simplifies further to:

$$g(\tau) \approx \frac{\Omega^2}{2\gamma\kappa} e^{-\gamma\tau} \tag{C.19}$$

So when we measure the fringe contrast at low intensity for a single quantum dot's ground state, we should expect a decay equal to the half width at half maximum of the corresponding "absorption" spectrum that we measure by plotting the total average intensity as a function of detuning. This is given by Eq. C.4, again in the limit $\gamma \gg \kappa$ and $\Omega \ll \gamma$ by:

$$n_\infty \approx \frac{\Omega^2}{2\kappa} \, \frac{\gamma}{\Delta\omega^2 + \gamma^2} \tag{C.20}$$

Eq. C.20 describes a Lorentzian of FWHM equal to 2γ. In general, we must fit our fringe contrast with Eq. C.12 still in the limit $\gamma \gg \kappa$. This yields:

$$g(\tau) \approx \frac{1}{4} \, \frac{\Omega^2}{\Omega^2 + \kappa\gamma} \left(\frac{\kappa^2}{\Omega^2 + \kappa\gamma} + e^{-\gamma\tau} + e^{-\gamma\tau/2} \Big(\cos(\mu\tau) - \frac{\gamma}{2\mu} \sin(\mu\tau) \Big) \right) \tag{C.21}$$

$$\boxed{g(\tau) \approx \frac{1}{4} \, \frac{\Omega^2}{\Omega^2 + \kappa\gamma} \left(e^{-\gamma\tau} + e^{-\gamma\tau/2} \Big(\cos(\mu\tau) - \frac{\gamma}{2\mu} \sin(\mu\tau) \Big) \right) \quad \text{(C.22)}}$$

where $\mu \approx \sqrt{\Omega^2 - \gamma^2/4}$

C.1.5 Power Spectrum

The power spectrum $S(\nu)$ of the resonance fluorescence is given by the Fourier transform of the first order correlation function, i.e.:

$$S(\nu) = \frac{1}{\pi} Re \int_0^\infty g(\tau) e^{i\nu\tau} d\tau \tag{C.23}$$

To compute the power spectrum, we use the following three equalities:

$$\int_0^\infty d\tau e^{-i(\omega-\nu)\tau} = \pi\delta(\nu-\omega) \tag{C.24}$$

$$\int_0^\infty d\tau e^{-i(\omega-\nu)\tau-\gamma\tau} = \frac{1}{i(\omega-\nu)+\gamma} \tag{C.25}$$

$$\int_0^\infty d\tau e^{-i(\omega-\nu)\tau-\gamma\tau/2\mp i\mu\tau} = \frac{1}{i(\omega-\nu\pm\mu)+\gamma/2} \tag{C.26}$$

Starting from Eq. C.21, which assumed $\gamma \gg \kappa$, we get:

$$\begin{aligned} S(\delta) = \frac{1}{8\pi}\,\frac{\gamma\Omega^2}{\Omega^2+\kappa\gamma}\Bigg(&\frac{1}{\delta^2+\gamma^2}+\frac{1/2}{(\delta-\mu)^2+(\gamma/2)^2}+\frac{1/2}{(\delta+\mu)^2+(\gamma/2)^2}+ \\ &-\frac{1}{2\mu}\,\frac{\delta-\mu}{(\delta-\mu)^2+(\gamma/2)^2}+\frac{1}{2\mu}\,\frac{\delta+\mu}{(\delta+\mu)^2+(\gamma/2)^2}\Bigg) \end{aligned} \tag{C.27}$$

Here the abbreviation $\delta = \omega - \nu$ has been used. Note that the harmonic variation of $g(\tau)$, $e^{-i\omega\tau}$ which has previously not been carried, has been re-introduced here. Simplified, this gives:

$$\boxed{S(\delta) = \frac{1}{8\pi}\,\frac{\gamma\Omega^2}{\Omega^2+\kappa\gamma}\left(\frac{1}{\delta^2+\gamma^2}+\frac{1-\delta/(2\mu)}{(\delta-\mu)^2+(\gamma/2)^2}+\frac{1+\delta/(2\mu)}{(\delta+\mu)^2+(\gamma/2)^2}\right) \quad (C.28)}$$

This describes the Mollow triplet with a central peak of width 2γ, and two side peaks of width γ, which are displaced by an amount $\mu \approx \sqrt{\Omega^2-\gamma^2/4}$.

C.1.6 Power Spectrum - general case

In the general case of arbitrary dephasing, we use again

$$S(\nu) = \frac{1}{\pi} Re \int_0^\infty g(\tau) e^{i\nu\tau} d\tau$$

with

$$\begin{aligned} g(\tau) = \frac{\Omega^2}{2\gamma\kappa+\kappa^2+2\Omega^2}\Bigg(& \frac{\kappa^2}{2\gamma\kappa+\kappa^2+2\Omega^2}+\frac{1}{2}e^{-\tau(\gamma+\kappa/2)}+ \\ & e^{-\tau(\gamma/2+3\kappa/4)}\Big(\cos(\mu\tau)\frac{1}{2}\;\frac{2\Omega^2-\kappa^2+2\gamma\kappa}{2\Omega^2+\kappa^2+2\gamma\kappa}+ \\ & -\sin(\mu\tau)\frac{1}{4\mu}\;\frac{\Omega^2(2\gamma-5\kappa)+2\gamma^2\kappa-2\gamma\kappa^2+\kappa^3/2}{2\Omega^2+\kappa^2+2\gamma\kappa}\Big)\Bigg) \end{aligned} \tag{C.29}$$

to get:

$$\begin{aligned} S(\nu) = \frac{n_\infty(0)}{\pi}Re\Bigg\{ & n_\infty(0)\frac{\kappa^2}{\Omega^2}\delta(\nu-\omega)+\frac{1}{2}\frac{1}{i(\omega-\nu)+1/T_2}+ \\ & +\frac{n_\infty(0)}{\Omega^2}\Big(\frac{A}{2}+\frac{B}{4\mu}\frac{1}{2i}\Big)\frac{1}{i(\omega-\nu-\mu)+(\frac{1}{2T_1}+\frac{1}{2T_2})} \\ & +\frac{n_\infty(0)}{\Omega^2}\Big(\frac{A}{2}-\frac{B}{4\mu}\frac{1}{2i}\Big)\frac{1}{i(\omega-\nu+\mu)+(\frac{1}{2T_1}+\frac{1}{2T_2})}\Bigg\} \end{aligned}$$

so that:

$$\begin{aligned} S(\nu) = \frac{n_\infty(0)}{\pi}\Bigg\{ & n_\infty(0)\frac{\kappa^2}{\Omega^2}\delta(\nu-\omega)+\frac{1}{2}\frac{1/T_2}{(\omega-\nu)^2+1/T_2^2}+ \\ & +\frac{n_\infty(0)}{\Omega^2}\Big(\frac{A}{2}+\frac{B}{4\mu}\frac{1}{2i}\Big)\frac{1}{i(\omega-\nu-\mu)+(\frac{1}{2T_1}+\frac{1}{2T_2})}+ \\ & +\frac{n_\infty(0)}{\Omega^2}\Big(\frac{A}{2}-\frac{B}{4\mu}\frac{1}{2i}\Big)\frac{1}{i(\omega-\nu+\mu)+(\frac{1}{2T_1}+\frac{1}{2T_2})}\Bigg\} \end{aligned}$$

or,

$$\begin{aligned} S(\nu) = \frac{n_\infty(0)}{\pi}\Bigg\{ & \frac{1}{2}\frac{1/T_2}{(\omega-\nu)^2+1/{T_2}^2}+ \\ & +\frac{n_\infty(0)}{\Omega^2}\Bigg(\frac{\frac{A}{2}(\frac{1}{2T_1}+\frac{1}{2T_2})-B\frac{\omega-\nu-\mu}{8\mu}}{(\omega-\nu-\mu)^2+(\frac{1}{2T_1}+\frac{1}{2T_2})^2}+\frac{\frac{A}{2}(\frac{1}{2T_1}+\frac{1}{2T_2})+B\frac{\omega-\nu+\mu}{8\mu}}{(\omega-\nu+\mu)^2+(\frac{1}{2T_1}+\frac{1}{2T_2})^2}\Bigg)\Bigg\} \end{aligned}$$

Here the short hand used is:

$$A = \frac{1}{2}(2\Omega^2 - \kappa^2 + 2\gamma\kappa) = \Omega^2 + \frac{1}{T_1}(\frac{1}{T_2} - \frac{1}{T_1})$$

and

$$\begin{aligned} B &= -(\Omega^2(2\gamma - 5\kappa) + 2\gamma^2\kappa - 2\gamma\kappa^2 + \kappa^3/2) \\ &= 2\Omega^2(\frac{3}{T_1} - \frac{1}{T_2}) - \frac{2}{T_1}(\frac{1}{T_1} - \frac{1}{T_2})^2 \end{aligned}$$

Therefore, in the general case, the central peak has a width (FWHM) of $2/T_2$ and the side peaks have a width (FWHM) of $(1/T_1 + 1/T_2)/2$, the average of the transverse and longitudinal decay rates. Note that the delta function term has been left out. This term, which represented a constant contrast in the time domain, will not be visible, at least not at the resolution of our system. To observe this term, scanning the interferometer for tens of nanoseconds (say a meter distance) would be required. Finally, in the limit of no pure dephasing, i.e. $\gamma = 0$ or $T_2 = 2T_1$, we get,

$$\begin{aligned} S(\nu) = \frac{n_\infty(0)}{\pi}\left\{ \frac{1}{4T_1}\frac{1}{(\omega-\nu)^2 + (\frac{1}{T_1})^2} + \right. \\ \left. + \frac{n_\infty(0)}{\Omega^2}\left(\frac{1}{T_1}\frac{\Omega^2 - \frac{1}{4T_1^2} - \frac{\omega-\nu}{4\mu}(5\Omega^2 - \frac{1}{4T_1^2})}{(\omega-\nu-\mu)^2 + (\frac{3}{4T_1})^2} + \text{''}\mu \to -\mu\text{''} \right) \right\} \end{aligned}$$

C.1.7 Power Broadening

The power-broadened linewidth is also directly measured in the experiment, i.e. it is obtained from the total emitted (average) intensity as a function of detuning. It is also often written out explicitly in the general case (both radiative and non-radiative damping), for example in Allen and Eberly [5] (p. 140, eq. 6.23):

$$HWHM = \frac{1}{T_2}\sqrt{1 + T_1 T_2 \Omega^2} \tag{C.30}$$

We get, using Eq. C.4, that

$$n_\infty(\Delta\omega) = \frac{\Omega^2}{4\kappa}\ \frac{\kappa + 2\gamma}{\Delta\omega^2 + (\kappa + 2\gamma)(\kappa + 2\gamma + 2\Omega^2/\kappa)/4} \tag{C.31}$$

and with $\frac{1}{T_1} = \kappa$ and $\frac{1}{T_2} = \gamma + \kappa/2$ we get:

$$n_\infty(\Delta\omega) = \frac{1}{2}\ \frac{T_1 \Omega^2 / T_2}{\Delta\omega^2 + {T_2}^{-2} + \Omega^2 T_1/T_2} \tag{C.32}$$

which is a Lorentzian with a HWHM equal to $\frac{1}{T_2}\sqrt{1 + T_1 T_2 \Omega^2}$.

C.1.8 Notes on Optical Bloch Equations

The familiar (real) optical Bloch eqations are derived from Eqs. C.1 and C.2 using the following substitutions:

$$\alpha = \frac{u - iv}{2} \qquad \alpha^* = \frac{u + iv}{2} \qquad w = n - m$$

Then we get:

$$\dot{u} = v\Delta\omega - \frac{u}{T_2} \tag{C.33}$$

$$\dot{v} = \Omega w - u\Delta\omega - \frac{v}{T_2} \tag{C.34}$$

$$\dot{w} = -\Omega v - \frac{w + 1}{T_1} \tag{C.35}$$

Note that Allen and Eberly [5] use a slightly different notation, namely their detuning is of opposite sign $\Delta = \omega_0 - \omega = -\Delta\omega$. Also, in their notation, κ

denotes the dipole moment (actually a factor of 2 different from our λ) so that they write (c.f. pp. 60):

$$\begin{aligned}\dot{u} &= -\Delta v - \frac{u}{T_2} && \text{(C.36)}\\ \dot{v} &= \kappa\mathcal{E}w + \Delta u - \frac{v}{T_2} && \text{(C.37)}\\ \dot{w} &= -\kappa\mathcal{E}v - \frac{w+1}{T_1} && \text{(C.38)}\end{aligned}$$

C.2 Second order correlation function

The second order correlation function $g^{(2)}(\tau)$ is calculated in the same manner as $g(\tau)$, using the quantum regression theorem. Explicitly, it is given by:

$$g^{(2)}(\tau) = \langle a^\dagger(t)a^\dagger(t+\tau)a(t+\tau)a(t)\rangle$$

C.2.1 Quantum regression theorem

The quantum regression theorem states [132] that for an operator $\mathcal{O}$ whose expectation value is known to evolve from a time t to a time $t+\tau$ as:

$$\langle\mathcal{O}(t+\tau)\rangle = \sum_j a_j(\tau)\langle\mathcal{O}_j(t)\rangle$$

the two-time correlation function $\langle\mathcal{O}_i(t)\mathcal{O}(t+\tau)\mathcal{O}_k(t)\rangle$ can be calculated as a function of single time expectation values as follows:

$$\langle\mathcal{O}_i(t)\mathcal{O}(t+\tau)\mathcal{O}_k(t)\rangle = \sum_j a_j(\tau)\langle\mathcal{O}_i(t)\mathcal{O}_j(t)\mathcal{O}_k(t)\rangle$$

C.2.2 Calculation of $g^{(2)}(\tau)$

From the optical Bloch equations, whose time evolution was previously written as:

$$\mathbf{R}(t+\tau) = \mathbf{U} \cdot \mathbf{R}(t) \tag{C.39}$$

with

$$\mathbf{U} = \mathbf{U}(\tau) = e^{\mathbf{M}\tau} \tag{C.40}$$

We can get $g^{(2)}(\tau)$, using the quantum regression theorem, as a function of $\mathbf{U}$ and then take the limit of infinitely long time t. Note that:

$$\mathbf{R}(t) = \begin{pmatrix} n(t) \\ \alpha(t) \\ \alpha^*(t) \\ m(t) \end{pmatrix}$$

or, explicitly,

$$\begin{gathered} n(t) = \langle a^\dagger(t) a(t) \rangle \\ \alpha(t) = \langle a(t) \rangle \\ \alpha^*(t) = \langle a^\dagger(t) \rangle \\ m(t) = \langle a(t) a^\dagger(t) \rangle \end{gathered}$$

and that:

$$\begin{gathered} a^\dagger a = |1\rangle\langle 1| \\ a = |0\rangle\langle 1| \\ a^\dagger = |1\rangle\langle 0| \\ a a^\dagger = |0\rangle\langle 0| \end{gathered}$$

Therefore:

$$g^{(2)}(\tau) = \langle a^\dagger(t) a^\dagger(t+\tau) a(t+\tau) a(t) \rangle$$

$$\begin{gathered} g^{(2)}(\tau) = U_{n,n}(\tau)\langle a^\dagger(t) a^\dagger(t) a(t) a(t) \rangle + U_{n,\alpha}(\tau)\langle a^\dagger(t) a(t) a(t) \rangle \\ + U_{n,\alpha^*}(\tau)\langle a^\dagger(t) a^\dagger(t) a(t) \rangle + U_{n,m}(\tau)\langle a^\dagger(t) a(t) a^\dagger(t) a(t) \rangle \end{gathered} \tag{C.41}$$

Only the last term is non-zero, so that:

$$g^{(2)}(\tau) = U_{n,m}(\tau)\langle a^\dagger(t)a(t)\rangle$$

And in the limit $t \to \infty$,

$$g^{(2)}(\tau) = U_{n,m}(\tau)n_\infty \tag{C.42}$$

which evaluates (normalized, and at exact resonance) to:

$$\boxed{g^{(2)}(\tau) = 1 - e^{-(\gamma/2+3\kappa/4)\tau}\Big(\cos(\mu\tau) + \frac{2\gamma+3\kappa}{4\mu}\sin(\mu\tau)\Big) \qquad \text{(C.43)}}$$

where

$$\mu = \sqrt{\Omega^2 - (\kappa/4 - \gamma/2)^2} \tag{C.44}$$

C.2.3 Limiting cases

Scully [132] gives the exact solution in the case $\gamma = 0$:

$$g^{(2)}(\tau) = 1 - e^{-3\kappa\tau/4}\Big(\cos(\mu\tau) + \frac{3\kappa}{4\mu}\sin(\mu\tau)\Big)$$

which is exactly what we find from Eq. (C.43). Meystre and Sargent ([103]) also give a formula for the case of strong excitation but including pure dephasing:

$$g^{(2)}(\tau) = 1 - e^{-(\gamma/2+3\kappa/4)}\cos(\Omega\tau)$$

which is also what we get from Eq. (C.43), when the sine term vanishes. Note that in their notation (which has been converted here), $\gamma = 1/T_2$ and $\Gamma = 1/T_1$.

C.2.4 Other limiting cases of interest

Of particular interest are the limiting cases under weak excitation. In general, if $\Omega \ll |\gamma/2 - \kappa/4|$, the $\mu \approx i|\gamma/2 - \kappa/4|$ and:

$$\boxed{g^{(2)}(\tau) = 1 - \frac{2\gamma + \kappa}{2\gamma - \kappa} e^{-\kappa\tau} + \frac{2\kappa}{2\gamma - \kappa} e^{-(\gamma + \kappa/2)\tau}} \tag{C.45}$$

then, if $\gamma \ll \kappa/2$, we get:

$$\boxed{g^{(2)}(\tau) = 1 + e^{-\kappa\tau} - 2e^{-\kappa\tau/2}} \tag{C.46}$$

and if $\gamma \gg \kappa/2$, we get:

$$\boxed{g^{(2)}(\tau) = 1 - e^{-\kappa\tau}} \tag{C.47}$$

The latter result is particularly interesting, because this is what everybody uses to fit their anti-bunching data. Depending on which limiting condition applies, the extracted lifetime can be off by a factor of 3 or more.

Appendix D

Cavity QED - some Theory

Here are the basic derivations (which can also be found in textbooks) of the results used for describing basic cavity-QED effects.

D.1 Perturbative Calculation of the Purcell Effect

One way to calculate the Purcell factor is to use the Fermi golden rule, which reads:

$$\frac{1}{\tau} = \frac{2\pi}{\hbar^2}\rho(\omega_e)\overline{|\langle \hat{H}_{in}\rangle|^2}$$

where the bar denotes averaging over all modes. All we need to do is compare the rates computed in free space and the rates in the cavity. The density of modes, $\rho(\omega)$, is different in both cases, but the vacuum field also changes. Specifically, the emission rate is changed in three ways:

1) The density of states is constant in free space (or in an infinite dielectric). It is sharply peaked around the resonance frequency of a single mode in a cavity. This highlights the importance of a high Q.

2) The vacuum field is changed in inverse proportion to the square root of the mode volume of the cavity. In free-space the volume factor cancels out, its just a normalization factor.

3) In free-space, the vacuum field is randomly polarized whereas in the cavity each mode has, in general, a well-defined polarization. The dipole moment of the quantum dot also has one of two polarizations in the plane orthogonal to the growth direction (quantum dots resemble pancakes). Therefore, the vector dot product between the field polarization vector and the optical dipole moment also determines the strength of the Purcell enhancement.

Below, the respective density of modes are first calculated before the Fermi golden rule is evaluated.

D.1.1 Free Space Density of Modes

The density of modes of the electromagnetic field in free space, i.e., the number of available modes in the energy interval $[\omega, \omega + d\omega]$ is given by:

$$dN = \rho(\omega) d\omega$$

If a normalization volume, V', is assumed (cubical box), then each mode in k-space occupies a (k-space) volume equal to $(2\pi)^3/V'$. In a spherical shell of radius k and thickness dk, there are thus $dN = 2 \times \frac{V'}{(2\pi)^3} \times 4\pi k^2 dk$ available modes (one for each polarization). Substituting for $k = n \times \omega/c$, where n is the index of refraction of the dielectric, we get:

$$dN = 2 \times \frac{V'}{(2\pi)^3} \times 4\pi\omega^2 n^3 d\omega/c^3 = \frac{\omega^2 V' n^3}{\pi^2 c^3} d\omega$$

This is the free space density of modes,

$$\rho_{free}(\omega) = \frac{\omega^2 V' n^3}{\pi^2 c^3}$$

D.1.2 Density of Modes in a Cavity

An emitter in a cavity near resonance with a single mode of that cavity (only one polarization) will see a mode density given approximately by a normalized ($\int \rho_{cav}(\omega)d\omega = 1$) Lorentzian:

$$\rho_{cav}(\omega) = \frac{2}{\pi \Delta\omega_c} \times \frac{\Delta\omega_c^2}{4(\omega - \omega_c)^2 + \Delta\omega_c^2}$$

This mode, centered at $\omega = \omega_c$, is assumed to have a quality factor $Q = \omega_c/\Delta\omega_c$.

D.1.3 Evaluation of the Decay Rates

We need to compute the matrix elements in the Fermi golden rule evaluation. In general, the single mode quantized field is expressed as:

$$\vec{E}(\vec{r}, t) = i\vec{\epsilon}\sqrt{\frac{\hbar\omega}{2\epsilon_0 n^2 V}} \times f(\vec{r}) \times \hat{a}e^{-i\omega t} + h.c.$$

where $h.c.$ stands for hermitian conjugate. $\vec{\epsilon}$ is a unit vector along the direction of polarization of the field whose mode function is $f(\vec{r})$, and V is either a normalization volume (free space) or the mode volume, $V = \frac{1}{n^2}\int\int\int n(\vec{r})|\vec{f}(\vec{r})|^2$. This expression describes a single electromagnetic mode with a specific wavevector, $\vec{k}$, and polarization λ. However, the modal indices have been omitted for clarity. The spontaneous emission from the upper state, $|b\rangle$, to the lower state, $|a\rangle$, is quantitatively described by the following matrix element in the Fermi golden rule:

$$\langle a, 1|\hat{H}_{int}|b, 0\rangle = \langle a| \otimes \langle 1| - e \cdot \vec{E}(\vec{r}_e) \cdot \vec{r}|b\rangle \otimes |0\rangle$$

The photon number states, $|0\rangle$, and $|1\rangle$, denote the states with respectively zero and one photon in the mode. This gives:

$$\langle a,1|\hat{H}_{int}|b,0\rangle = e \times i(\vec{\epsilon})^* \sqrt{\frac{\hbar\omega}{2\epsilon_0 n^2 V}} f^*(\vec{r}_e) \times \langle a|\vec{r}|b\rangle\langle 1|\hat{a}^\dagger|0\rangle$$

We have used the second term in the above expression for $\vec{E}(\vec{r},t)$ because only $\hat{a}^\dagger$ can connect $|0\rangle$ and $|1\rangle$, i.e. $\langle n+1|\hat{a}^\dagger|n\rangle = \sqrt{n+1}$. Note that while $\vec{r}$ denotes the position operator, $f(\vec{r}_e)$ is simply a function (which satisfies Maxwells equations) evaluated at the position, $\vec{r}_e$, of the emitter. Finally we get:

$$|\langle a,1|\hat{H}_{int}|b,0\rangle|^2 = \frac{e^2\hbar\omega}{2\epsilon_0 n^2 V} \times |(\vec{\epsilon})^* f^*(\vec{r}_e) \times \langle a|\vec{r}|b\rangle|^2$$

Usually this is written using $\langle a|\vec{r}|b\rangle \equiv \vec{r}_{ab}$ and $\vec{\mu}_{ab} \equiv -e \cdot \vec{r}_{ab}$ is the dipole moment of the particular transition. Therefore,

$$|\langle a,1|\hat{H}_{int}|b,0\rangle|^2 = \frac{\hbar\omega}{2\epsilon_0 n^2 V} \times |\vec{\epsilon} f(\vec{r}_e) \cdot \vec{\mu}_{ab}|^2$$

D.1.3.1 Free space

The mode function is then given by $f(\vec{r}) = e^{i\vec{k}\vec{r}}$ so that

$$|\langle a,1|\hat{H}_{int}|b,0\rangle|^2 = \frac{\hbar\omega}{2\epsilon_0 n^2 V} \times |\vec{\epsilon} \cdot \vec{\mu}_{ab}|^2$$

Since the density of states is $\rho_{free}(\omega) = \frac{\omega^2 V n^3}{\pi^2 c^3}$, the Fermi golden rule evaluates to:

$$\frac{1}{\tau_{free}} = \frac{2\pi}{\hbar^2}\rho_{free}(\omega) \times |\langle a,1|\hat{H}_{int}|b,0\rangle|^2 = \frac{\omega^3}{\pi\hbar c^3 \epsilon_0}|\vec{\epsilon} \cdot \vec{\mu}_{ab}|^2$$

and, when averaged over the random dipole orientations (factor of 1/3), to

$$\frac{1}{\tau_{free}} = \frac{\omega^3 n |\vec{\mu}_{ab}|^2}{3\pi\epsilon_0\hbar c^3}$$

which is the familiar result for the radiative decay rate.

D.1.3.2 Emitter in a Cavity

We then retain the general form:

$$|\langle a,1|\hat{H}_{int}|b,0\rangle|^2 = \frac{\hbar\omega}{2\epsilon_0 n^2 V} \times |f(\vec{r}_e)\vec{\epsilon}\cdot\vec{\mu}_{ab}|^2$$

and use:

$$\rho_{cav}(\omega) = \frac{2}{\pi\Delta\omega_c} \times \frac{\Delta\omega_c^2}{4(\omega-\omega_c)^2+\Delta\omega_c^2}$$

we get:

$$\frac{1}{\tau_{cav}} = \frac{2\pi}{\hbar^2}\rho_{cav}(\omega)|\langle a,1|\hat{H}_{int}|b,0\rangle|^2 = \frac{\hbar\omega}{2\epsilon_0 n^2 V} \times |f(\vec{r}_e)\vec{\epsilon}\cdot\vec{\mu}_{ab}|^2$$

$$= \frac{2}{\epsilon_0 n^2\hbar} \times (Q/V) \times \frac{\Delta\omega_c^2}{4(\omega-\omega_c)^2+\Delta\omega_c^2} \times |f(\vec{r}_e)\vec{\epsilon}\cdot\vec{\mu}_{ab}|^2$$

Finally,

$$\frac{\tau_{free}}{\tau_{cav}} = \frac{2}{\epsilon_0 n^2\hbar} \times (Q/V) \times \frac{\Delta\omega_c^2}{4(\omega-\omega_c)^2+\Delta\omega_c^2} \times |f(\vec{r}_e)\vec{\epsilon}\cdot\vec{\mu}_{ab}|^2 \frac{3\pi\epsilon_0\hbar c^3}{|\vec{\mu}_{ab}|^2\omega^3 n}$$

and substituting for $\lambda = \frac{2\pi c}{\omega}$,

$$\frac{\tau_{free}}{\tau_{cav}} = F_p \times \frac{\Delta\omega_c^2}{4(\omega-\omega_c)^2+\Delta\omega_c^2} \times |f(\vec{r}_e)\vec{\epsilon}\cdot\vec{\mu}_{ab}|^2/|\vec{\mu}_{ab}|^2$$

where $F_p = \frac{3Q}{4\pi^2 V}(\lambda/n)^3$ is the Purcell factor (here is the free space wavelength, not the index labeling the polarization state as before). This factor becomes important as the size of the cavity approaches the wavelength in the dielectric. Note that this is only valid if $\Delta\omega_e \ll \Delta\omega_c$. If this is not the case, Q needs to be replaced by $(1/Q + \Delta\omega_e/\omega)^{-1}$, i.e. the Purcell effect saturates as the emitter linewidth approaches the linewidth of the cavity.

This still remains a very simplified picture, because only one mode has been considered. In a real situation, there is a competition between confined modes of the cavity and other modes that may be supported in the structure such as waveguide modes in layered systems. Thus, the dependence of the lifetime enhancement on the mode volume, in particular, is not really linear. Typically, the mode volume needs to be smaller than a certain value before any Purcell effect is observable, regardless of how large Q is. The theoretical expression can be corrected for, by simply adding a term, α, accounting for decay into leaky modes:

$$\frac{\tau_{free}}{\tau_{cav}} = F_p \times \frac{\Delta\omega_c^2}{4(\omega-\omega_c)^2 + \Delta\omega_c^2} \times |f(\vec{r}_e)\vec{\epsilon} \cdot \vec{\mu}_{ab}|^2/|\vec{\mu}_{ab}|^2 + \alpha$$

The data is then traditionally represented as the lifetime enhancement $\frac{\tau_{free}}{\tau_{cav}}$ versus Purcell factor, F_p.

Appendix E

All-Epitaxial Microcavities: A Gaussian Beam Analysis

This appendix is dedicated to the theoretical modeling of the all-optical microcavities presented above, particularly their resonant frequencies. This can be done by assuming that they can be approximated by truncated fibers which can be then described with the usual effective index formalism that yields Bessel function solutions. Alternatively, the cavities can be viewed as consisting of one planar and one spherical mirror, thus resembling a conventional cavity, albeit smaller, which can be understood with Gaussian beam optics. The latter approach is taken here, as it gives simple analytical formulas for the resonant frequencies as a function of otherwise measurable parameters, such as the radius of curvature of the upper mirror which can be obtained from AFM measurements.

E.1 Hermite-Gaussian Solutions

The familiar solution to the paraxial wave equation in cartesian coordinates is written as:

$$E_{nm}(x, y, z) = u_n(x, z)u_m(y, z)$$

with

$$u_n(x,z) = \Big(\frac{2}{\pi}\Big)^{1/4}\sqrt{\frac{e^{i(2n+1)(\psi(z)-\psi_0)}}{2^n n! w(z)}} H_n\Big(\frac{x\sqrt{2}}{w(z)}\Big)\exp(-i\frac{kx^2}{2R(z)} - \frac{x^2}{w(z)^2}) \quad \text{(E.1)}$$

Here $w(z) = w_0\sqrt{1+(z/z_R)^2}$ is the waist size as a function of z, $R(z) = z + z_R^2/z$ is the radius of curvature of the wave fronts as a function of z, and $\psi(z) = \tan^{-1}(z/z_R)$ is the Guoy phase shift.

A Gaussian beam is entirely characterized by its Rayleigh range, z_R, which determines the scaling of the field with z (given the wave-vector, k, and $w_0^2 = 2z_R/k$.) In a resonator, it is the geometry, i.e. the radii of curvature of the mirrors that fix the Rayleigh range. This is because the wave front curvature at the mirror positions must match the curvature of the mirrors.

The functions $u_n(x,z)$ are generally called "Hermite-Gaussian functions". They are orthonormal, i.e

$$\int_{-\infty}^{\infty} u_n^*(x,z)u_m(x,z)dx = \delta_{nm}$$

Therefore, any paraxial beam $E(x,y,z)$ can be constructed from a superposition of the functions $E_{nm}(x,y,z) = u_n(x,z)u_m(y,z)$, as:

$$E(x,y,z) = \sum_{n=0}^{\infty}\sum_{m=0}^{\infty} c_{nm}E_{nm}(x,y,z)$$

with the expansion coefficients c_{nm} given by

$$c_{nm} = \int_{-\infty}^{\infty}\int_{-\infty}^{\infty} E_{nm}(x,y,z)E_{nm}^*(x,y,z)dxdy$$

E.2 Laguerre-Gaussian Solutions

When the paraxial wave equation is solved in cylindrical coordinates, the solutions are "Laguerre-Gaussian" function,

$$E_{pl}(r,\theta,z) = \sqrt{\frac{2p!}{(1+\delta_{ol})\pi(l+p)!}} \frac{e^{i(2p+l+1)(\psi(z)-\psi_0)}}{w(z)} \Big(\frac{r\sqrt{2}}{w(z)}\Big)^l$$

$$\times L_p^l\Big(\frac{2r^2}{w(z)^2}\Big) \exp(-i\frac{kr^2}{2R(z)} - \frac{r^2}{w(z)^2})e^{il\theta} \qquad \text{(E.2)}$$

where $w(z)$, $R(z)$, and $\psi(z)$ are the same as in the cartesian representation.

E.3 Astigmatic Mode Functions

Because the x and y components of the field separate in the cartesian solutions, we can, in general, also have solutions $E_{nm}(x,y,x) = u_n(x,z)v_m(y,z)$ with two different Rayleigh ranges for the x and y components. This description is appropriate for resonators with astigmatism, for example with elliptical rather than spherical mirrors.

E.3.1 Expansion of Laguerre-Gaussian Modes into Hermite-Gaussian Modes

In the all-epitaxial cavities, the modes closely resemble Laguerre-Gaussian modes (instead of Hermite-Gaussian modes), because these resonators are almost cylindrically symmetric. Therefore, we are looking for solutions which can meet the boundary conditions with one elliptical mirror (the lens-shaped top reflector of the cavities), i.e. different radii of curvature R_1 and R_2 in the x and y directions, respectively. These solutions also need to equal the Laguerre-Gaussian functions when $R_1 = R_2$.

We thus first need to find the expansion coefficients c_{nm}^{pl} which allow us to write the Laguerre-Gaussian solutions in terms of the Hermite-Gaussian solutions as,

$$E_{pl}(r, \theta, z) = \sum_{n=0}^{\infty} \sum_{m=0}^{\infty} c_{nm}^{pl} E_{nm}(x, y, x)$$

namely, we need t compute

$$c_{nm}^{pl} = \int_0^{2\pi} \int_0^{\infty} E_{pl}(r, \theta, z) u_n^*(r\cos(\theta), z) u_m(r\sin(\theta), z) r dr d\theta$$

These coefficients only depend on the mode indices.

E.3.2 Quasi-Cylindircal Solutions

Now we can construct the solutions to our problem with elliptical mirrors by allowing the functions $E_{nm}(x, y, z)$ in the expansion above to be compsed of two functions $u_n^{(1)}(x)$ and $u_m^{(2)}(y)$ with *different* Rayleigh ranges, i.e. in short,

$$u_n^{(1)}(x) = \Big(\frac{2}{\pi}\Big)^{1/4} \sqrt{\frac{e^{i(2n+1)\psi_1}}{2^n n! w_1}} H_n\Big(\frac{x\sqrt{2}}{w_1}\Big) \exp(-i\frac{kx^2}{2R_1} - \frac{x^2}{w_1^2})$$

$$u_m^{(2)}(y) = \Big(\frac{2}{\pi}\Big)^{1/4} \sqrt{\frac{e^{i(2m+1)\psi_2}}{2^m m! w_2}} H_m\Big(\frac{y\sqrt{2}}{w_2}\Big) \exp(-i\frac{ky^2}{2R_2} - \frac{y^2}{w_2^2})$$

Therefore, our full solutions are given by:

$$\epsilon_{pl}(x, y, x) = \sum_{n=0}^{\infty} \sum_{m=0}^{\infty} c_{nm}^{pl} u_n^{(1)}(x, z) u_m^{(2)}(y, z)$$

or, explicitly,

$$\epsilon_{pl}(x,y,x) = \sqrt{\frac{2}{\pi}}\frac{e^{-i\frac{k}{2}(\frac{x^2}{R_1}+\frac{y^2}{R_2})-(\frac{x^2}{w_1^2}+\frac{y^2}{w_2^2})}}{\sqrt{w_1 w_2}}e^{\frac{i}{2}(\psi_1\psi_2)}$$
$$\times\sum_{n,m} c_{nm}^{pl}\frac{e^{i(n\psi_1+m\psi_2)}}{\sqrt{2^{n+m}n!m!}}H_n\Big(\frac{x\sqrt{2}}{w_1}\Big)H_m\Big(\frac{y\sqrt{2}}{w_2}\Big) \tag{E.3}$$

E.3.3 Resonant Frequencies

The frequencies allowed in the resonator are directly given by the axial phase, ϕ_{pl}, shift during one round trip. We can compute it from the relation

$$e^{2i\phi_{pl}} = \epsilon_{pl}(x,y,z)/\epsilon_{pl}(x,y,z)^*$$
$$e^{2i\phi_{pl}} = \lim_{x,y\to 0}\left(\frac{\sum_{n,m} c_{nm}^{pl}\frac{e^{i(n\psi_1+m\psi_2)}}{\sqrt{2^{n+m}n!m!}}H_n\left(\frac{x\sqrt{2}}{w_1}\right)H_m\left(\frac{y\sqrt{2}}{w_2}\right)}{\sum_{n,m} c_{nm}^{pl}\frac{e^{-i(n\psi_1+m\psi_2)}}{\sqrt{2^{n+m}n!m!}}H_n\left(\frac{x\sqrt{2}}{w_1}\right)H_m\left(\frac{y\sqrt{2}}{w_2}\right)}\right) \tag{E.4}$$

For the $p=0$ modes, this evaluates simply to:

$$\phi_{0l} = \lfloor\frac{l+1}{2}\rfloor\psi_1 + \lfloor\frac{l}{2}\rfloor\psi_2$$

where $\lfloor x\rfloor$ denotes the "entier" function of x, i.e. the greatest integer less than or equal to x.

E.3.4 Plano-Elliptical Resonator

When the bottom mirror has infinite radius of curvature (plane) and the top mirror has radii R_1 and R_2, then the transverse mode splitting for $p=0$ modes is given by:

$$\Delta\omega_{0l} = \frac{\pi c}{nL}\Big(\lfloor\frac{l+1}{2}\rfloor\tan^{-1}\sqrt{L/R_1} + \lfloor\frac{l}{2}\rfloor\tan^{-1}\sqrt{L/R_2}\Big)$$

where L is the cavity height.

E.3.5 Estimates

The lithographically-defined mesas have diameter D and height h, so that when overgrown, they will assume some dome or lens-like shape, with an average radius of curvature give approximately by:

$$R \approx \frac{D^2}{8h}$$

For a typical mesa with $D \sim 6\mu$m, and $h \sim$30nm, we get $R \sim 150\mu$m. This means that we can expect splittings on the order of,

$$\Delta\phi_{0l} \sim \frac{\pi c}{nL} \tan^{-1} \sqrt{L/R}$$

which, for $L \sim 1\mu$m, gives $\Delta E_{0l} \sim$10meV (here n is the refractive index of the medium.)

Bibliography

[1] G. Abstreiter, P. Schittenhelm, C. Engel, E. Silveira, A. Zrenner, D. Meertens, and W. Jager. Growth and characterization of self-assembled Ge-rich islands on Si. *Semicond. Sci. Technol*, 11:1521, 1996.

[2] N. Akopian, NH Lindner, E. Poem, Y. Berlatzky, J. Avron, D. Gershoni, BD Gerardot, and PM Petroff. Entangled Photon Pairs from Semiconductor Quantum Dots. *Physical Review Letters*, 96(13):130501, 2006.

[3] B. Alen, F. Bickel, K. Karrai, R.J. Warburton, and P.M. Petroff. Stark-shift modulation absorption spectroscopy of single quantum dots. *Applied Physics Letters*, 83(11):2235–2237, 2003.

[4] AP Alivisatos. Semiconductor clusters, nanocrystals, and quantum dots. *Science*, 271(5251):933–937, 1996.

[5] L. Allen and J. H. Eberly. *Optical Resonance and Two-Level Atoms.* Dover, New York, 1975.

[6] E. Alphandery, R. J. Nicholas, N. J. Mason, B. Zhang, P. Mock, and G. R. Booker. Self-assembled InSb quantum dots grown on GaSb: A photoluminescence, magnetoluminescence, and atomic force microscopy study. *Applied Physics Letters*, 74(14):2041–2043, 1999.

[7] L.C. Andreani, G. Panzarini, and J.M. Gérard. Strong-coupling regime for quantum boxes in pillar microcavities: Theory. *Physical Review B*, 60(19):13276–13279, 1999.

[8] PK Aravind. Matrix solution of pseudospin equations for three-level systems. *Journal of the Optical Society of America. B, Optical physics(Print)*, 3(7):1025–1032, 1986.

[9] G. Bacher, R. Weigand, J. Seufert, VD Kulakovskii, NA Gippius, A. Forchel, K. Leonardi, and D. Hommel. Biexciton versus Exciton Lifetime in a Single Semiconductor Quantum Dot. *Physical Review Letters*, 83(21):4417–4420, 1999.

[10] Antonio Badolato, Kevin Hennessy, Mete Atature, Jan Dreiser, Evelyn Hu, Pierre M. Petroff, and Atac Imamoglu. Deterministic Coupling of Single Quantum Dots to Single Nanocavity Modes. *Science*, 308(5725):1158–1161, 2005.

[11] O. Baklenov, D. L. Huffaker, A. Anselm, D. G. Deppe, and B. G. Streetman. Influence of Al content on formation of InAlGaAs quantum dots grown by molecular beam epitaxy. *Journal of Applied Physics*, 82(12):6362–6364, 1997.

[12] O. Baklenov, H. Nie, JC Campbell, BG Streetman, and AL Holmes Jr. Long-wavelength luminescence from InGaAs/GaAs quantum dots grown by migration enhanced epitaxy. *Journal of Vacuum Science & Technology B: Microelectronics and Nanometer Structures*, 17:1124, 1999.

[13] M. Bayer and A. Forchel. Temperature dependence of the exciton homogeneous linewidth in In_ {0.60} Ga_ {0.40} As/GaAs self-assembled quantum dots. *Physical Review B*, 65(4):41308, 2002.

[14] M. Bayer, A. Kuther, A. Forchel, A. Gorbunov, V. B. Timofeev, F. Schäfer, J. P. Reithmaier, T. L. Reinecke, and S. N. Walck. Electron and Hole g Factors and Exchange Interaction from Studies of the Exciton Fine Structure In $In_{0.60}Ga_{0.40}As$ Quantum Dots. *Phys. Rev. Lett.*, 82(8):1748–1751, Feb 1999.

[15] M. Bayer, A. Kuther, A. Forchel, A. Gorbunov, VB Timofeev, F. Schäfer, JP Reithmaier, TL Reinecke, and SN Walck. Electron and Hole g Factors and Exchange Interaction from Studies of the Exciton Fine Structure in In_ {0.60} Ga_ {0.40} As Quantum Dots. *Physical Review Letters*, 82(8):1748–1751, 1999.

[16] M. Bayer, T. L. Reinecke, F. Weidner, A. Larionov, A. McDonald, and A. Forchel. Inhibition and Enhancement of the Spontaneous Emission of Quantum Dots in Structured Microresonators. *Phys. Rev. Lett.*, 86(14):3168–3171, Apr 2001.

[17] M. Bayer, O. Stern, P. Hawrylak, S. Fafard, and A. Forchel. Hidden symmetries in the energy levels of excitonic'artificial atoms'. *Nature*, 405(6789):923–6, 2000.

[18] A. Bennett, D. Unitt, P. Atkinson, D. Ritchie, and A. Shields. High

performance single photon sources from photolithographically defined pillar microcavities. *Optics Express*, 13(1):50–55, 2005.

[19] C.H. Bennett and D.P. DiVincenzo. Quantum information and computation. *Nature*, 404(6775):247–255, 2000.

[20] F. Bernardot, P. Nussenzveig, M. Brune, JM Raimond, and S. Haroche. Vacuum Rabi splitting observed on a microscopic atomic sample in a microwave cavity. *Europhysics Letters*, 17:33, 1992.

[21] L. Besombes, J. J. Baumberg, and J. Motohisa. Coherent Spectroscopy of Optically Gated Charged Single InGaAs Quantum Dots. *Phys. Rev. Lett.*, 90(25):257402, Jun 2003.

[22] L. Besombes, JJ Baumberg, and J. Motohisa. Polarization-dependent Rabi oscillations in single InGaAs quantum dots. *Semicond. Sci. Technol*, 19(4):S148–S151, 2004.

[23] P. Bianucci, A. Muller, CK Shih, QQ Wang, QK Xue, and C. Piermarocchi. Experimental realization of the one qubit Deutsch-Jozsa algorithm in a quantum dot. *Physical Review B*, 69(16):161303, 2004.

[24] D. Birkedal, K. Leosson, and JM Hvam. Long Lived Coherence in Self-Assembled Quantum Dots. *Physical Review Letters*, 87(22):227401, 2001.

[25] N. H. Bonadeo, J. Erland, D. Gammon, D. Park, D. S. Katzer, and D. G. Steel. Coherent Optical Control of the Quantum State of a Single Quantum Dot. *Science*, 282(5393):1473–1476, 1998.

[26] P. Borri, W. Langbein, J.M. Hvam, F. Heinrichsdorff, MH Mao, and D. Bimberg. Time-resolved four-wave mixing in InAs/InGaAs quantum-dot amplifiers under electrical injection. *Applied Physics Letters*, 76(11):1380, 2000.

[27] P. Borri, W. Langbein, J. Mørk, JM Hvam, F. Heinrichsdorff, M.H. Mao, and D. Bimberg. Dephasing in InAs/GaAs quantum dots. *Physical Review B*, 60(11):7784–7787, 1999.

[28] P. Borri, W. Langbein, S. Schneider, U. Woggon, R. L. Sellin, D. Ouyang, and D. Bimberg. Ultralong Dephasing Time in InGaAs Quantum Dots. *Phys. Rev. Lett.*, 87(15):157401, Sep 2001.

[29] P. Borri, W. Langbein, S. Schneider, U. Woggon, R. L. Sellin, D. Ouyang, and D. Bimberg. Rabi oscillations in the excitonic ground-state transition of InGaAs quantum dots. *Phys. Rev. B*, 66(8):081306, Aug 2002.

[30] P. Borri, W. Langbein, S. Schneider, U. Woggon, R. L. Sellin, D. Ouyang, and D. Bimberg. Relaxation and Dephasing of Multiexcitons in Semiconductor Quantum Dots. *Phys. Rev. Lett.*, 89(18):187401, Oct 2002.

[31] J. R. R. Bortoleto, H. R. Gutierrez, M. A. Cotta, and J. Bettini. Mechanism of lateral ordering of InP dots grown on InGaP layers. *Applied Physics Letters*, 87(1):013105, 2005.

[32] Alfio Borzì, Georg Stadler, and Ulrich Hohenester. Optimal quantum control in nanostructures: Theory and application to a generic three-level system. *Phys. Rev. A*, 66(5):053811, Nov 2002.

[33] R. Brouri, A. Beveratos, J.P. Poizat, and P. Grangier. Photon antibunching in the fluorescence of individual color centers in diamond. *Opt. Lett*, 25(17):1294–1296, 2000.

[34] M. Bruchez Jr, M. Moronne, P. Gin, S. Weiss, and A.P. Alivisatos. Semiconductor nanoparticles as fluorescent biological labels [J]. *Science*, 281:2013–2016, 1998.

[35] K. Brunner, G. Abstreiter, G. Böhm, G. Tränkle, and G. Weimann. Sharp-Line Photoluminescence and Two-Photon Absorption of Zero-Dimensional Biexcitons in a GaAs/AlGaAs Structure. *Physical Review Letters*, 73(8):1138–1141, 1994.

[36] N. Carlsson, W. Seifert, A. Petersson, P. Castrillo, M. E. Pistol, and L. Samuelson. Study of the two-dimensional–three-dimensional growth mode transition in metalorganic vapor phase epitaxy of GaInP/InP quantum-sized structures. *Applied Physics Letters*, 65(24):3093–3095, 1994.

[37] Wen-Hao Chang, Wen-Yen Chen, Hsiang-Szu Chang, Tung-Po Hsieh, Jen-Inn Chyi, and Tzu-Min Hsu. Efficient Single-Photon Sources Based on Low-Density Quantum Dots in Photonic-Crystal Nanocavities. *Physical Review Letters*, 96(11):117401, 2006.

[38] G. Chen, NH Bonadeo, DG Steel, D. Gammon, DS Katzer, D. Park, and LJ Sham. Optically Induced Entanglement of Excitons in a Single Quantum Dot. *Science*, 289(5486):1906–1909, 2000.

[39] C. Cohen-Tannoudji, B. Diu, F. Laloë, and S.R. Hemley. *Quantum mechanics.. Vol. 1.* Wiley Interscience;, 1977.

[40] Q. Deng, H. Deng, and DG Deppe. Radiation fields from whispering-gallery modes of oxide-confined vertical-cavity surface-emitting lasers. *Optics Letters*, 22(7):463–465, 1997.

[41] DG Deppe, LA Graham, and DL Huffaker. Enhanced spontaneous emission using quantum dots and an aperturedmicrocavity. *Quantum Electronics, IEEE Journal of*, 35(10):1502–1508, 1999.

[42] DJ Eaglesham and M. Cerullo. Dislocation-free Stranski-Krastanow growth of Ge on Si (100). *Physical Review Letters*, 64(16):1943–1946, 1990.

[43] A. Einstein, B. Podolsky, and N. Rosen. Can quantum-mechanical description of physical reality be considered complete? *Physical Review*, 47:777, 1935.

[44] Dirk Englund, David Fattal, Edo Waks, Glenn Solomon, Bingyang Zhang, Toshihiro Nakaoka, Yasuhiko Arakawa, Yoshihisa Yamamoto, and Jelena Vuckovic. Controlling the Spontaneous Emission Rate of Single Quantum Dots in a Two-Dimensional Photonic Crystal. *Physical Review Letters*, 95(1):013904, 2005.

[45] X. Fan, P. Palinginis, S. Lacey, H. Wang, and M.C. Lonergan. Coupling semiconductor nanocrystals to a fused-silica microsphere: a quantum-dot microcavity with extremely high Q factors. *Opt. Lett*, 25(21):1600–1602, 2000.

[46] Xudong Fan, Mark C. Lonergan, Yuzhong Zhang, and Hailin Wang. Enhanced spontaneous emission from semiconductor nanocrystals embedded in whispering gallery optical microcavities. *Phys. Rev. B*, 64(11):115310, Aug 2001.

[47] I. Favero, G. Cassabois, C. Voisin, C. Delalande, Ph. Roussignol, R. Ferreira, C. Couteau, J. P. Poizat, and J. M. Gerard. Fast exciton spin relaxation in single quantum dots. *Physical Review B (Condensed Matter and Materials Physics)*, 71(23):233304, 2005.

[48] Z. Ficek and S. Swain. Simulating quantum interference in a three-level system with perpendicular transition dipole moments. *Physical Review A (Atomic, Molecular, and Optical Physics)*, 69(2):023401, 2004.

[49] F. Findeis, M. Baier, E. Beham, A. Zrenner, and G. Abstreiter. Photocurrent and photoluminescence of a single self-assembled quantum dot

in electric fields. *Applied Physics Letters*, 78(19):2958, 2001.

[50] J. Förstner, C. Weber, J. Danckwerts, and A. Knorr. Phonon-Assisted Damping of Rabi Oscillations in Semiconductor Quantum Dots. *Phys. Rev. Lett.*, 91(12):127401, Sep 2003.

[51] S. Francoeur, JF Klem, and A. Mascarenhas. Optical Spectroscopy of Single Impurity Centers in Semiconductors. *Physical Review Letters*, 93(6):67403, 2004.

[52] Ilya Fushman, Dirk Englund, and Jelena Vuckovic. Coupling of PbS quantum dots to photonic crystal cavities at room temperature. *Applied Physics Letters*, 87(24):241102, 2005.

[53] D. Gammon, Al. L. Efros, T. A. Kennedy, M. Rosen, D. S. Katzer, D. Park, S. W. Brown, V. L. Korenev, and I. A. Merkulov. Electron and Nuclear Spin Interactions in the Optical Spectra of Single GaAs Quantum Dots. *Phys. Rev. Lett.*, 86(22):5176–5179, May 2001.

[54] D. Gammon, ES Snow, BV Shanabrook, DS Katzer, and D. Park. Fine Structure Splitting in the Optical Spectra of Single GaAs Quantum Dots. *Physical Review Letters*, 76(16):3005–3008, 1996.

[55] D. Gammon, ES Snow, BV Shanabrook, DS Katzer, and D. Park. Homogeneous Linewidths in the Optical Spectrum of a Single Gallium Arsenide Quantum Dot. *Science*, 273(5271):87, 1996.

[56] J. M. Gérard, B. Sermage, B. Gayral, B. Legrand, E. Costard, and V. Thierry-Mieg. Enhanced Spontaneous Emission by Quantum Boxes in a Monolithic Optical Microcavity. *Phys. Rev. Lett.*, 81(5):1110–1113, Aug 1998.

[57] M. Grundmann, J. Christen, NN Ledentsov, J. Böhrer, D. Bimberg, SS Ruvimov, P. Werner, U. Richter, U. Gösele, J. Heydenreich, et al. Ultranarrow Luminescence Lines from Single Quantum Dots. *Physical Review Letters*, 74(20):4043–4046, 1995.

[58] T. Guenther, C. Lienau, T. Elsaesser, M. Glanemann, V.M. Axt, T. Kuhn, S. Eshlaghi, and A.D. Wieck. Coherent Nonlinear Optical Response of Single Quantum Dots Studied by Ultrafast Near-Field Spectroscopy. *Physical Review Letters*, 89(5):57401, 2002.

[59] JR Guest, TH Stievater, G. Chen, EA Tabak, BG Orr, DG Steel, D. Gammon, and DS Katzer. Near-field coherent spectroscopy and microscopy of a quantum dot system. *Science(Washington, D. C.)*, 293(5538):2224–2227, 2001.

[60] JR Guest, TH Stievater, X. Li, J. Cheng, DG Steel, D. Gammon, DS Katzer, D. Park, C. Ell, A. Thränhardt, et al. Measurement of optical absorption by a single quantum dot exciton. *Physical Review B*, 65(24):241310, 2002.

[61] T. D. Happ, I. I. Tartakovskii, V. D. Kulakovskii, J.-P. Reithmaier, M. Kamp, and A. Forchel. Enhanced light emission of $In_xGa_{1-x}As$

quantum dots in a two-dimensional photonic-crystal defect microcavity. *Phys. Rev. B*, 66(4):041303, Jul 2002.

[62] S. Haroche and D. Kleppner. Cavity Quantum Electrodynamics. *Physics Today*, 42:24, 1989.

[63] F. Hatami, N. N. Ledentsov, M. Grundmann, J. Bohrer, F. Heinrichsdorff, M. Beer, D. Bimberg, S. S. Ruvimov, P. Werner, U. Gosele, J. Heydenreich, U. Richter, S. V. Ivanov, B. Ya. Meltser, P. S. Kop'ev, and Zh. I. Alferov. Radiative recombination in type-II GaSb/GaAs quantum dots. *Applied Physics Letters*, 67(5):656–658, 1995.

[64] P. Hawrylak, GA Narvaez, M. Bayer, and A. Forchel. Excitonic Absorption in a Quantum Dot. *Physical Review Letters*, 85(2):389–392, 2000.

[65] HF Hess, E. Betzig, TD Harris, LN Pfeiffer, and KW West. Near-Field Spectroscopy of the Quantum Constituents of a Luminescent System. *Science*, 264(5166):1740, 1994.

[66] A. Högele, S. Seidl, M. Kroner, K. Karrai, R.J. Warburton, B.D. Gerardot, and P.M. Petroff. Voltage-Controlled Optics of a Quantum Dot. *Physical Review Letters*, 93(21):217401, 2004.

[67] S. Hoppe, G. Ctistis, J.J. Paggel, and P. Fumagalli. Reflection scanning near-field optical microscopy in ultrahigh vacuum. *Review of Scientific Instruments*, 76(6):63704–63704, 2005.

[68] H. Htoon and Shih C. K. *Studies on quantum coherence phenomena of self-assembled quantum dots*. PhD thesis, The University of Texas at Austin, Austin, Texas, 2001.

[69] H. Htoon, D. Kulik, O. Baklenov, A. L. Holmes, T. Takagahara, and C. K. Shih. Carrier relaxation and quantum decoherence of excited states in self-assembled quantum dots. *Phys. Rev. B*, 63(24):241303, Jun 2001.

[70] H. Htoon, T. Takagahara, D. Kulik, O. Baklenov, AL Holmes Jr, and CK Shih. Interplay of Rabi Oscillations and Quantum Interference in Semiconductor Quantum Dots. *Physical Review Letters*, 88(8):87401, 2002.

[71] H. Htoon, H. Yu, D. Kulik, JW Keto, O. Baklenov, AL Holmes Jr, BG Streetman, and CK Shih. Quantum dots at the nanometer scale: Interdot carrier shuffling and multiparticle states. *Physical Review B*, 60(15):11026–11029, 1999.

[72] YZ Hu, SW Koch, M. Lindberg, N. Peyghambarian, EL Pollock, and F.F. Abraham. Biexcitons in semiconductor quantum dots. *Physical Review Letters*, 64(15):1805–1807, 1990.

[73] DL Huffaker and DG Deppe. Electroluminescence efficiency of 1.3 m wavelength InGaAs/GaAs quantum dots. *Appl. Phys. Lett*, 73(4):520–522, 1998.

[74] H. Kamada, H. Gotoh, J. Temmyo, T. Takagahara, and H. Ando. Exciton Rabi Oscillation in a Single Quantum Dot. *Phys. Rev. Lett.*, 87(24):246401, Nov 2001.

[75] C. Kammerer, G. Cassabois, C. Voisin, C. Delalande, P. Roussignol, and JM Gérard. Photoluminescence Up-Conversion in Single Self-Assembled InAs/GaAs Quantum Dots. *Physical Review Letters*, 87(20):207401, 2001.

[76] C. Kammerer, G. Cassabois, C. Voisin, M. Perrin, C. Delalande, Ph. Roussignol, and J. M. Gerard. Interferometric correlation spectroscopy in single quantum dots. *Applied Physics Letters*, 81(15):2737–2739, 2002.

[77] J.W. Keto, M.F. Becker, D. Kovar, G. Malyavanatham, A. Muller, D.T. O'Brien, CK Shih, and J. Wang. Nanoparticles of Er-doped glass produced by laser ablation of microparticles. *Journal of the Optical Society of America B*, 23(8):1581–1585, 2006.

[78] H. J. Kimble and L. Mandel. Theory of resonance fluorescence. *Phys. Rev. A*, 13(6):2123–2144, Jun 1976.

[79] A. Kiraz, P. Michler, C. Becher, B. Gayral, A. Imamoglu, Lidong Zhang, E. Hu, W. V. Schoenfeld, and P. M. Petroff. Cavity-quantum electrodynamics using a single InAs quantum dot in a microdisk structure. *Applied Physics Letters*, 78(25):3932–3934, 2001.

[80] N. Kirstaedter, NN Ledentsov, M. Grundmann, D. Bimberg, VM Ustinov, SS Ruvimov, MV Maximov, PS Kop'ev, Z.I. Alferov, U. Richter, et al. Low threshold, large T injection laser emission from (InGa) As quantum dots. *Electronics Letters*, 30:1416, 1994.

[81] V. I. Klimov, A. A. Mikhailovsky, Su Xu, A. Malko, J. A. Hollingsworth, C. A. Leatherdale, H.-J. Eisler, and M. G. Bawendi. Optical Gain and Stimulated Emission in Nanocrystal Quantum Dots. *Science*, 290(5490):314–317, 2000.

[82] A. Kress, F. Hofbauer, N. Reinelt, M. Kaniber, H. J. Krenner, R. Meyer, G. Bohm, and J. J. Finley. Manipulation of the spontaneous emission dynamics of quantum dots in two-dimensional photonic crystals. *Physical Review B (Condensed Matter and Materials Physics)*, 71(24):241304, 2005.

[83] A. Kurtenbach, K. Eberl, and T. Shitara. Nanoscale InP islands embedded in InGaP. *Applied Physics Letters*, 66(3):361–363, 1995.

[84] C. Kurtsiefer, S. Mayer, P. Zarda, and H. Weinfurter. Stable Solid-State Source of Single Photons. *Physical Review Letters*, 85(2):290–293, 2000.

[85] I.L. Kuskovsky, C. Tian, GF Neumark, JE Spanier, I.P. Herman, W.C. Lin, SP Guo, and MC Tamargo. Optical properties of δ-doped ZnSe: Te grown by molecular beam epitaxy: The role of tellurium. *Physical Review B*, 63(15):155205, 2001.

[86] Olivier Labeau, Philippe Tamarat, and Brahim Lounis. Temperature Dependence of the Luminescence Lifetime of Single $CdSe/ZnS$ Quantum Dots. *Phys. Rev. Lett.*, 90(25):257404, Jun 2003.

[87] Wolfgang Langbein and Brian Patton. Microscopic Measurement of Photon Echo Formation in Groups of Individual Excitonic Transitions. *Physical Review Letters*, 95(1):017403, 2005.

[88] D. Lee, A. Mysyrowicz, AV Nurmikko, and BJ Fitzpatrick. Exciton self-trapping in ZnSe-ZnTe alloys. *Physical Review Letters*, 58(14):1475–1478, 1987.

[89] A. S. Lenihan, M. V. Gurudev Dutt, D. G. Steel, S. Ghosh, and P. K. Bhattacharya. Raman Coherence Beats from Entangled Polarization Eigenstates in InAs Quantum Dots. *Phys. Rev. Lett.*, 88(22):223601, May 2002.

[90] P. Lerouxhugon and H. Mariette. Stochastic transfer of excitations and exhancement of the NN_α-pair luminescence in GaP: N. *Phys. Rev. B*, 30(3):1622–1625, Aug 1984.

[91] Xiaoqin Li, Yanwen Wu, Duncan Steel, D. Gammon, T. H. Stievater, D. S. Katzer, D. Park, C. Piermarocchi, and L. J. Sham. An All-Optical Quantum Gate in a Semiconductor Quantum Dot. *Science*, 301(5634):809–811, 2003.

[92] N. Liu, J. Tersoff, O. Baklenov, AL Holmes Jr, and CK Shih. Nonuniform Composition Profile in In$_{0.5}$Ga$_{0}$.5As Alloy Quantum Dots. *Physical Review Letters*, 84(2):334–337, 2000.

[93] A. Loffler, J. P. Reithmaier, G. Sek, C. Hofmann, S. Reitzenstein, M. Kamp, and A. Forchel. Semiconductor quantum dot microcavity pillars with high-quality factors and enlarged dot dimensions. *Applied Physics Letters*, 86(11):111105, 2005.

[94] N. Louvion, D. Gerard, J. Mouette, F. de Fornel, C. Seassal, X. Letartre, A. Rahmani, and S. Callard. Local Observation and Spectroscopy of Optical Modes in an Active Photonic-Crystal Microcavity. *Physical Review Letters*, 94(11):113907, 2005.

[95] D. Lu, J. Ahn, S. Freisem, D. Gazula, and D. G. Deppe. Lens-shaped all-epitaxial quantum dot microcavity. *Applied Physics Letters*, 87(16):163105, 2005.

[96] D. Lu, J. Ahn, H. Huang, and D. G. Deppe. All-epitaxial mode-confined vertical-cavity surface-emitting laser. *Applied Physics Letters*, 85(12):2169–2171, 2004.

[97] PA Maksym and T. Chakraborty. Quantum dots in a magnetic field: Role of electron-electron interactions. *Physical Review Letters*, 65(1):108–111, 1990.

[98] S. M. Mansfield and G. S. Kino. Solid immersion microscope. *Applied Physics Letters*, 57(24):2615–2616, 1990.

[99] J.Y. Marzin, J.M. Gérard, A. Izraël, D. Barrier, and G. Bastard. Photoluminescence of Single InAs Quantum Dots Obtained by Self-Organized Growth on GaAs. *Physical Review Letters*, 73(5):716–719, 1994.

[100] K. Matsuda, T. Saiki, S. Nomura, M. Mihara, Y. Aoyagi, S. Nair, and T. Takagahara. Near-Field Optical Mapping of Exciton Wave Functions in a GaAs Quantum Dot. *Physical Review Letters*, 91(17):177401, 2003.

[101] J. McKeever, A. Boca, AD Boozer, and JR Buck. Experimental realization of a one-atom laser in the regime of strong coupling. *Nature*, 425:268–271, 2003.

[102] J. McKeever, A. Boca, AD Boozer, R. Miller, JR Buck, A. Kuzmich, and HJ Kimble. Deterministic generation of single photons from one atom trapped in a cavity. *Science(Washington)*, 303(5666):1992–1994, 2004.

[103] P. Meystre and M. Sargent III. *Elements of Quantum Optics*. Springer, 3rd edition, 1999.

[104] P. Michler. *Single Quantum Dots: Fundamentals, Applications and New Concepts*. Springer, 2003.

[105] P. Michler, A. Imamoglu, MD Mason, PJ Carson, GF Strouse, and SK Buratto. Quantum correlation among photons from a single quantum dot at room temperature. *Nature*, 406(6799):698–970, 2000.

[106] P. Michler, A. Kiraz, C. Becher, W. V. Schoenfeld, P. M. Petroff, Lidong Zhang, E. Hu, and A. Imamoglu. A Quantum Dot Single-Photon Turnstile Device. *Science*, 290(5500):2282–2285, 2000.

[107] B. R. Mollow. Resonant Scattering of Radiation from Collision-Damped Two-Level Systems. *Phys. Rev. A*, 2(1):76–80, Jul 1970.

[108] BR Mollow. Power Spectrum of Light Scattered by Two-Level Systems. *Physical Review*, 188(5):1969–1975, 1969.

[109] A. Muller, P. Bianucci, C. Piermarocchi, M. Fornari, IC Robin, R. André, and CK Shih. Time-resolved photoluminescence spectroscopy of individual Te impurity centers in ZnSe. *Physical Review B*, 73(8):81306, 2006.

[110] A. Muller, D. Lu, J. Ahn, D. Gazula, S. Quadery, S. Freisem, D.G. Deppe, and C.K. Shih. Self-Aligned All-Epitaxial Microcavity for Cavity QED with Quantum Dots. *Nano Letters*, 6(12):2920–2924, 2006.

[111] A. Muller, C.K. Shih, J. Ahn, D. Lu, and D.G. Deppe. Isolated single quantum dot emitters in all-epitaxial microcavities. *Optics Letters*, 31(4):528–530, 2006.

[112] A. Muller, C.K. Shih, J. Ahn, D. Lu, D. Gazula, and D.G. Deppe. High (33 000) all-epitaxial microcavity for quantum dot vertical-cavity surface-emitting lasers and quantum light sources. *Applied Physics Letters*, 88(3):31107–31107, 2006.

[113] A. Muller, QQ Wang, P. Bianucci, CK Shih, and QK Xue. Determination of anisotropic dipole moments in self-assembled quantum dots using Rabi oscillations. *Applied Physics Letters*, 84(6):981–983, 2004.

[114] DF Nelson, JD Cuthbert, PJ Dean, and DG Thomas. Auger Recombination of Excitons Bound to Neutral Donors in Gallium Phosphide and Silicon. *Physical Review Letters*, 17(25):1262–1265, 1966.

[115] M.A. Nielsen and I.L. Chuang. *Quantum computation and quantum information.* Cambridge University Press, 2000.

[116] M. Nirmal, D. J. Norris, M. Kuno, M. G. Bawendi, Al. L. Efros, and M. Rosen. Observation of the "Dark Exciton" in CdSe Quantum Dots. *Phys. Rev. Lett.*, 75(20):3728–3731, Nov 1995.

[117] ZY Ou, SF Pereira, HJ Kimble, and KC Peng. Realization of the Einstein-Podolsky-Rosen paradox for continuous variables. *Physical Review Letters*, 68(25):3663–3666, 1992.

[118] Y.S. Park, A.K. Cook, and H. Wang. Cavity QED with Diamond Nanocrystals and Silica Microspheres. *Arxiv preprint cond-mat/0608493*, 2006.

[119] MD Pashley, KW Haberern, W. Friday, JM Woodall, and PD Kirchner. Structure of GaAs (001)(2× 4)-c (2× 8) Determined by Scanning Tunneling Microscopy. *Physical Review Letters*, 60(21):2176–2179, 1988.

[120] PP Paskov, PO Holtz, B. Monemar, JM Garcia, WV Schoenfeld, and PM Petroff. Photoluminescence up-conversion in InAs/GaAs self-assembled quantum dots. *Applied Physics Letters*, 77(6):812–814, 2006.

[121] B. Patton, U. Woggon, and W. Langbein. Coherent Control and Polarization Readout of Individual Excitonic States. *Physical Review Letters*, 95(26):266401, 2005.

[122] Matthew Pelton, Charles Santori, Jelena Vucˇković, Bingyang Zhang, Glenn S. Solomon, Jocelyn Plant, and Yoshihisa Yamamoto. Efficient Source of Single Photons: A Single Quantum Dot in a Micropost Microcavity. *Phys. Rev. Lett.*, 89(23):233602, Nov 2002.

[123] E. Peter, P. Senellart, D. Martrou, A. Lemaitre, J. Hours, J. M. Gerard, and J. Bloch. Exciton-Photon Strong-Coupling Regime for a Single Quantum Dot Embedded in a Microcavity. *Physical Review Letters*, 95(6):067401, 2005.

[124] D. V. Regelman, U. Mizrahi, D. Gershoni, E. Ehrenfreund, W. V. Schoenfeld, and P. M. Petroff. Semiconductor Quantum Dot: A Quantum Light Source of Multicolor Photons with Tunable Statistics. *Phys. Rev. Lett.*, 87(25):257401, Nov 2001.

[125] JP Reithmaier, G. Sek, A. Loeffler, C. Hofmann, S. Kuhn, S. Reitzenstein, LV Keldysh, VD Kulakovskii, TL Reinecke, and A. Forchel. Strong coupling in a single quantum dot-semiconductor microcavity system. *Nature*, 432(7014):197–200, 2004.

[126] T. Rivera, J.-P. Debray, J. M. Gerard, B. Legrand, L. Manin-Ferlazzo, and J. L. Oudar. Optical losses in plasma-etched AlGaAs microresonators using reflection spectroscopy. *Applied Physics Letters*, 74(7):911–913, 1999.

[127] A. Rosenauer, T. Reisinger, F. Franzen, G. Schutz, B. Hahn, K. Wolf, J. Zweck, and W. Gebhardt. Transmission electron microscopy and reflected high-energy electron-diffraction investigation of plastic relaxation in doped and undoped ZnSe/GaAs(001). *Journal of Applied Physics*, 79(8):4124–4131, 1996.

[128] C. Santori, D. Fattal, J. Vuckovic, G.S. Solomon, and Y. Yamamoto. Indistinguishable photons from a single-photon device. *Nature*, 419(6907):594–597, 2002.

[129] C. Santori, D. Fattal, J. Vuckovic, G.S. Solomon, and Y. Yamamoto. Single-photon generation with InAs quantum dots. *New Journal of Physics*, 6(1):89, 2004.

[130] C. Santori, M. Pelton, G. Solomon, Y. Dale, and Y. Yamamoto. Triggered Single Photons from a Quantum Dot. *Physical Review Letters*, 86(8):1502–1505, 2001.

[131] D. Sanvitto, A. Daraei, A. Tahraoui, M. Hopkinson, P. W. Fry, D. M. Whittaker, and M. S. Skolnick. Observation of ultrahigh quality factor in a semiconductor microcavity. *Applied Physics Letters*, 86(19):191109, 2005.

[132] M. O. Scully and M. S. Zubairy. *Quantum Optics*. Cambridge University Press, 1997.

[133] J. Shah. Ultrafast luminescence spectroscopy using sum frequency generation. *Quantum Electronics, IEEE Journal of*, 24(2):276–288, 1988.

[134] K. Shahzad. Excitonic transitions in ZnSe epilayers grown on GaAs. *Physical Review B*, 38(12):8309–8312, 1988.

[135] J. M. Smith, P. A. Dalgarno, R. J. Warburton, A. O. Govorov, K. Karrai, B. D. Gerardot, and P. M. Petroff. Voltage Control of the Spin Dynamics of an Exciton in a Semiconductor Quantum Dot. *Physical Review Letters*, 94(19):197402, 2005.

[136] G. S. Solomon, M. Pelton, and Y. Yamamoto. Single-mode Spontaneous Emission from a Single Quantum Dot in a Three-Dimensional Microcavity. *Phys. Rev. Lett.*, 86(17):3903–3906, Apr 2001.

[137] Kartik Srinivasan, Matthew Borselli, Thomas J. Johnson, Paul E. Barclay, Oskar Painter, Andreas Stintz, and Sanjay Krishna. Optical loss and lasing characteristics of high-quality-factor AlGaAs microdisk

resonators with embedded quantum dots. *Applied Physics Letters*, 86(15):151106, 2005.

[138] RM Stevenson, RJ Young, P. Atkinson, K. Cooper, DA Ritchie, and AJ Shields. A semiconductor source of triggered entangled photon pairs. *Nature*, 439(7073):179–82, 2006.

[139] T. H. Stievater, Xiaoqin Li, T. Cubel, D. G. Steel, D. Gammon, D. S. Katzer, and D. Park. Measurement of relaxation between polarization eigenstates in single quantum dots. *Applied Physics Letters*, 81(22):4251–4253, 2002.

[140] T. H. Stievater, Xiaoqin Li, D. G. Steel, D. Gammon, D. S. Katzer, D. Park, C. Piermarocchi, and L. J. Sham. Rabi Oscillations of Excitons in Single Quantum Dots. *Phys. Rev. Lett.*, 87(13):133603, Sep 2001.

[141] TH Stievater, X. Li, DG Steel, D. Gammon, DS Katzer, and D. Park. Transient nonlinear spectroscopy of excitons and biexcitons in single quantum dots. *Physical Review B*, 65(20):205319, 2002.

[142] N. G. Stoltz, M. Rakher, S. Strauf, A. Badolato, D. D. Lofgreen, P. M. Petroff, L. A. Coldren, and D. Bouwmeester. High-quality factor optical microcavities using oxide apertured micropillars. *Applied Physics Letters*, 87(3):031105, 2005.

[143] IN Stranski and L. Krastanow. Zur Theorie der orientierten Ausscheidung von Ionenkristallen aufeinander, Akad. Wiss. Lit. Wien Math.

Natur. Kl IIb, 146:797, 1937.

[144] S. Strauf, K. Hennessy, M. T. Rakher, Y.-S. Choi, A. Badolato, L. C. Andreani, E. L. Hu, P. M. Petroff, and D. Bouwmeester. Self-Tuned Quantum Dot Gain in Photonic Crystal Lasers. *Physical Review Letters*, 96(12):127404, 2006.

[145] S. Strauf, P. Michler, M. Klude, D. Hommel, G. Bacher, and A. Forchel. Quantum Optical Studies on Individual Acceptor Bound Excitons in a Semiconductor. *Physical Review Letters*, 89(17):177403, 2002.

[146] S. Stufler, P. Ester, A. Zrenner, and M. Bichler. Quantum optical properties of a single $\mathrm{In}_x\mathrm{Ga}_{1-x}\mathrm{As}$-GaAs quantum dot two-level system. *Physical Review B*, 72(12):121301, 2005.

[147] S. Stufler, P. Ester, A. Zrenner, and M. Bichler. Ramsey Fringes in an Electric-Field-Tunable Quantum Dot System. *Physical Review Letters*, 96(3):37402, 2006.

[148] S. Stufler, P. Machnikowski, P. Ester, M. Bichler, VM Axt, T. Kuhn, and A. Zrenner. Two-photon Rabi oscillations in a single $\mathrm{In}_x\mathrm{Ga}_{1-x}\mathrm{As}$/ GaAs quantum dot. *Physical Review B*, 73(12):125304, 2006.

[149] RJ Thompson, G. Rempe, and HJ Kimble. Observation of normal-mode splitting for an atom in an optical cavity. *Physical Review Letters*, 68(8):1132–1135, 1992.

[150] Y. Toda, O. Moriwaki, M. Nishioka, and Y. Arakawa. Efficient Carrier Relaxation Mechanism in InGaAs/GaAs Self-Assembled Quantum Dots Based on the Existence of Continuum States. *Phys. Rev. Lett.*, 82(20):4114–4117, May 1999.

[151] D. C. Unitt, A. J. Bennett, P. Atkinson, D. A. Ritchie, and A. J. Shields. Polarization control of quantum dot single-photon sources via a dipole-dependent Purcell effect. *Physical Review B (Condensed Matter and Materials Physics)*, 72(3):033318, 2005.

[152] T. Unold, K. Mueller, C. Lienau, T. Elsaesser, and A.D. Wieck. Optical Stark Effect in a Quantum Dot: Ultrafast Control of Single Exciton Polarizations. *Physical Review Letters*, 92(15):157401, 2004.

[153] T. Unold, K. Mueller, C. Lienau, T. Elsaesser, and A.D. Wieck. Optical Control of Excitons in a Pair of Quantum Dots Coupled by the Dipole-Dipole Interaction. *Physical Review Letters*, 94(13):137404, 2005.

[154] K. Vahala. Optical Microcavities. *Nature*, 424(6950):839–846, Aug 2003.

[155] A. Vasanelli, R. Ferreira, and G. Bastard. Continuous Absorption Background and Decoherence in Quantum Dots. *Phys. Rev. Lett.*, 89(21):216804, Nov 2002.

[156] D. W. Vernooy, A. Furusawa, N. Ph. Georgiades, V. S. Ilchenko, and H. J. Kimble. Cavity QED with high-Q whispering gallery modes.

Phys. Rev. A, 57(4):R2293–R2296, Apr 1998.

[157] J. M. Villas-Boas, Sergio E. Ulloa, and A. O. Govorov. Decoherence of Rabi Oscillations in a Single Quantum Dot. *Physical Review Letters*, 94(5):057404, 2005.

[158] Q. Q. Wang, A. Muller, P. Bianucci, E. Rossi, Q. K. Xue, T. Takagahara, C. Piermarocchi, A. H. MacDonald, and C. K. Shih. Decoherence processes during optical manipulation of excitonic qubits in semiconductor quantum dots. *Physical Review B (Condensed Matter and Materials Physics)*, 72(3):035306, 2005.

[159] QQ Wang, A. Muller, MT Cheng, HJ Zhou, P. Bianucci, and CK Shih. Coherent Control of a V-Type Three-Level System in a Single Quantum Dot. *Physical Review Letters*, 95(18):187404, 2005.

[160] XY Wang, WQ Ma, JY Zhang, GJ Salamo, M. Xiao, and CK Shih. Photoluminescence intermittency of InGaAs/GaAs quantum dots confined in a planar microcavity. *Nano Lett*, 5(10):1873–1877, 2005.

[161] L. Worschech, W. Ossau, C. Fischer, H. Schafer, and G. Landwehr. Characterization of structural defects in MBE grown ZnSe. *Mat. Sci. Eng. B*, 43:29, 1997.

[162] F. Y. Wu, R. E. Grove, and S. Ezekiel. Investigation of the Spectrum of Resonance Fluorescence Induced by a Monochromatic Field. *Phys. Rev. Lett.*, 35(21):1426–1429, Nov 1975.

[163] Q. Wu, R.D. Grober, D. Gammon, and DS Katzer. Imaging Spectroscopy of Two-Dimensional Excitons in a Narrow GaAs/AlGaAs Quantum Well. *Physical Review Letters*, 83(13):2652–2655, 1999.

[164] Y. Wu, X. Li, LM Duan, DG Steel, and D. Gammon. Density Matrix Tomography through Sequential Coherent Optical Rotations of an Exciton Qubit in a Single Quantum Dot. *Physical Review Letters*, 96(8):87402, 2006.

[165] S. H. Xin, P. D. Wang, Aie Yin, C. Kim, M. Dobrowolska, J. L. Merz, and J. K. Furdyna. Formation of self-assembling CdSe quantum dots on ZnSe by molecular beam epitaxy. *Applied Physics Letters*, 69(25):3884–3886, 1996.

[166] C. S. Yang, D. Y. Hong, C. Y. Lin, W. C. Chou, C. S. Ro, W. Y. Uen, W. H. Lan, and S. L. Tu. Optical properties of the $\mathrm{ZnSe}_{1-x}\mathrm{Te}_x$ epilayers grown by molecular beam epitaxy. *Journal of Applied Physics*, 83(5):2555–2559, 1998.

[167] T. Yao, H. Tanino, M. Kato, and JJ Davies. Photoluminescence of excitons bound at Te isoelectronic traps in ZnSe. *American Association for Crystal Growth, International Conference on II-VI Compounds, 3rd, Monterey, CA, July 12-17, 1987) Journal of Crystal Growth (ISSN 0022-0248),*, 86(1-4):552–557, 1988.

[168] A. Yariv. *Quantum Electronics*. Wiley, 3rd edition, 1988.

[169] T. Yoshie, A. Scherer, J. Hendrickson, HM Gibbs, G. Rupper, C. Ell, OB Shchekin, and DG Deppe. Vacuum Rabi splitting with a single quantum dot in a photonic crystal nanocavity. *Nature*, 432:200–203, 2004.

[170] Zhiliang Yuan, Beata E. Kardynal, R. Mark Stevenson, Andrew J. Shields, Charlene J. Lobo, Ken Cooper, Neil S. Beattie, David A. Ritchie, and Michael Pepper. Electrically Driven Single-Photon Source. *Science*, 295(5552):102–105, 2002.

[171] L. Zhang, T.F. Boggess, DG Deppe, DL Huffaker, OB Shchekin, and C. Cao. Dynamic response of 1.3-μm-wavelength InGaAs/GaAs quantum dots. *Appl. Phys. Lett*, 76:1222–1224, 2000.

[172] V. Zhuk, D.V. Regelman, D. Gershoni, M. Bayer, J.P. Reithmaier, A. Forchel, P.A. Knipp, and T.L. Reinecke. Near-field mapping of the electromagnetic field in confined photon geometries. *Phys. Rev. B*, 66(11):115302, Sep 2002.

[173] A. Zrenner, E. Beham, S. Stufler, F. Findeis, M. Bichler, and G. Abstreiter. Coherent properties of a two-level system based on a quantum-dot photodiode. *Nature*, 418(6898):612–614, 2002.

[174] A. Zrenner, LV Butov, M. Hagn, G. Abstreiter, G. Böhm, and G. Weimann. Quantum dots formed by interface fluctuations in AlAs/GaAs coupled quantum well structures. *Physical Review Letters*, 72(21):3382–3385, 1994.

[175] V. Zwiller, T. Aichele, and O. Benson. Single-photon Fourier spectroscopy of excitons and biexcitons in single quantum dots. *Physical Review B (Condensed Matter and Materials Physics)*, 69(16):165307, 2004.

Vita

Andreas Muller was born in Munich, Germany, on October 11, 1978, the son of Fritz Müller and Doris Müller. He graduated from high school Lycée Gustave Jaume, Pierrelatte, France in 1997 and received a Vordiplom (Associate degree) in physics from the Technische Universität München, Munich, Germany in 1999. He transferred to the University of Texas at Austin in the same year, where he received a bachelor's (B.S.) degree in physics in 2001. He entered the graduate school at the University of Texas at Austin in the Spring of 2002 where he joined Prof. C. K. Shih's nanoscale electronic materials research group and studied the optical properties of semiconductor quantum dots. He received a Master's (M.A.) degree in physics in Dec. 2003.

Permanent address: Le Travers du Haut Plan
F-07700 St. Martin d'Ardeche
France

This dissertation was typeset with LaTeX[†] by Andreas Muller.

[†] LaTeX is a document preparation system developed by Leslie Lamport as a special version of Donald Knuth's TeX Program.